Computational Design of High Temperature Alloys

Yu, Hao

Important note
To cite this publication, please use the final published version (if applicable).
Please check the document version above.

The Computational Design of High Temperature Alloys

This dissertation has been approved by the

Promotors: Prof. dr. ir. S. van der Zwaag and Prof. dr. W. Xu

Composition of the doctoral committee:

Rector Magnificus	Chairperson
Prof. dr. ir. S. van der Zwaag	Delft University of Technology, promotor
Prof. dr. W. Xu	Northeastern University, China, Delft University of Technology, promotor

Independent members:

Prof. dr. ir. R.H. Petrov	Ghent University, Belgium
Prof. dr. A. Borgenstam	KTH Royal Institute of Technology, Sweden
Prof. dr. U. Krupp	RWTH Aachen University, Germany
Dr. ir. N.H. van Dijk	TNW, Delft University of Technology
Dr. ir. W.G. Sloof	3ME, Delft University of Technology
Prof. dr. E.H. Brück	TNW, Delft University of Technology, Reserved

Contents

Introduction

1.1 The computational design approach for alloy development

Notwithstanding their long history, the work on new alloys with new chemical compositions and new processing conditions must continue to meet the ever-rising performance demand from industries. The traditional experimental alloy development cycle is generally based on the adaption of already existing compositions[1-5]. Although new alloy compositions with potentially improved material properties are expected to be similar to already known alloys, this procedure impedes efficiently finding novel compositions in the large multi-dimensional design-space containing all potential alloying elements[6, 7]. In addition, the complex cross effects due the interactions of alloying elements have delayed finding the "optimal solution" for targeted applications.

In recent decades, the application of computational techniques to assist the alloy design process has pronouncedly accelerated the pace of new alloy developments [8-12]. New opportunities can be spotted more cost-effectively with higher efficiency by the help of computational approaches, such as ab initio calculations[13], artificial neural networks [14] and so on. Among the various computational methods, the CALPHAD (CALculation of PHAse Diagrams) method is well-known as a powerful approach to predict the equilibrium microstructural features based on the chemical composition of the target material and the service conditions (temperature, pressure and so on)[15-17]. By employing reliable thermodynamic databases and computer interfaces, the competition and synergy among various alloying elements in a complex multi-element system can be analysed as a function of the temperature and elemental composition. The CALPHAD results, interpreted by human operators/metallurgists, can be utilized to guide and accelerate the exploration of new alloy systems.

Recently, the CALPHAD method has been successfully combined with Genetic Algorithms for novel steels development at the TUDelft. The

"alloy-by-design" model was built by employing quantitative microstructural parameters to bridge the chemical compositions and target properties through thermodynamic and kinetic calculations. By applying the computational model, novel advanced ultra-high strength stainless steels for room temperature application[18, 19] and novel heat resistant steels applied under temperature around 650°C[20-22] have been successfully developed. As shown in figure 1.1, the newly designed alloys are expected to outperform their commercial counterparts in separated domains with different strengthening mechanisms[23].
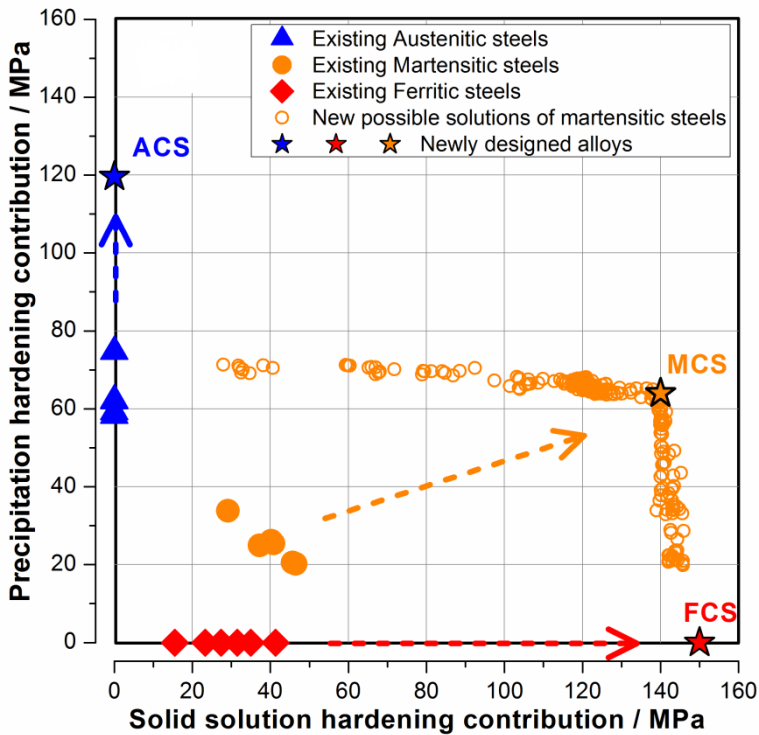
Figure 1.1 Comparison of designed and existing creep resistant alloys[23].

1.2 High temperature alloys: introduction

1.2.1 Heat resistant ferritic/martensitic steels

Heat resistant steels are the most commonly used materials in automotive, aerospace, fossil and nuclear power plants applications, due to the combination of good mechanical properties and corrosion resistance[24]. The ferritic/martensitic heat resistant steels, having a ferrite-type matrix, are generally applied as thick-section components in thermal power plants, as they possess higher thermal conductivities and lower thermal expansion coefficients compared to their austenitic counterparts[25, 26]. With the purpose of improving the generating efficiency and reducing the emission of CO_2, higher operating temperatures and pressures force the need for new steels with better performance[27]. This has led to consistent research activities placing emphasis on new steel development through the optimization of chemical compositions and heat treatment process.

Heat resistant ferritic/martensitic steels generally contain up to 13 different alloying elements, while the improvement of their outstanding performance have been mainly achieved through minor changes in the alloy composition. Heat resistant ferritic/martensitic steels can be roughly divided into two groups, 9-12%Cr steels and high Cr (>12 wt.%) steels. Although differences in chemical compositions among different grades of 9-12%Cr steels can be found, they all share quite similar microstructures. Namely, the typical microstructure is a tempered martensite with finely-dispersed small-sized particles pinning the mobility of dislocations and sub-grain boundaries[27, 28]. Their improved creep strength is due to the retarded migration of dislocations and sub-grain boundaries, wherein the most essential strengtheners to stabilize the microstructure are MX (M=Nb, V, ect.; X=C, N, ect.;) carbonitrides. MX precipitations are characterized as the backbone of long-term strength for heat resistant steels systems due to their small

initial sizes and excellent coarsening resistance. Novel heat resistant steels with higher Cr content may have better oxidation and corrosion resistance but suffer from a reduced microstructural stability[29]. Experimental results show that with Cr alloying level rising above 10 wt.%, MX precipitates are unavoidably consumed in the course of time and transformed into detrimental Z phase after about 10^4 hours under creep conditions[30]. Z phases nucleate in the vicinity of MX particles and grow at the expense of MX forming elements, which will easily extend to micron size dimensions and thereby fail to provide any strengthening effects. This detrimental transformation has been proved the reason for "premature failure" of heat resistant steels during long-term creep test[31, 32]. High Cr levels trigger the undesirable microstructure instability, on the other hand, a sufficiently high Cr concentration is mandatory for high corrosion and oxidation resistance at elevated temperature application. The conflict between the requirements of microstructural stability and corrosion resistance remains unsolved until now and currently became a serious problem for all steel developers.

In 2000s, the requirement to develop creep resistant steels functioning at higher temperatures ($> 620^0$C) promoted a new concept for high chromium steel. These novel steels with a chromium content higher than 14 wt.% have been developed by fully annealing process without undergoing a martensitic transformation. Therefore, they possess the matrix with a relatively low dislocation density, while the formation of detrimental δ-phase with high Cr alloying can be also circumvented. Owing to the long-term microstructure stability, the high Cr steels manage to outperform the traditional 9-12%Cr steels during long time creep service[33-35]. Also, the extremely low solubility of carbon and nitrogen in ferrite makes the use of stable MX precipitates impossible. Hence, attempts have been made to tailor the properties of traditionally-considered undesirable phases by adjusting the element concentrations[36, 37]. Laves phase and $M_{23}C_6$ carbides shows some potential in acting as strengthening precipitates, since their coarsening

behaviour and particle morphology can be well adjusted by novel element alloying[33, 38]. High Cr steels strengthened by Laves phase precipitates have been successfully developed in Japan, while the newly designed alloys have been experimentally validated with better long-term creep properties compared with commercial grades P92. Inspired by the same concept, attempts have been made to develop novel W or Mo containing martensitic creep resistant steels strengthened by Laves phase and $M_{23}C_6$ precipitates[36, 37]. The coarsening rate of these strengthening phases have been tuned to a minimum value with their volume fraction tuned to a maximum level simultaneously. The strengthening effect of such Laves phase precipitates can be comparable to that of MX carbonitrides.

The conventional approach in designing creep resistant steels, as mentioned above, is basically the combination of precipitation hardening (MX carbonitrides, $M_{23}C_6$ carbides, Laves phase and so on) and solid solution strengthening (commonly employing W and Mo) mechanisms, while the principle is to postpone the formation of creep defects as longer as possible. However, during creep service, once the initial creep damage is formed, the creep properties degrade in a continuous manner without any tendency to stop or slow down. Recently an alternative concept, the so-called "self-healing", has been applied in designing novel materials, namely the damage can be healed by the material itself[39, 40]. This self-healing concept of designing novel materials has been successfully applied in wide range of materials such as polymers[41], coatings[42], concrete[43] and metals[44], while the main strategy is to enable the "local temporary mobility" of the healing agents. More precisely, the mobile healing agents are designed to arrive at the damage site only when the damage appears. In the specific case of heat resistant steels, the selection of alloying elements which can provide potential self-healing agents should fulfil the following key requirements summarized by Zhang[45]: i) a supersaturated system to provide driving force for healing precipitation; ii) a larger atomic radius for solute atoms than that of Fe to achieve a net volumetric filling

process; iii) the preference of precipitation should be at damage site rather than in the matrix; iv) the diffusion of healing atoms should be faster than the self-diffusion of Fe to make healing faster than pore formation; and v) the solute atom should not interact with other atoms to become immobile before precipitation at the damage sites. In case all abovementioned requirements are fulfilled, the occurrence of local mechanical damage can cause atoms to move towards the defect site and fill it, such that it is no longer present or cannot grow further under prevailing conditions. With these abovementioned selection requirements, four iron-based binary systems with potential self-healing properties have been selected and investigated, i.e., Fe-Cu, Fe-W, Fe-Mo and Fe-Au system[46, 47]. Systematic researches have been made to investigate their autonomous healing process qualitatively and quantitatively, but there are no studies yet which take the concept tested on pure binary alloys to the realm of real high temperature steels.

1.2.1 Ni-single crystal superalloys

For more elevated temperature applications, the nickel-base superalloys have emerged as the materials of choice with outstanding creep resistance, particularly when the operating temperatures are above $800^{o}C$ as is the case for gas turbines used for jet propulsion in aerospace engineering[48]. Ni-based superalloys have gone through a continuous development phase since the design of the first Ni-based superalloy in the 1940s, then a concerted period of alloy and process development enabled their performance to be improved significantly[49-51]. By eliminating grain boundaries as the weaker parts of the alloy for high temperature strength applications, single crystalline superalloys now achieve the highest high temperature mechanical strength and creep resistance possible[48].

The superior high temperature properties of Ni-based single crystal (SX) superalloys are largely dictated by their unique microstructural features. The typical microstructure of Ni superalloy single crystals consists of a high volume fraction(up to 70% at room temperature) γ' phase with the continuous FCC γ phase. The ordered $L1_2$ structure γ' phase exists in the form of cuboids with coherent interfaces to the matrix, which itself is present in the form of narrow channels between the γ' cuboids. During creep service, plenty of deformation mechanisms can be found in Ni-SX superalloys system, include anti-phase boundaries (APB), complex stacking faults (CSF), superlattice intrinsic stacking faults (SISF) and superlattice extrinsic stacking faults (SESFs). The main deformation mechanisms strongly depend on the applied stress and temperature domains, where the mobile dislocations interacts differently with precipitations and matrix, as shown in figure 1.2.
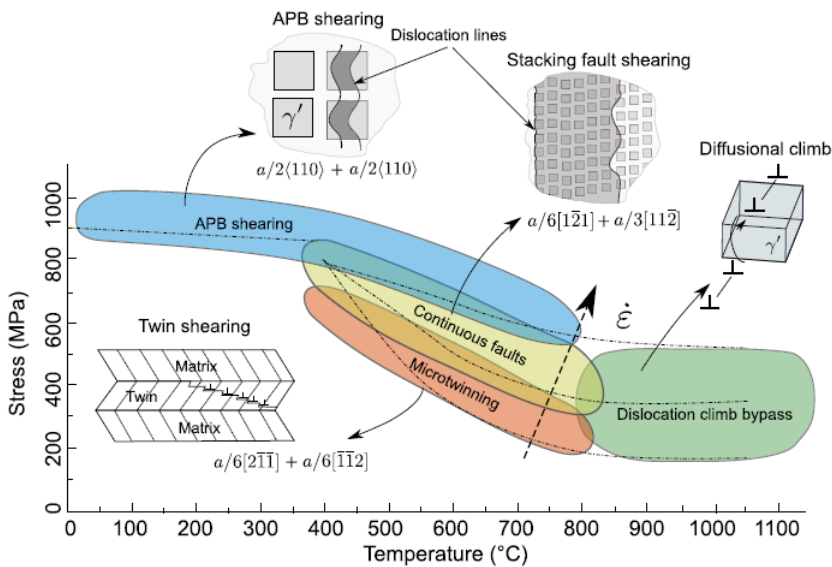
Figure 1.2 Deformation mechanisms for a single crystal superalloy at the different stress, temperature and strain rate domains[52, 53]

8

Since single crystals are more designed for withstanding higher temperatures, here we focus more on the high temperature ($> 950^{\circ}$C) and low stress (< 200MPa) domain, where interactions between dislocation and γ phases, namely the climbing and bypassing of dislocations, are the dominate deformation mechanism. In that case the creep performance is intrinsically determined by the combined effects of microstructural evolution and the dislocation behaviour. In the field of microstructural evolution, the cuboid γ precipitates will experience a morphology change during service, which is so-called rafting process. The initial microstructure in Ni superalloys gradually degrades by a directional coarsening process of γ′ precipitates. That is, the initially adjacent cuboidal γ′ particles coalesce and form platelets which turn into plate-like or rid-like structures[54, 55]. The rafting process will generally be completed during the first creep stage, while the fully rafted lamellar microstructure can remain stable during the whole creep stable stage, until the γ' gradually interconnects and becomes the matrix phase surrounding isolated γ phase islands[56, 57]. This process is known as the 'topological phase inversion'. This inverted microstructure can be maintained during the accelerated creep stage but rapidly loses it regularity and this leads to rupture. On the other hand, the creep response strongly depends on the changes in the dynamics and topology of the dislocations[58]. At the beginning of creep loading, the deformation is governed by the dislocation glide and dislocation multiplication in the γ channels. Soon thereafter the mobile dislocations start to accumulate and become rearranged at the γ/γ' interface, while the formation of lamellar rafts takes place, leading to the widely observed formation of dislocation networks on the γ/γ' interface[58-62]. Analogous to the lamellar microstructure, the dislocation network will remain stable until the end of the stable creep stage, when the network begins to degrade by huge amounts of dislocations cutting into the rafted γ′ through the interface. This dislocation multiplication process finally leads to rupture. In the literature the microstructure evolution and that of

the dislocation structure are reasonable well documented but most surprisingly they have not yet been connected to each other.

1.3 Contents of this thesis

In this thesis, the newly developed alloy design approach has been applied to a compositional optimization of heat resistant steels. In Chapter 2, The balancing effects of alloying elements have been thermodynamically and kinetically simulated in order to reach the "optimal trade-off" between cost and performance. Calculations have indicated that decreasing Co levels will reduce costs but inevitably lead to lower strength values. In the case of Laves phase strengthened steels, Co can be partially replaced by W to yield the same precipitation strengthening level, while in steels strengthened by $M_{23}C_6$ the long-term strength level was found to monotonously depend on the Co level. To handle the problem of microstructural instability for modern heat resistant steels with high-Chromium alloying, in Chapter 3, attempts have been made to predict the formation of undesirable Z phase thermodynamically and kinetically. Simulations have shown that a high Cr level will unavoidably result in the formation of Z-phase. Compositional adjustments which lead to a combination of a high Cr level (12-15 %Cr) and a reduced tendency to form Z-phase precipitates do not seem possible. In Chapter 4, novel creep resistant steels with self-healing properties have been computationally developed following the same generic alloy design approach. The precipitation behaviour of self-healing agents, in this case, W-containing Laves phase, have been constitutively expressed by a thermodynamic parameter, where the self-healing properties can be quantified in alloy-by-design routine. The computed optimal compositions form the start of an extensive experimental program to be started after the completion of this PhD project. In Chapter 5, a model for the minimum creep rate based on thermodynamic and kinetic calculations and using an existing detailed

dislocation dynamics model has been built, which takes the dislocation migration behaviours as well as the rafted microstructure into consideration. By applying this model, the creep properties of existing Ni superalloy grades can be well reproduced. Finally, in Chapter 6, a new thermodynamic model is presented to connect the chemical compositions and the rate of microstructure evolution, more precisely, to predict the γ channel widening of Ni commercial grades, in particular the CMSX family of superalloys. The effect of alloying elements on the microstructural parameters, γ' coarsening rates and microstructure stability have been analysed by this model, and the outcome can guide further work on compositional optimization.

References

[1]   Taneike M, Abe F, Sawada K. Nature 2003;424:294.
[2]   Yoon KE, Noebe RD, Seidman DN. Acta Mater 2007;55:1159.
[3]   Amouyal Y, Mao Z, Seidman DN. Acta Mater 2010;58:5898.
[4]   Beswick JM. Metallurgical Transactions A 1987;18:1897.
[5]   Abe F, Nakazawa S. Metall Mater Trans A 1992;23:3025.
[6]   Markl M, Müller A, Ritter N, Hofmeister M, Naujoks D, Schaar H, Abrahams K, Frenzel J, Subramanyam APA, Ludwig A, Pfetzing-Micklich J, Hammerschmidt T, Drautz R, Steinbach I, Rettig R, Singer RF, Körner C. Metall Mater Trans A 2018.
[7]   Sandström R. Mater Design 1985;6:328.
[8]   Kuehmann C, Olson G. Mater Sci Technol-lond 2009;25:472.
[9]   Curtarolo S, Hart GL, Nardelli MB, Mingo N, Sanvito S, Levy O. Nature Mater 2013;12:191.
[10]   Asta M. JOM 2014;66:364.
[11]   Datta S, Davim JP. Computational Approaches to Materials Design: Theoretical and Practical Aspects: Theoretical and Practical Aspects: IGI Global, 2016.
[12]   Olson GB. Science 1997;277:1237.

[13]   Fahrenthold E. TechConnect Briefs 2016;4:59.
[14]   Kiselyova N, Gladun V, Vashchenko N. J Alloy Compd 1998;279:8.
[15]   Kaufman L. Calphad 2001;25:141.
[16]   Luo AA. Calphad 2015;50:6.
[17]   Schaffernak BC, Cerjak HH. Calphad 2001;25:241.
[18]   Xu W, Rivera-Díaz-del-Castillo P, Wang W, Yang K, Bliznuk V, Kestens L, Van der Zwaag S. Acta Mater 2010;58:3582.
[19]   Xu W, Zwaag Svd. Isij Int 2011;51:1005.
[20]   Lu Q, Xu W, van der Zwaag S. Philos Mag 2013;93:3391.
[21]   Lu Q, Xu W, van der Zwaag S. Comp Mater Sci 2014;84:198.
[22]   Lu Q, Xu W, van der Zwaag S. Acta Mater 2014;77:310.
[23]   Lu Q. Computational design of heat resistant steels with evolving and time-independent strengthening factors. Doctoral dissertation. Netherlands: Delft university of Technology, 2015.
[24]   Ennis P, Czyrska-Filemonowicz A. Sadhana 2003;28:709.
[25]   Masuyama F. Isij Int 2001;41:612.
[26]   Klueh R, Nelson AT. J Nucl Mater 2007;371:37.
[27]   Cerjak H, Hofer P, Schaffernak B. Isij Int 1999;39:874.
[28]   Yan W, Wang W, Shan Y, Yang K. Front Mater Sci 2013;7:1.
[29]   Danielsen HK, Hald J. Energy Mater 2006;1:49.
[30]   Sawada K, Kushima H, Kimura K. Isij Int 2006;46:769.
[31]   Kocer C, Abe T, Soon A. Mater Sci Eng A 2009;505:1.
[32]   Danielsen HK. Mater Sci Technol-lond 2016;32:126.
[33]   Kimura K, Seki K, Toda Y, Abe F. Isij Int 2001;41:S121.
[34]   Toda Y, Seki K, Kimura K, Abe F. Isij Int 2003;43:112.
[35]   Shibuya M, Toda Y, Sawada K, Kushima H, Kimura K. Mater Sci Eng A 2016;652:1.
[36]   Lu Q, Xu W, van der Zwaag S. Metall Mater Trans A 2014;45:6067.
[37]   Lu Q, Toda Y, Harada N, Xu W, van der Zwaag S. Comp Mater Sci 2015;107:110.
[38]   Abe F. Mater Sci Eng A 2001;319:770.
[39]   van der Zwaag S. Self healing materials: an alternative approach to 20 centuries of materials science: Springer Science+ Business Media BV Dordrecht, The Netherlands, 2008.
[40]   Ghosh SK. Self-healing materials: fundamentals, design strategies, and applications: John Wiley & Sons, 2009.
[41]   Zhong N, Post W. Compos Part A Appl Sci Manuf 2015;69:226.

[42]   Cho SH, White SR, Braun PV. Adv Mater 2009;21:645.

[43]   De Belie N, Gruyaert E, Al-Tabbaa A, Antonaci P, Baera C, Bajare D, Darquennes A, Davies R, Ferrara L, Jefferson T. Adv Mater Interfaces 2018:1800074.

[44]   van Dijk N, van der Zwaag S. Adv Mater Interfaces 2018:1800226.

[45]   Zhang S, Kohlbrecher J, Tichelaar FD, Langelaan G, Brück E, van der Zwaag S, van Dijk NH. Acta Mater 2013;61:7009.

[46]   Fang H, Versteylen CD, Zhang S, Yang Y, Cloetens P, Ngan-Tillard D, Brück E, van der Zwaag S, van Dijk NH. Acta Mater 2016;121:352.

[47]   Zhang S, Fang H, Gramsma ME, Kwakernaak C, Sloof WG, Tichelaar FD, Kuzmina M, Herbig M, Raabe D, Brück E, van der Zwaag S, van Dijk NH. Metall Mater Trans A 2016;47:4831.

[48]   Reed RC. The superalloys: fundamentals and applications: Cambridge university press, 2008.

[49]   McLean M. Nickel-based alloys: Recent developments for the aero-gas turbine. High Performance Materials in Aerospace. Springer, 1995. p.135.

[50]   Pollock TM, Tin S. J Propul Power 2006;22:361.

[51]   Long H, Mao S, Liu Y, Zhang Z, Han X. J Alloy Compd 2018;743:203.

[52]   Smith TM, Unocic RR, Deutchman H, Mills MJ. Mater High Temp 2016;33:372.

[53]   Barba D, Alabort E, Pedrazzini S, Collins DM, Wilkinson AJ, Bagot PAJ, Moody MP, Atkinson C, Jérusalem A, Reed RC. Acta Mater 2017;135:314.

[54]   Nabarro FR. Metall Mater Trans A 1996;27:513.

[55]   Ignat M, Buffiere J-Y, Chaix J. Acta Metall Mater 1993;41:855.

[56]   Epishin A, Link T, Brückner U, Portella P. Acta Mater 2001;49:4017.

[57]   Goerler JV, Lopez-Galilea I, Mujica Roncery L, Shchyglo O, Theisen W, Steinbach I. Acta Mater 2017;124:151.

[58]   Zhang J, Murakumo T, Koizumi Y, Kobayashi T, Harada H, Masaki Jr S. Metall Mater Trans A 2002;33:3741.

[59]   Lasalmonie A, Strudel J. Philos Mag 1975;32:937.

[60]   Gabb T, Draper S, Hull D, MacKay R, Nathal M. Mater Sci Eng A 1989;118:59.

[61]   Sugui T, Huihua Z, Jinghua Z, Hongcai Y, Yongbo X, Zhuangqi
       H. Mater Sci Eng A 2000;279:160.
[62]   Zhang J, Harada H, Koizumi Y, Kobayashi T. J Mater Sci
       2010;45:523.

On the Cobalt – Tungsten/Chromium balance in martensitic creep resistant steels

Recently novel martensitic creep resistant steels strengthened by slowly coarsening Laves phase or stable $M_{23}C_6$ precipitates have been identified both computationally and experimentally. The coarsening kinetics of these precipitates, traditionally considered to be very detrimental in creep steels, can be suppressed to a degree which makes them attractive strengthening factors by alloying such steels to high Cobalt levels. As high Co levels are undesirable for various reasons, in the present work, the characteristics of Laves phase and $M_{23}C_6$, in particular the volume fraction, coarsening rate and precipitation strengthening factor, in newly designed alloys are computationally compared with those of existing Co-containing creep steels. The binary analyses of Co-M balance show that Co-W are highly coupled for creep steels strengthened by Laves phase deposits and W can partially replace Co to yield the same precipitation strengthening. For the $M_{23}C_6$ strengthened alloys, irrespective of the Cr level, a high Co concentration is necessary for a high creep resistance.

2.1 Introduction

The efficiency of coal-fired ultra-supercritical power plants depends to a high degree on the operation temperature, and hence relies on the development of high-end creep resistant steels stable at temperatures above those currently used in industrial installations [1-5]. To achieve and maintain a high performance during long-term service at elevated temperatures, an undesired development of the microstructure should be suppressed, which requires a stable precipitation strengthen strategy as well as a stable matrix. Generally, precipitation of a secondary phase with a relatively high-volume fraction, a small particle size and an excellent thermal stability is considered to be the preferred strategy [6-9]. For a given use temperature the precipitate volume fraction, the initial precipitate size and its coarsening rate are all influenced by alloying additions.

It has been reported by several researchers that alloying of creep steels by cobalt additions can effectively improve the high temperature creep resistance through various mechanisms. Gustafson[10] computationally studied the effect of Co on the coarsening rate of $M_{23}C_6$ in P92 steel and found that 10 wt.% of Co addition can decrease the coarsening rate of carbides by 30%, as well as retard the decomposition of the lath martensitic matrix. Yamada [11] and Shibuya [12] and their co-workers investigated the Co effect experimentally and concluded that Co alloying suppresses the formation of δ-ferrite and significantly promotes a homogeneous precipitation of MX and $M_{23}C_6$ carbides as well as Fe_2W intermetallics. Helis and Kipelova's work[13, 14] used combined computational and experimental approaches and confirmed the desirable effects of Cobalt since it increases the total amount of precipitates formed as well as decreases the coarsening rate of carbides.

Recently a genetic based computational alloy design approach coupling thermodynamics and kinetics principles has been developed and applied to the design of novel Cobalt-rich creep resistant steels intended to

operate at least 10^5 hours at 650°C[15]. The computational approach identified Co-containing martensitic creep resistant steels relying on precipitation strengthening by $M_{23}C_6$ and Laves phase [16], which are traditionally considered as detrimental phases because of their high coarsening rates. However, the calculations suggested that the coarsening process can be significantly retarded by Co additions to the same low level of that predicted for those the desirable MX carbides by bringing the Co level to 10 wt.% Given the undesirable features of Cobalt, e.g. a high cost and a high toxicity, the present work focuses on exploring the possibility to reduce the Co level while maintaining the high performance of the new alloy systems. The effects of Co on the temporal evolution of $M_{23}C_6$ and Laves phases in a multi-component martensitic matrix at a fixed temperature of $650 ^0$C are investigated computationally. The binary analyses of Co-W and Co-Cr isopleth systems for predicted optimal matrix compositions are performed to identify the opportunities to substitute Co by either W or Cr.

2.2 Model description

The computational design methodology used here and validated in a number of earlier studies involves two key steps: the translator and creator, which link the properties, microstructure and eventually the composition and processing [15, 17]. For the design of martensitic creep resistant steels strengthened by Laves phase or $M_{23}C_6$, the translator defines the target microstructure as: 1) a fully martensitic matrix with adequate corrosion and oxidation resistance by setting a minimal Cr level in the matrix after formation of all precipitates; 2) a high volume fraction of Laves phase or $M_{23}C_6$ precipitates with a minimal coarsening rate throughout its service time and 3) a limited volume fractions of undesirable other secondary phases.

Given the target microstructure as defined above, the creator uses multiple quantitative criteria to ensure the formation of the desired target microstructure: (1) the equilibrium volume fraction of austenite at austenisation temperature (T_{aus}) should be higher than 99%; (2) the martensitic start temperature (Ms) should be higher than 250°C. (3) the Cr concentration in the matrix upon completion of the precipitation reactions should at least be 10 wt.%. (4) the volume fraction of martensitic matrix and target precipitates at the service temperature should be higher than 99%. For those candidate solutions which fulfil all go/no-go criteria, the time dependent precipitation hardening effect (PH, σ_p) of Laves phase or $M_{23}C_6$ are optimized for the given service condition, i.e. 10^5 hours at 650°C. The model used is a multistep genetic algorithm (GA) sampling the equilibrium phase fractions and compositions at the homogenisation temperature, the quenching temperature and the long term use temperature of over a 100.00 potential steel compositions using Thermo-calc software (using database TCFE7) and the metallurgical criteria specified above. The GA model returns the steel composition fulfilling all criteria and yielding the highest precipitation strengthening factor at the intended combination of use temperature and use time. The strengthening factor (PH, σ_p) depends on both the final precipitate fraction (f_p) as well as the predicted size of the coarsened precipitates (K) in the following manner:

$$\sigma_p \propto 1/L = \sqrt{f_p}/r = \sqrt{f_p}/\sqrt[3]{r_0^3 + Kt}$$

where L is the average inter-particle spacing, f_p is the equilibrium volume fraction of the strengthening precipitates at the service temperature, r_0 is the critical precipitate nucleus size, K is the factor of coarsening rate and t is the exposure time at the high temperature. The equation shows that the highest strengthening factors are obtained for high volume fractions and small precipitate sizes, i.e. very low coarsening rates. The computational details of the model and its application to MX precipitation strengthened creep resistant steel design can be found elsewhere [11]. In the present model it is assumed that the

contribution of other strengthening factors such as solid solution strengthening, grain size and dislocation density are affected to a much lower extent by the compositional changes.

2.3 Results

The GA model proposed optimal compositions for martensitic creep resistant steels strengthened by Laves phase or $M_{23}C_6$ precipitates after being exposed to 10^5 hours at 650 ^{0}C are named LavesW and $M_{23}C_6$W respectively. Their compositions and desired prior austenisation temperature T_{aus} are given in table 2.1. Table 2.2 contains the compositions of state-of-the art commercial creep steel containing Laves phase and $M_{23}C_6$ carbides as strengthening precipitates.

The tables show that the proposed new LavesW alloy has a very high Co level (the maximum allowed level), a relatively high concentration of W (again the maximum allowed design level) and a low C level compared to existing steels. The results are in line with the design concept that Laves phase is the target strengthening precipitates, wherein W is the main forming element of Fe_2W Laves phase. For the same reason, the proposed $M_{23}C_6$W alloy strengthened by $M_{23}C_6$ carbides contains relatively higher concentrations of Cr and C. The Co addition in newly designed alloys are noticeably higher than that existing steels, and its origin will be analysed in the discussion. Recent experimental results by Fedoseeva[18] show that 9-12%Cr heat-resistant steels with a relatively low W content(2 wt.%) tends to form W-rich $M_{23}C_6$ carbides coupled with the decomposition of retained austenite, while a higher W concentration leads to the formation of metastable W-rich M_6C carbides, followed by further transformation into stable Laves phase. It is interesting to point out that the concentrations of W in the two newly designed alloys, i.e. 1.61 wt.% in $M_{23}C_6$W and 10% in LavesW, are perfectly in line with the experimental observations.

Table 2.1 Composition (in wt.%) of newly designed alloys strengthened by Laves phase and $M_{23}C_6$.

	C	Cr	Ni	W	Co	Nb	N	V	Mo	Ti	Al	Taus/^{o}C
LavesW	0.001	10.84	3.23	10.00	10.00	0.32	0.03	0.001	0.00	0.11	0.001	1239
$M_{23}C_6W$	0.15	16.00	0.01	1.61	10.00	0.001	0.006	1.00	0.00	0.01	0.001	1069

Table 2.2 Composition (in wt.%) of existing Co-containing creep resistant steels.

	Tune	C	Cr	Ni	W	Co	Nb	N	V	Mo	Si	Mn	B	Others
P92[10, 19, 20]	0Co	0.1	9.0	0.1	1.8	0.0	0.06	0.05	0.2	0.6	0.3	0.5	0.005	0.008P, 0.006S
	3Co	0.1	9.0	0.1	1.8	3.0	0.06	0.05	0.2	0.6	0.3	0.5	0.005	
	5Co	0.1	9.0	0.1	1.8	5.0	0.06	0.05	0.2	0.6	0.3	0.5	0.005	
P911[14]	0Co	0.13	8.6	0.05	3.0	0.0	0.07	0.04	0.2	0.9	0.06	0.02	0.005	
	3Co	0.13	8.6	0.05	3.0	3.0	0.07	0.04	0.2	0.9	0.06	0.02	0.005	
9Cr-3W[21]		0.078	9.0	-	3.0	3.0	0.05	0.002	0.2	-	0.3	0.5	-	
NF12[22]		0.08	11.0	-	2.6	2.5	0.07	0.05	0.2	0.2	0.2	0.5	0.004	0.07Ta
SAVE12[22]		0.10	11.0	-	3.0	3.0	0.07	0.04	0.2	-	0.3	0.2	-	0.04Nd

Table 2.3 Fulfilments of go/no-go criteria, i.e., the equilibrium volume fraction of austenite at austenisation temperature V_{Aus}(in vol.%), martensitic start temperature T_{Ms}(in ^{o}C), Cr concentration in the matrix at service temperature Val_{Cr}(in mass.%) and volume fraction of martensitic matrix and target precipitates at service temperature (i.e., 650°C) $V_{desirable}$(in vol.%), of existing steel grades. The values marked in red represent values violating the imposed criteria in the model.

Base	Tune	V_{Aus}/%>99	T_{Ms}/^{o}C>250	Val_{Cr}/mass.%>10	$V_{desirable}$/%>99
P92	0Co	99.7	368	8.1	100
	3Co	99.7	389	8.0	100
	5Co	99.7	403	7.9	100
P911	0Co	99.8	370	7.7	100
	3Co	99.8	391	7.6	100
9Cr-3W		99.9	401	8.3	100
NF12		99.9	369	10.3	100
SAVE12		99.9	373	10.1	100
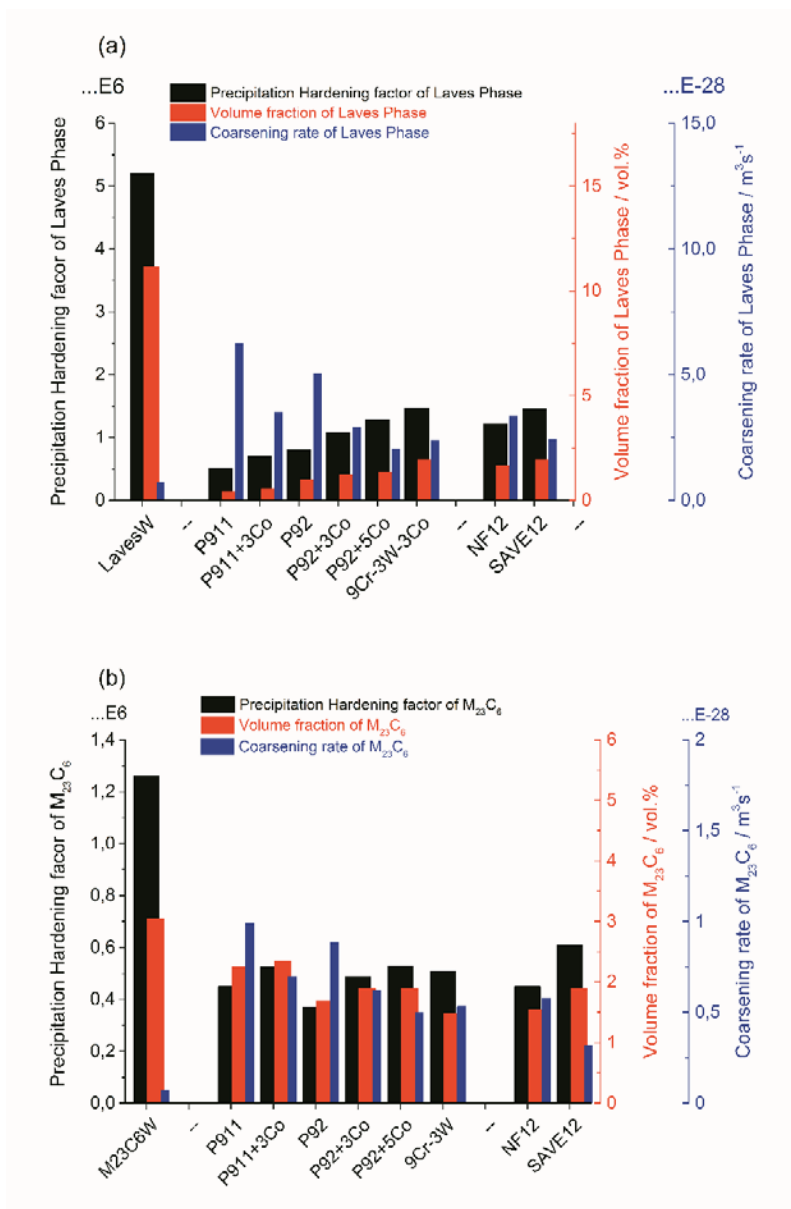
Figure 2.1 the key precipitation characteristics, i.e., precipitation hardening factor, volume fraction and coarsening rate for the newly designed (a) LavesW and (b) $M_{23}C_6$W alloys and those of the existing Co-containing creep resistant steel grades.

In our former publications, the validity of the formulated go/no-go criteria in MX carbides strengthened austenitic[23] and martensitic [24] creep resistant steels has been demonstrated by applying them on existing alloys. As in the previous model validation tests, the results show that in fact all existing steels meet criteria concerning the austenite volume fraction at T_{aus}, the martensitic start temperature T_{Ms} and volume fraction of matrix and desirable precipitates at the service temperature of 650^oC. However, the Cr concentrations in the matrix for most of the existing alloys cannot reach 10 wt.%, except NF12 and SAVE12 steels. The mismatch implies that employed corrosion resistant criterion is too sharp compared with existing steels, and hence a better corrosion and oxidation resistance can be expected from the newly designed alloys.

The key precipitation strengthening factors, volume fractions and coarsening rates of the newly designed Co-rich alloys and their existing commercial counterparts are calculated and plotted in figure 2.1 in the order of their Cr concentrations. For P911 and P92 serial steels, it can be observed that, with the addition of Co (P911, P911+3Co and P92, P92+3Co, P92+5Co), the coarsening rates of Laves phase decrease significantly, the volume fractions increase slightly and, as a result, the precipitate strengthening factors increase monotonously. figure 2.1b also indicates that Co can effectively increase the volume fraction and retard the coarsening rate of $M_{23}C_6$ carbides in P911 and P92 steels. It is also worth noting that the calculated Co effects on volume fraction of $M_{23}C_6$ precipitates in these steels correlate well with the experimental results by Gustafson[10] and Kipelova[25].

Compared to existing alloys in figure 2.1a, the newly designed steel LavesW alloy has an remarkably high volume fraction and a relatively low coarsening rate, leading to the highest precipitation strengthening factor. Similarly, $M_{23}C_6W$ in figure 2.1b has the lowest coarsening rate and the highest volume fraction of $M_{23}C_6$ phase, and hence guarantees that $M_{23}C_6W$ outperforms all the existing alloys. In summary, the newly designed alloys with a high Co concentration surpass all existing

counterparts' performance in various aspects, but the exact effect of Co and its possible substitutions are still yet to be further explored in details.

To further clarify the Co effects on the precipitation hardening factor and design constraints (go/no-go criteria), the compositions of LavesW and $M_{23}C_6W$ alloy are taken as baseline and effects of Co variations are evaluated. The results are shown in figure 2.2 In these figures the original Co upper concentration used in the alloy design study (10 wt.%) is expanded twice to make it possible to separate real metallurgical factors from model-imposed constraints. The horizontal, backward and forward slash patterns indicate concentration ranges violating the go/no-go criteria of Cr concentration in the matrix, austenite volume fraction and volume fraction of desirable phases at service temperature respectively.
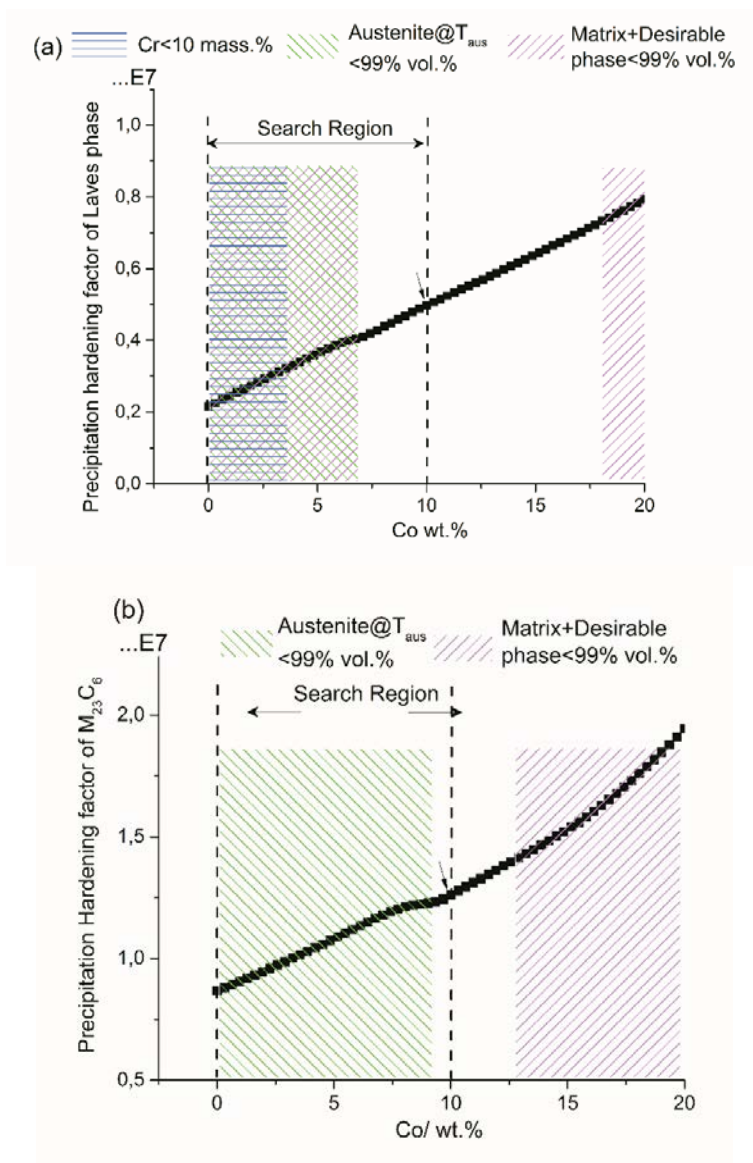
Figure 2.2 The effect of Co on the precipitation hardening factor, with the domains in which the various go/no-go criteria are activated are indicated. The composition of (a) LavesW and (b) $M_{23}C_6W$ alloys were taken as baseline. The vertical dashed lines define the search region of Co, and the arrows indicate the optimal Co concentration in optimization.

The unmarked area in figure 2.2a indicates that the precipitation hardening factor of Laves phase increases linearly with Co concentration. For the high Co range (above 17.9%), the criterion that the volume fraction of austenite at austenitisation temperature should be above 99% is violated, because of the formation of the detrimental σ phase. For Co concentrations below 7.1 wt.%, the two criteria, volume fraction of austenite at austenite temperature and volume fraction of matrix plus target phase at service temperature, are violated simultaneously. The first violation is due to the formation of δ-ferrite at low Co levels, which is in a good agreement with Helis' experimental observation[26] that the formation of δ-ferrite in creep resistance steel can be strongly suppressed by Co addition. The second violation can be attributed to the formation of austenite, which also correlates well with Helis' experimental work [26] showing that Co alloying significantly decreases the austenitisation temperature of creep resistance steels. At Co levels below 3.2%, the criterion of adequate Cr concentration in martensitic matrix is also violated, since Cr partially dissolves in austenite phase.

In figure 2.2b showing the optimal Co levels for $M_{23}C_6$ strengthened steels, the criterion of a sufficiently high-volume fraction of austenite at the austenisation temperature is violated at Co concentrations below 9.02 wt.% because of the presence of δ-ferrite. For Co levels above 12.8 wt.%, the criteria dealing with the matrix austenitic volume fraction and the absence of undesirable phases at the service temperature are not met due to the formation of detrimental Cr-rich σ phase. As in the Laves strengthened system, a reduction in the Cobalt concentration in the $M_{23}C_6$ system also leads to a decrease in precipitation hardening factor.
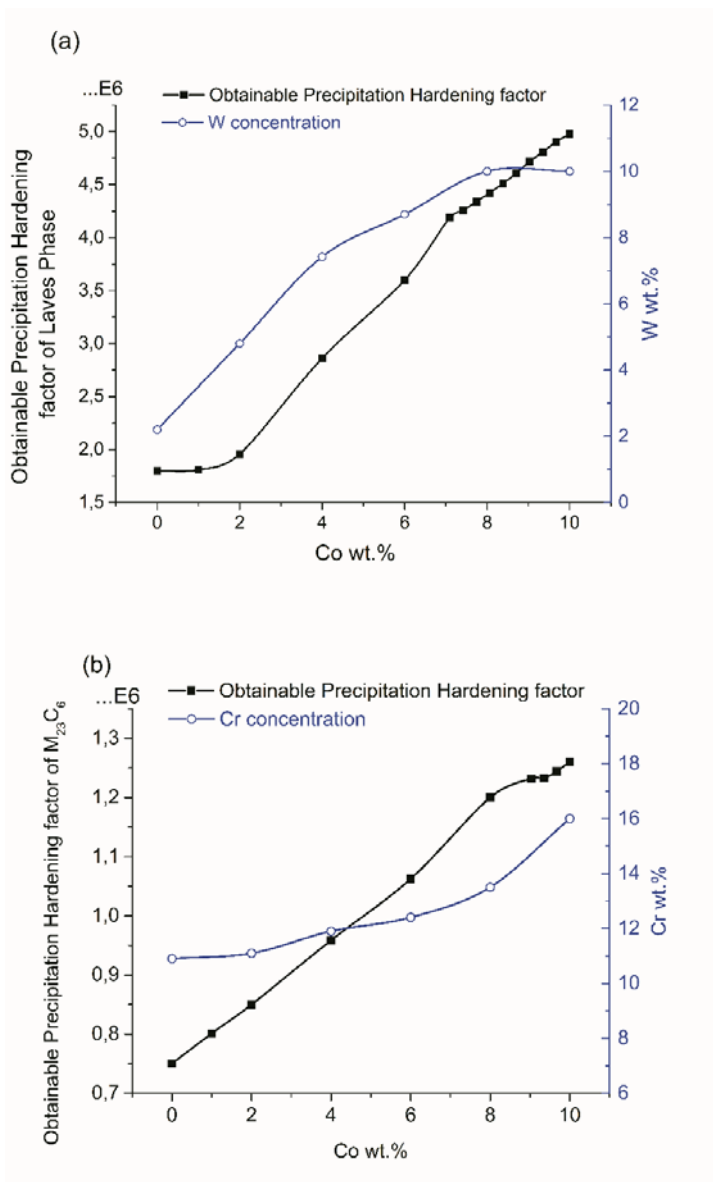
Figure 2.3 The optimal precipitation hardening factors obtained by employing different upper search limit of Co concentration, and the optimal concentration of alloying elements which are the most sensitive to Co variations in (a) Laves strengthened steels and (b) $M_{23}C_6$ strengthened steels.

Figure 2.2 demonstrates the effect of the Cobalt concentration by taking the compositions of the alloys LavesW and $M_{23}C_6$W as the baseline and by computationally increasing the Co level. In this case, the concentration of all other alloying elements was fixed while only Co level is changed at the expense of the Fe fraction. However, to further explore the complex interactions among different component and to find the possible alternative low Co solutions, a new series of optimization runs employing different upper Co limits are performed. The precipitation hardening factors of each obtainable solution, as well as the optimal concentration of alloying elements that varies most with Co change, are demonstrated in figure 2.3. As excepted, the predicted optimal Co concentrations can be found in the very upper limit of the search range in every optimization run.

Figure 2.3a shows that with a decrease in Co concentration from 10 to 0 wt.%, there is a nearly linear drop of precipitation hardening factors as a result of decreasing presence of the Laves phase. The amount of Laves phase present depends not only on the Co level but also on the W level. The optimal W concentration for a given Co level is also plotted in figure 2.3a and the figure shows that the optimal W concentration decreases only slightly at high Co levels but falls sharply when the Co concentration gets below 6 wt.%. Similarly, in figure 2.3b, the precipitation hardening factor of $M_{23}C_6$ carbides at 0 wt.% is only one-third of its original value at 10 wt.% Co. In this system the most sensitive element is Cr, of which the optimal concentration is also plotted in figure 2.3b. The figure shows that the optimal Cr concentration decreases only slightly with decreasing Co concentration.

By combining the results in figure 2.2 and figure 2.3, it can be concluded that the precipitation strengthening contributions in the current systems will inevitably degrade as the Co alloying decreases, even when taking into account the complex synergies of all alloying elements. In the next section, the relevant importance of the optimal W and Cr levels with respect to the Co level for both Laves and $M_{23}C_6$ strengthened steels will

be further discussed, in order to further evaluate the effectiveness of replacing Co by either W or Cr.

The chemical composition of LavesW alloy is taken as a baseline to present the binary analysis of Co and W while keeping the levels of other components constant. The composition domains of Co and W are extended to two times the original search range employed in the optimization so as to find out the general pattern. In figure 2.4, the background colour contour indicates the volume fraction (figure 2.4a), coarsening rate (figure 2.4b) and precipitation strengthening factor (figure 2.4c) of Laves phase, respectively, at the intended service time of 10^5 hours. To make a clear contrast, the levels of colour contour are normalized with respect to the maximum grade of each precipitation properties. In each figure, the black horizontal, black vertical and white horizontal slash patterns demonstrate the area not fulfilling the go/no-go criteria of volume fraction of austenite at T_{aus}, Cr concentration in the matrix and volume fraction of desirable phase at T_{aus} respectively. The white regions close to the W-axis contain compositions where Thermo-Calc equilibrium calculation cannot be successfully performed, while the central unmarked regions unveil the valid composition domains that meet all the constraints.

(a) Normalized volume fraction of Laves phase

(b) Normalized coarsening rate of Laves phase
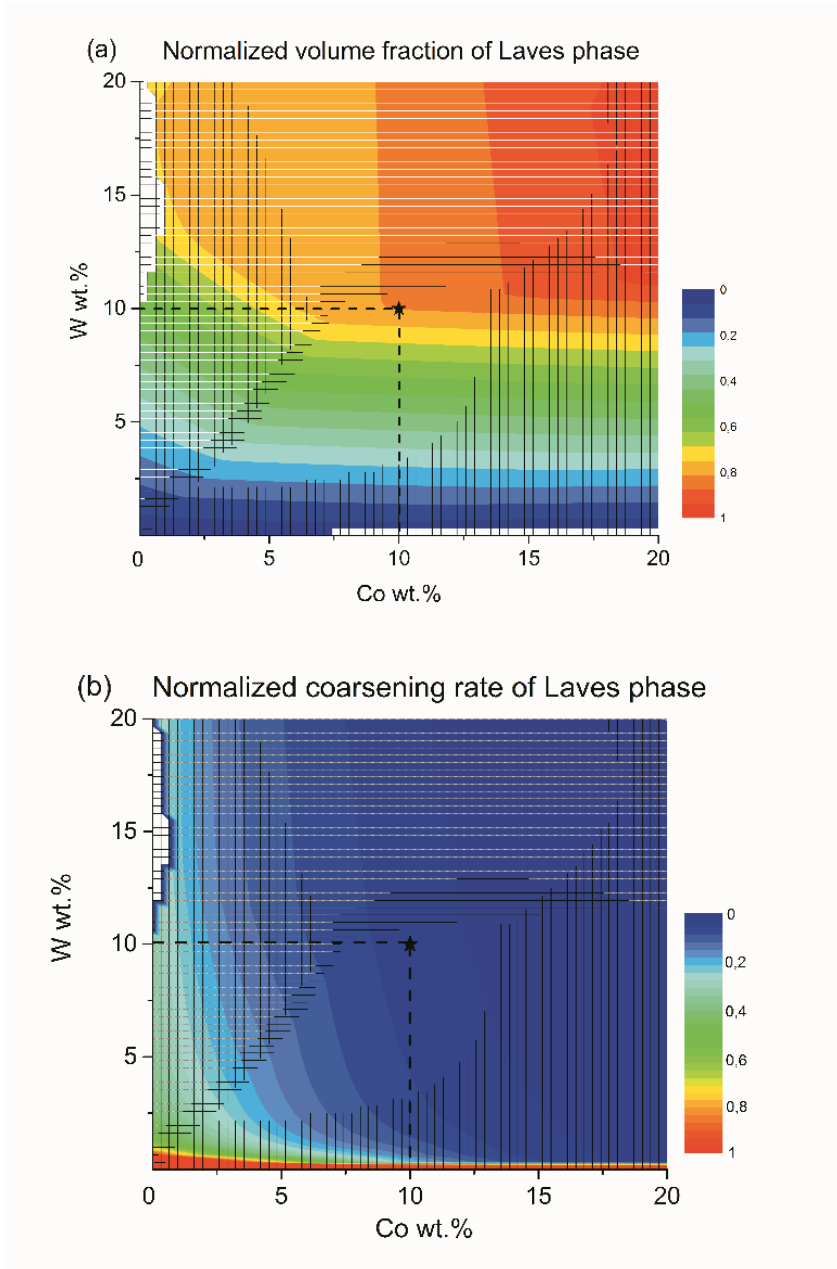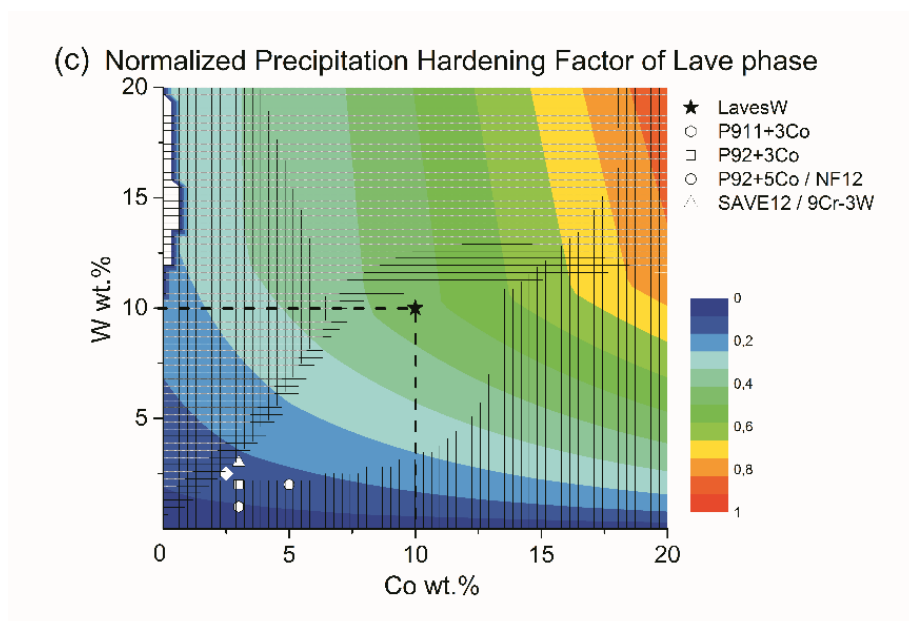
Figure 2.4. The binary isopleths of Co-W for the calculate LavesW composition showing the normalized (a)precipitation volume fraction, (b) coarsening rate and (c) precipitation hardening factor. The original upper limits of Co and W are marked by vertical and horizontal dashed lines respectively, and the black star symbols show the concentration value for the previously defined optimal LavesW alloy. The white symbols show the calculated performance of the marked commercial alloys.

In figure 2.4a, the background contours show that tungsten concentrations have the most important effect on the volume fraction of Laves phase as the colour band is nearly horizontal in the valid area. The results are fully understandable as W is the principle Laves phase forming element. Moreover, it can be observed in figure 2.4b that the coarsening rate contour is nearly vertical in the available area, which suggests the coarsening rate of Laves phase is more affected by the Co. Subsequently, figure 2.4c represents an inverse proportional pattern, as

precipitation hardening factor is a balance of volume fraction and coarsening rate. Therefore, it can be concluded that both Co and W play important roles in improving the precipitation hardening factor, i.e., W in increasing the volume fraction and Co in decreasing the coarsening rate; W can partially replace the Co to yield the same precipitation hardening level in the valid solution area.

As the positions of the black star symbol in figure 2.4c show, the concentrations of Co and W in LavesW alloy are at the upper limit of their original search domains. However, the background contour in the uncovered area indicates that further improvement can be achieved via increasing the searching upper limit of Co and W. Furthermore, the existing steels and the newly designed ones are pointed on figure 2.4c. It can be noticed that almost all existing alloys locate in the unmarked area, indicating the validity of the design strategy. Nevertheless, the compositions of the existing commercial alloys are concentrated in the band of a low precipitation hardening level, suggesting that the newly designed alloy can significantly outperform the existing steel grades.

(a)   Normalized volume fraction of $M_{23}C_6$ phase
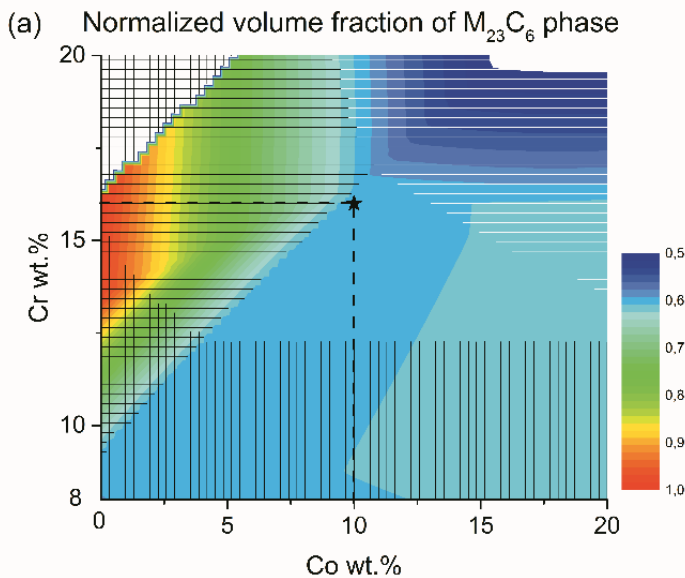
(b)   Normalized coarsening rate of $M_{23}C_6$ phase
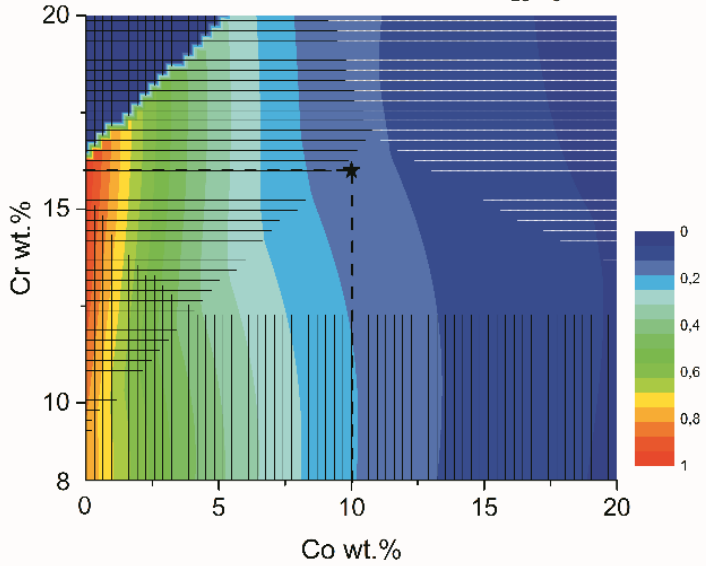
(c)   Normalized Precipitation Hardening Factor of $M_{23}C_6$
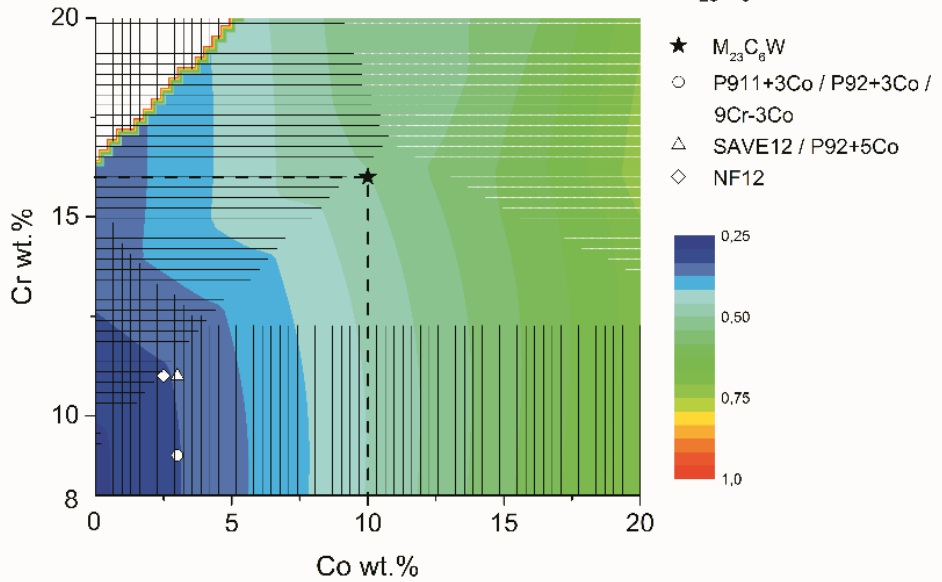
Figure 2.5. The binary effects of Co-Cr on the normalized (a)precipitation volume fraction, (b) coarsening rate and (c) precipitation hardening factor of $M_{23}C_6$ in $M_{23}C_6W$ alloy. The original upper limits of Co and Cr are marked by vertical and horizontal dashed lines respectively. The black star symbol shows the concentration value of the recommended $M_{23}C_6W$ alloy composition. The white symbols mark the predicted performance of existing commercial martensitic steel grades.

The same analysis is performed taking alloy $M_{23}C_6W$ as the baseline and varying the Co-Cr levels and the results are shown in figure 2.5. The same go/no go criteria patterns as defined for figure 2.4 are superimposed. The valid solutions form an un unmarked central area with a relative narrow Cr concentration and a wide Co variation. The $M_{23}C_6$ volume fraction patterns in figure 2.5b indicate that variations of Co and Cr contents do not lead to notable changes in the equilibrium volume fraction of $M_{23}C_6$ precipitates at the intended use temperature. Given the significant effect of Co in decreasing the coarsening rate of $M_{23}C_6$ carbides as shown in figure 2.5b, the precipitate strengthening factor in figure 2.5c is also nearly vertical and only sensitive to Co variation. Therefore, Co has an irreplaceable contribution to the precipitation hardening factor in $M_{23}C_6W$ alloy.

2.4 Conclusions

1. The newly designed alloys with high concentrations of Co and precipitation-forming elements remarkably outperform the existing alloys when exposed for 10^5 hours to a temperature of 650 ^{0}C. The improvement is due to a better combination of precipitation characteristics such as volume fractions, coarsening rates and precipitation strengthening factors.

2. The analysis of Co effects on the precipitation of Laves phase and $M_{23}C_6$ suggested that the precipitation strengthening contributions in these systems will inevitably degrade as the Co alloying decreases, even considering the complex synergies of all alloying elements.

3. W and Cr are found to be highly coupled with Co in Laves phase and $M_{23}C_6$ strengthening system respectively. In the case of Laves phase strengthened martensitic steels the calculations predict that Co can be partially replaced by W to yield the same precipitation strengthening level, while in $M_{23}C_6$ strengthened martensitic steels the long-term strength level cannot be tailored by adjustment of the Cr level and was found to depend on the Co level only.

Reference

[1]   Abe F. Curr Opin Solid St M 2004;8:305.
[2]   Sachadel U, Morris P, Clarke P. Mater Sci Technol-lond 2013;29:767.
[3]   Abe F, Kern T-U, Viswanathan R. Creep-resistant steels. Cambridge England: Woodhead Publishing, CRC Press, 2008.
[4]   Kaybyshev R, Skorobogatykh V, Shchenkova I. Phys Met Metallography 2010;109:186.
[5]   Vaillant J, Vandenberghe B, Hahn B, Heuser H, Jochum C. Int J Pres Ves Pip 2008;85:38.

[6]   Taneike M, Abe F, Sawada K. Nature 2003;424:294.
[7]   Yin F-S, Jung W-S. Metall Mater Trans A 2009;40:302.
[8]   Maruyama K, Sawada K, Koike J-i. Isij Int 2001;41:641.
[9]   Abe F, Horiuchi T, Taneike M, Sawada K. Materials Science and
        Engineering: A 2004;378:299.
[10]   Gustafson Å, Ågren J. Isij Int 2001;41:356.
[11]   Yamada K, Igarashi M, Muneki S, Abe F. Isij Int 2003;43:1438.
[12]   Shibuya M, Toda Y, Sawada K, Kushima H, Kimura K. Mater
        Sci Eng A 2011;528:5387.
[13]   Kipelova A, Odnobokova M, Belyakov A, Kaibyshev R. Metall
        Mater Trans A 2012;44:577.
[14]   Kipelova A, Belyakov A, Kaibyshev R. Mater Sci Eng A
        2012;532:71.
[15]   Xu W, Rivera-Díaz-del-Castillo P, Van Der Zwaag S. Philos
        Mag 2008;88:1825.
[16]   Lu Q, Xu W, van der Zwaag S. Metall Mater Trans A
        2014;45:6067.
[17]   Xu W, Rivera-Díaz-del-Castillo P, Wang W, Yang K, Bliznuk V,
        Kestens L, Van der Zwaag S. Acta Mater 2010;58:3582.
[18]   Fedoseeva A, Dudova N, Glatzel U, Kaibyshev R. J Mater Sci
        2016;51:9424.
[19]   Agamennone R, Blum W, Gupta C, Chakravartty JK. Acta Mater
        2006;54:3003.
[20]   Dudova N, Plotnikova A, Molodov D, Belyakov A, Kaibyshev R.
        Mater Sci Eng A 2012;534:632.
[21]   Abe F, Horiuchi T, Taneike M, Sawada K. Mater Sci Eng A
        2004;378:299.
[22]   Viswanathan R, Bakker W. J Mater Eng Perform 2001;10:81.
[23]   Lu Q, Xu W, van der Zwaag S. Philos Mag 2013;93:3391.
[24]   Lu Q, Xu W, van der Zwaag S. Acta Mater 2014;77:310.
[25]   Kipelova A, Kaibyshev R, Belyakov A, Molodov D. Mater Sci
        Eng A 2011;528:1280.
[26]   Helis L, Toda Y, Hara T, Miyazaki H, Abe F. Mater Sci Eng A
        2009;510-511:88.

On the relationship between the Chromium concentration, the Z-phase formation and the creep strength of ferritic-martensitic steels

In this study the long-term creep strength behaviour of commercial heat resistant martensitic/ferritic steels with Cr levels ranging from 1 to 15 wt.% is analysed by linking their computed equilibrium compositions to their creep properties. At lower Cr levels the calculated strength due to precipitation hardening agrees well with the experimental results. At high chromium levels and longer exposure times an accelerated strength loss due to the formation of Z-phase precipitates has been reported. The accelerated strength loss is computationally analysed and a correlation between accelerated strength loss and Z phase formation is confirmed. A study is made to explore the option of adjusting the chemical composition of existing high-chromium steels to reduce the driving force for Z-phase formation. However, no proper composition ranges are found which combine a high Cr concentration with a significantly lower driving force for Z-phase formation.

3.1 Introduction

Creep resistant steels that combine a high creep strength with a high corrosion and oxidation resistance are a key requirement for the construction of efficient and long-lasting power plants. Power plant design has sought to increase the overall fuel efficiency by bringing the operating conditions to higher pressures and temperatures. The increase in the severity of the operating conditions has led to ongoing research into the development of creep-resistant steels with even more outstanding mechanical properties and corrosion resistance at elevated temperatures[1]. The development has also led to a renewed interest in understanding the role of chromium concentration in the time dependent creep strength.

Low-alloy ferritic/bainitic steels with low chromium and molybdenum levels (1/2Cr1/2Mo, 1CrMo, 2CrMo etc.), which were developed at the beginning of the 1920s, were commonly used for the components of the first-generation power station boilers. It was general practice to use these steels for installations with a service temperature between 450-500°C and a pressure of 35 bar[2]. However the increase in service temperature and service pressure has necessitated the raise of the chromium level in such steels. Progress in recent years has led to the development of high-strength 9–12% Chromium martensitic steels[3, 4]. Their high creep strength at 600 ^{0}C is guaranteed by the tempered martensitic matrix, containing solid solution strengthening alloying elements and particle strengthening with carbonitrides[5-7]. With higher operating temperatures approaching 650°C, even higher Cr levels are required for better oxidation resistance. To ensure a fully martensitic microstructure, the increased chromium content has to be balanced by the addition of elements that stabilize the austenite phase without reducing the ferrite/austenite transformation temperature. Cobalt and copper have been the favoured additions and the newer 12% chromium steels usually contain one of these elements. However, attempts to apply 12% Cr steels

at 650°C have largely failed, since under this condition the fine MX particles which provide a major strengthening contribution transform into relatively coarse Z-phase particles[8-10]. The development of Z-phase has been held responsible for the decrease in long term creep properties as well as the decrease in corrosion resistance, since the formation of Z-phase not only causes the dissolution of desirable MX precipitates[11], but it also might consume some of the chromium in solid solution in the matrix which is required for the formation of a corrosion resistant surface layer. In Hald's research[10], one possible solution to avoid Z-phase in high Cr steels is to eliminate the Z-phase forming elements such as V and Nb and replace them by Ti, since TiN is the only nitride in steels which cannot transform into Z-phase. However, the TiN nitrides generally do not make a significant contribute to the high temperature strength, hence, the problem how to suppressing Z-phase formation in heat resistant martensitic steels with high Cr levels (Cr wt.%>11) operating under a prescribed service temperature of 600-650°C still remains unsolved[12].

The development of creep resistant steels functioning at higher temperatures required a new concept for high chromium steel[13], and led to the development of fully ferritic steels with a chromium content of 14% or more, not undergoing a martensitic transformation. Due to the extremely low solubility of carbon and nitrogen in ferrite, it will not be possible to produce a significant and stable dispersion of strengthening carbides and nitrides. Instead, intermetallic phases, such as the Laves phases, should be considered provided that such precipitates are sufficiently fine and resistant to coarsening at the applied temperatures. To validate the feasibility of a ferritic matrix, Kimura et al[14]. have investigated the effect of initial microstructure on the long-term creep strength, assuming that fully annealed steels with a ferritic matrix and a relatively low dislocation density would perform better under long-term service conditions. Based on this concept, novel ferritic steels with 15% Cr level have been developed in which the precipitation strengthening is due to intermetallic compounds[15]. However, as stated above the

formation of strengthening intermetallic particles consumes Cr in solid solution. Also, a high level of Cr leads to a microstructural instability and strongly promotes the formation of a detrimental Z-phase during long time creep exposure. Whether the remaining Cr content in the matrix can ensure the long term oxidation resistance at elevated service temperature appears doubtful[16]. As on the one hand a sufficiently high Cr level is beneficial for high temperature corrosion and oxidation stability, while on the other hand an increase in Cr level promotes the formation of a detrimental phase, it is useful to analyse the possibility to tailor the overall chemical composition of high Cr ferritic steels to reduce the tendency to Z-phase formation.

The present study is a thermodynamic/computational analysis of both the creep strength behaviour as a function of the Cr level over the range 1-15 wt.% and an exploration of compositional modifications to reduce Z-phase formation in 15 wt.% Cr steels to be used at 650^0C or above.

3.2 Results and discussion

3.2.1 Existing martensitic/ferritic steel with different Cr level

Table 3.1 shows the chemical composition of some existing heat resistant steels listed in order of their Cr level[2, 15, 17-19], and decade in which the steel was introduced in the market is reported[1, 2]. for the commercial grades, the specification ranges of their alloying elements are listed as well. As mentioned above, these heat resistant steels can be roughly divided into three groups: Low-alloy ferritic steels (1-4%Cr); 9-12Cr martensitic steels and 15Cr ferritic steels. The chemical compositions of the low-alloy ferritic steels are quite similar in their C, Si, Mn and Mo levels, yet have different Cr levels. Si is a ferrite former whereas Mn is an austenite former. The Mn/Si balance controls the high temperature stability of the ferritic matrix and also contributes to a

proper toughness. The addition of Mo provides some solid solution strengthening, thereby effectively enhancing the creep properties[20].

With respect to 9-12Cr steels, the 15Cr steels are more heavily alloyed to achieve better high-temperature mechanical properties. All high Cr alloys contain a similar alloying level of V, Nb and N, which produces finely distributed MX carbonitrides and a remarkable precipitation strengthening. In contrast, the alloying levels of Mo and W vary with the different steel grades. These elements not only act as solid solution strengtheners but also as Laves phase formers, in order to provide particle strengthening. The addition of austenite stabilizers such as Co, Ni and Cu, to high-Cr grades (Cr%>11%), aims to maintain the Cr equivalent while inhibiting the formation of δ-ferrite. The Boron addition, according to the literature[21, 22], helps to retard the coarsening of the $M_{23}C_6$ carbides near the prior austenite grain boundaries, which decreases the minimum creep rate and increases the time to rupture. As shown in table 3.1, the 15Cr ferritic steels are relatively highly alloyed with Mo, W and Co compared to 9-12Cr grades, the effect of which on the mechanical properties will be discussed in the next section.

Table 3.1 Chemical composition of existing Cr steels grades (in wt.%, with Fe to balance), and year of conception when the steel was introduced in the market. The first value per element is the lowest specification range; the bold middle value is the value used in calculation; the final value is the highest specification range per element.

	C	Si	Mn	Cr	Mo	W	V	Nb	B	N	others	Year of conception
P11/STBA22[17]	0</**0.15**/ ≤0.15	0.50</**0,65**/<1.00	0.30</**0,50**/<0.60	0.90</**1.00**/<1.10	0.45</**0,50**/<0.65							1920s
STBA23 [17]	0</**0.15**/ ≤0.15	0.50</**0,65**/<1.00	0.30</**0,45**/<0.60	1.00</**1,25**/<1.50	0.45</**0,50**/<0.65							1920s
P22/STBA24[17]	0</**0.15**/ ≤0.15	0</**0.50**/ ≤0.50	0.30</**0,45**/<0.60	1.90</**2,25**/<2.60	0.87</**1.00**/<1.18							1930s
STBA25 [17]	0</**0.15**/ ≤0.15	0</**0.50**/ ≤0.50	0.30</**0,45**/<0.60	4.80</**5.00**/<5.20	0.45</**0,50**/<0.65							1930s
P9/STBA26[17]	0</**0.15**/ ≤0.15	0</**0.50**/ ≤0.50	0.30</**0,45**/<0.60	8.00</**9.00**/<10.00	0.90</**1.00**/<1.10							1940s
P91[1]	0.08</**0,10**/<0.12	0</**0,40**/ ≤0.50	0.30</**0,45**/<0.60	8.00</**9.00**/<9.50	0.85</**1.00**/<1.05		0.18</**0,20**/<0.25	0.06</**0,08**/<0.10		0.03</**0,05**/<0.07		1970s
P92[1]	0.07</**0,10**/<0.13	0</**0,50**/ ≤0.50	0.30</**0,45**/<0.60	8.50</**9.00**/<9.50	0.30</**0,50**/<0.60	1.50</**1,80**/<2.00	0.15</**0,20**/<0.25	0.04</**0,08**/<0.09	0.001</**0,004**/<0.006	0.03</**0,05**/<0.07		1980s

MARN[18]	**0,08**	**0,30**	**0,50**	**9**		**3.00**	**0.20**	**0.05**		**0.008**	**3.00Co**	1990s
NF12[1]	**0,10**	**0,20**	**0,50**	**10**	**0,15**	**2,60**	**0,20**	**0,06**	**0.004**	**0,07**	**2,50Co**	1990s
SAVE12 [19]	**0,10**	**0,25**	**0,25**	**11**		**3.00**	**0,20**	**0,07**	**0.006**	**0,03**	**3.00Co, 0,10Ta,0 .04Nd**	1990s
P122[1]	0.07</**0, 11**/<0.14	0</**0,10**/ ≤0.50	0</**0,60**/ ≤0.70	10.00</**1 2.00**/<12 .50	0.25</**0, 40**/<0.60	1.50</**2. 00**/<2.50	0.15</**0, 20**/<0.30	0.04</**0, 05**/<0.10	0.0005</ **0,003**/<0 .005	0.040</**0 ,06**/<0.1 00	**1.00Cu**	1990s
15Cr3W 3Co[15]	**0,10**	**0,25**	**0,50**	**15**	**1.00**	**3.00**	**0,20**	**0,05**	**0,003**	**0,08**	**3.00Co**	2000s
15Cr6W 3Co[15]	**0,05**	**0,22**	**0,50**	**15**	**1.00**	**6.00**	**0,19**	**0,045**	**0,003**	**0,033**	**3.00Co**	2000s

Table 3.2 The calculated microstructure of existing Cr-containing steels at 650°C (in vol.%, F indicates Ferrite and M indicates Martensite, with matrix to balance).

Grades	Matrix	Precipitates			
		$M_{23}C_6$	Laves	Z phase	Others
P11/STBA22	F	2.84	-	-	
STBA23	F	2.82	-	-	
P22/STBA24	F	2.95	-	-	
STBA25	F	2.96	-	-	
P9/STBA26	F	3.00	-	-	
P91	M	1.99	-	0.60	
P92	M	1.40	1.10	0.50	
MARN	M	1.56	1.71	0.25	0.02NbC
NF12	M	2.00	1.63	0.64	0.18M_2N
SAVE12	M	1.85	1.99	0.37	0,07TaC
P122	M	2.20	1.35	0.67	0.08M_2N
15Cr3W3Co	F	2.00	3.10	0.59	0.31M_2N
15Cr6W3Co	F	1.00	6.70	0.50	

The equilibrium phase fractions of the various strengthening phases (in vol.%) at a service temperature of 650°C as calculated by Thermo-Calc are listed in table 3.2. Here the thermodynamic calculation ignores the effects of applied stresses on their equilibrium phase configuration, since the simulation of stress field is beyond the ability of Thermo-Calc calculation. For low-alloy steels with a ferritic matrix, only $M_{23}C_6$ carbides play a significant role as strengthening particles,

and the amount of $M_{23}C_6$ particles increases slightly with the addition of Cr. Despite the difference in chemical concentration, the 9-12%Cr steel grades share an almost identical as-tempered martensitic matrix. The characteristics of the precipitates present, such as the $M_{23}C_6$ or the Laves phase, intrinsically determine the creep properties during service, as the precipitates pin the movement of dislocations, i.e. reduce the creep rate, and retard the recovery of martensitic lath boundaries. Compared to low-alloy steels, the higher amount of precipitates in 9-12%Cr steels provides a considerable contribution to the high-temperature properties. According to the thermodynamic calculations the undesirable course Z-phase particles can be present in 9-12Cr and 15Cr steels, while no MN phases are identified. The reason is that MN nitrides are thermodynamically less stable than the Z-phase according to Danielsen's research[8, 23]. The precipitation of Z-phase at the expense of MN nitrides has been confirmed as the root cause of the observed premature failure during long-time creep test. 15Cr steels contain a higher amount of Laves phase particles which act as their major strength contributor.

3.2.2 Creep properties of existing martensitic/ferritic steel
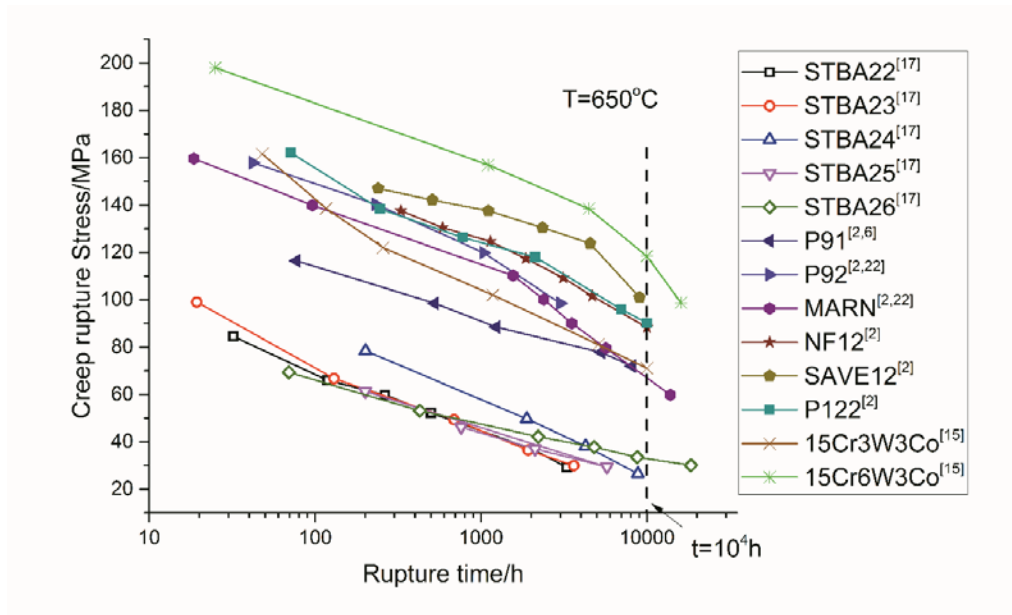
Figure 3.1 Stress-rupture data for heat resistant steels at 650°C.

Figure 3.1 shows the reported creep strength values of existing Cr-containing steels as a function of time at a fixed temperature of 650°C[2, 6, 15, 17, 24]. As intended, the low-alloying heat resistance steels show a much lower creep rupture stress compared to high Cr containing steels for a given rupture time, since low alloying steels are designed to operate at the temperature below 500°C. Within the low-alloyed steel group, only minor differences in creep properties can be found. The complex dependence of creep properties on alloying conditions and service condition can hardly be analysed systematically, and the effect of Cr content on creep properties is largely submerged in the other influencing factors. The creep curves show that the 15Cr6W3Co, SAVE12, NF12 and P122 commercial and pre-commercial grades perform better than the other counterparts. A qualitative analysis by

combining Figure 3.1 with the results in tables 3.1 and 3.2, the mentioned steels performing better generally contain higher levels of W+Mo, leading to higher amounts of Laves phases present. The contributions of the W, Mo-enriched Laves phase to the creep performances will be analysed in the following section. Finally, a remarkable drop in creep strength at longer creep time can be found in 15Cr6W3Co, SAVE12 and P122 steels. The reason for the reduction in strength will be computationally analysed.

As grain boundary strengthening does not play a major role in creep resistant steels, the precipitation hardening and solid solution strengthening are the most effective methods to raise the creep strength. In our previous work, the precipitation strengthening contribution in creep resistant steels has been shown to be inversely proportional to the inter-particle spacing, which in general is a function of the particle volume fraction, the initial particle size and coarsening kinetics of the precipitates[25-27]. The following expression is used to calculate the time-dependent precipitate strengthening factor while taking into account precipitate coarsening and its temperature dependence:

$$\sigma_p \propto 1/L = \sqrt{f_p}/r = \sqrt{f_p}\Big/\sqrt[3]{r_o^3 + Kt} \tag{1}$$

$$\gamma_0 = 2\gamma/\Delta G_V \tag{2}$$

$$K = 8\gamma V_m^p \Big/ \sum_{i=1}^{n} \frac{9(x_i^p - x_i^{mp})^2}{x_i^{mp} D_i} \Big/ RT \tag{3}$$

where L is the average inter-particle spacing, f_p is the equilibrium volume fraction of the strengthening precipitates at the service temperature, r_0 is the critical precipitate nucleus size, γ is matrix-precipitate interfacial energy, ΔG_v is volume thermodynamic driving force for the precipitation. V_m^p is the molar volume of precipitate. K is the factor of coarsening rate and t is the exposure time at the high temperature. x is equilibrium interface mole fraction of the precipitation former elements on both matrix (m) and precipitate (p) sides. T is the service temperature and D is the corresponding diffusion coefficient. In the calculations the interfacial energy is arbitrarily set at a fixed value of 1 J/m^2 irrespective of the precipitate size or type. This is a slight simplification but helps in illustrating the effect of precipitate coarsening. All thermodynamic parameter values including f_p, ΔG_v, x_i^p, x_i^{mp}, D_i and V_m^p required during the calculations were calculated via Thermo-Calc using the TCFE6 and MOBFE1 databases. The equation shows that the highest strengthening factors are obtained for high volume fractions and small and constant precipitate sizes, i.e. precipitates showing a very low coarsening rate. The computational details of the model and its application to MX precipitation strengthened creep resistant steel design can be found elsewhere[25-27]. In the present calculations the temperature and the creep time are fixed at 650^{0}C and 10^4 hours respectively.

With respect to solid solution strengthening, the solid solution strengthening factor was taken to be the weighted contribution of atomic concentration of solutes, which can be formulated as

$$\Delta\sigma_{ss} = \alpha \sum_i S_i x_i^{mp} \qquad \textbf{(4)}$$

Where α is a temperature dependent scalar, and S_i is the (room temperature) solid solution strengthening coefficient which combines size misfit and modulus misfit effect. For the solid solution elements in this work, the strengthening coefficients at room temperature were

determined from literature data on binary Fe-M systems and actual values are shown in table 3.3[28, 29]. Although in the reliable ranking of the alloy the actual value of α does not play a role, a value of α=0.25 was used based on the calibration study in literature[30].

Table 3.3 Strengthening coefficient for alloying elements at room temperature (MPa per at.%) [28, 29].

Element	C	N	Si	Ni	Ti	Mn	Mo	W	Al	Cr	Co	V
Si	1103.45	1103.45	25.80	19.20	17.90	16.90	15.90	31.8	9.00	2.60	2.10	2.00

The precipitation strengthening factors after 10^4 hours at 650^0C due $M_{23}C_6$ and Laves phase contributions as well as the solid solution strengthening factors for the selected Cr containing steels are shown in Figure 3.2. It can be seen that the solid solution strengthening factor of all steels, marked by blue dots, fluctuates between 49 and 70 among all the grades. The much larger differences in creep strength shown in Figure 3.1 are mainly due to the difference in the contributions of precipitation strengthening. The black and red bars in Figure 3.2 shows that no great difference in the strengthening effect of $M_{23}C_6$ carbides can be found amongst the heat resistant steels, while the Laves phase makes significantly different contributions to the creep strengthening. The sum of the precipitation strengthening factors matches the creep properties in Figure 3.1 with a reasonable sequence, which shows that 15Cr6W3Co performs best, followed by SAVE12 and NF12 alloys. The reason why only $M_{23}C_6$ and Laves phase are considered as strengthening phases in this calculation and the MX carbonitrides are ignored is due to the selected service time $(t = 10^4 \text{ h})$ which in high Cr steels $(\text{Cr}\% \geq 12)$ is sufficiently long for completion of the Z-phase formation depleting the MX carbonitrides population.[12] The coarse Z-Phase precipitates do not contribute to the creep strength (i.e. at best do not introduce

premature cracking) and are therefore also left out in the summation of strengthening factors. It should be mentioned that for the 9-11%Cr creep resistant steels the formation of Z-phase will not be finished completely in 10^4 hours as a result of the lower thermodynamic driving force at lower Cr concentrations.[12] The result indicates that the calculated precipitation strengthening factors for P91, P92, NF12 and SAVE12 steels are underestimates since the contribution from retained MX carbonitrides is ignored.
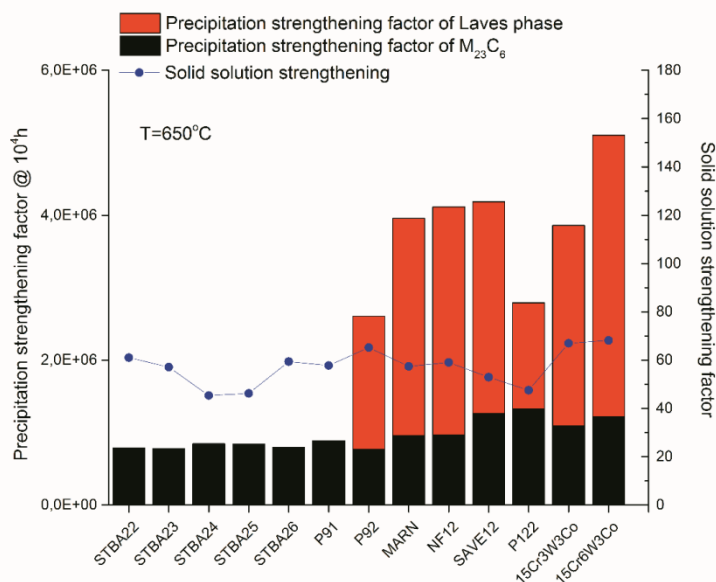
Figure 3.2 The calculated precipitation strengthening factor of $M_{23}C_6$ and Laves phase in existing Cr containing steels, at the temperature of $650^{o}C$ and service time of 10^4h; and the calculated solid solution strengthening factor of existing Cr containing steels.
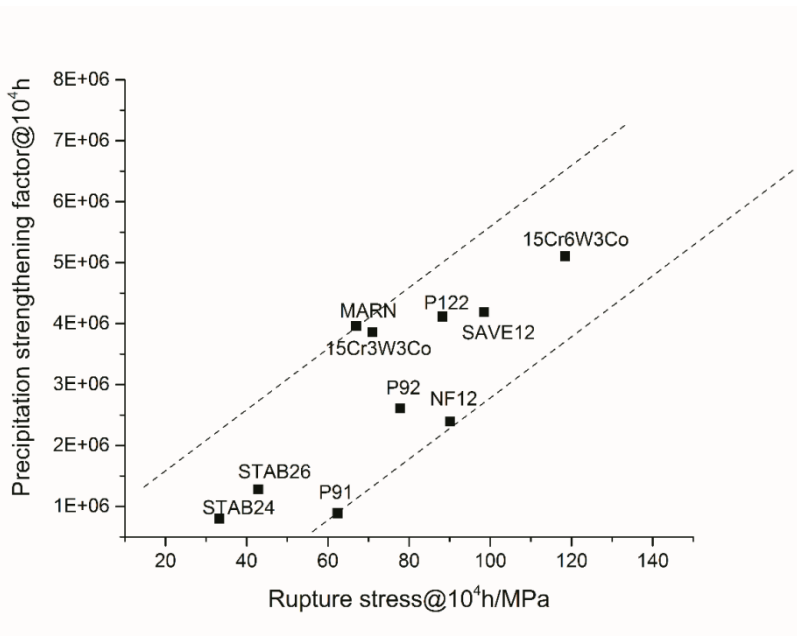
Figure 3.3 The calculated precipitation strengthening factor versus the experimental creep rupture for selected steels, both for exposure to 650^0C for 10^4h.

In Figure 3.3 the experimental creep rupture stresses at 10^4 h obtained from the curves in Figure 3.1 are compared with the calculated precipitation strengthening factors from Figure 3.2. All data are within a linear scatter band as indicated by the two parallel dotted lines. As mentioned previously, the pre-set time 10^4 h is not sufficient long for complete Z phase transformation in relative low-Cr (Cr%<12) steels. As a result, the precipitation strengthening factors of P91, P92, NF12 and SAVE12 steels are underestimates due to effects of retained MX not being taking into account in the calculations. This is corresponding to the data points for P91, P92, NF12 and SAVE12 steels on the lower limit of the parallel dotted line. This suggest that a better linear relationship can be expected if the as yet non-quantifiable contributions of MX and Z-phase precipitates were taken into account. Nevertheless,

by employing the current precipitation strengthening factor as the creep strength indicator and taking the contributions of solid solution strengthening as more or less constant, the model predicts the relative ranking of the selected commercial and pre-commercial steel grades rather well.

3.2.3 The microstructural changes as a result of Z-phase formation

The formation of Z-phase and its consequence for so-called premature failure has been mentioned repeatedly in the literature when the experimental creep data and the corresponding changes in the microstructure were analysed and correlated. To have a better understanding of the effect of Z-phase formation on the precipitate population, the thermodynamically calculated precipitate volume fractions in our selected heat resistant steels are plotted in Figure 3.4 with either the Z-phase computationally suppressed or allowed. The results show that for the alloys P91, MARN, SAVE12 and 15Cr6W3Co, the Z-phase develops solely at the expense of the strengthening MX particles. For the P92, NF12, P122 and 15Cr3W3Co alloys, the Z-phase not only originates from MX carbonitrides but also from M_2N particles. The predictions that M_2N nitrides partially transform into Z-phase particles agrees well with experimental observations.[31, 32] However, no clear relationship between the maximum volume fraction of MX particles and the maximum amount of final Z-phase particles is found. To get this correlations clearer a further investigation of the dislocation-pinning characteristics of consumed MX and the Z-phase particles formed would be required.
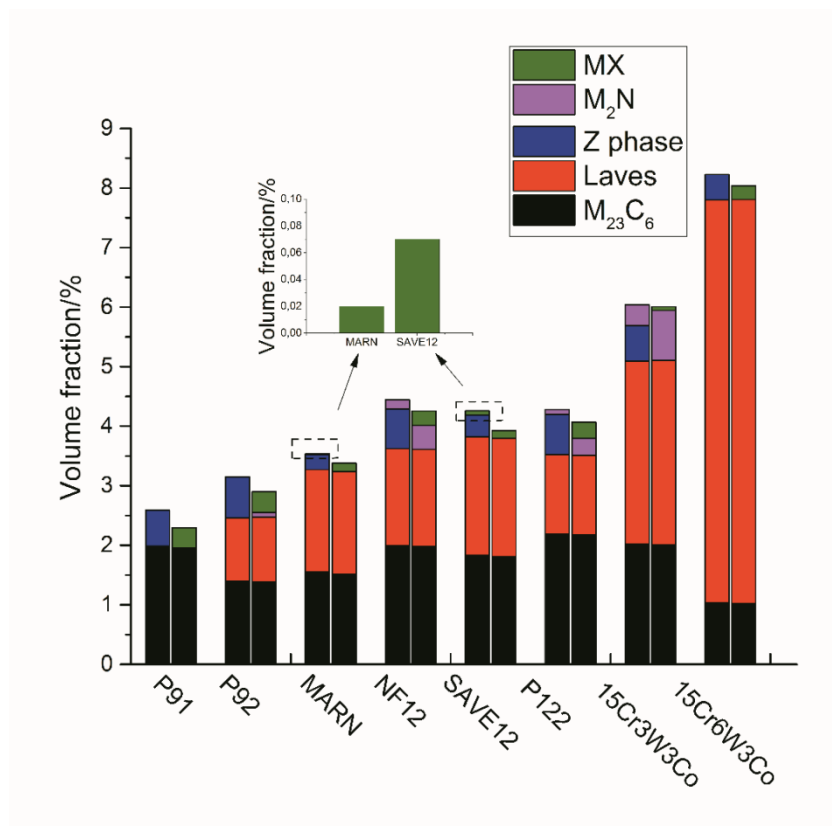
Figure 3.4 The calculated equilibrium precipitate populations (columns on left) and the precipitate populations with Z phase being computationally suppressed (columns on right) for heat resistant steels.

3.2.4 The strength loss due to Z-phase formation
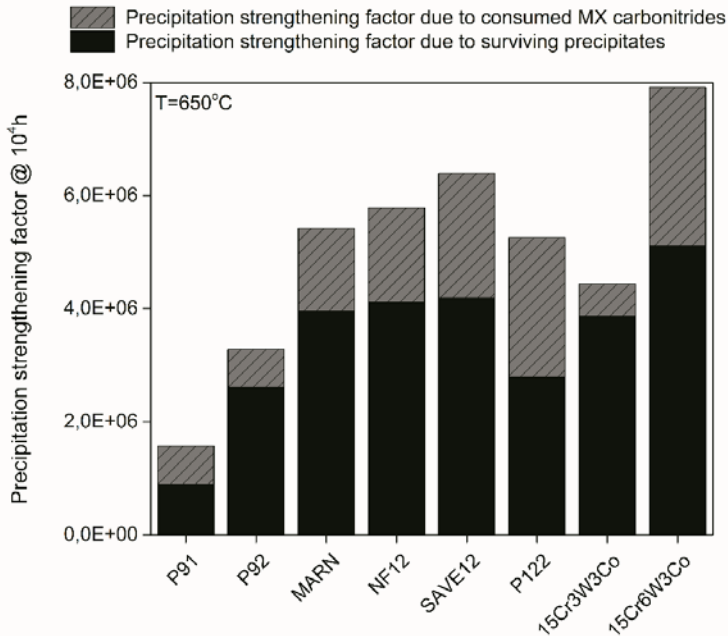
Figure 3.5 The calculated precipitation factor after 10^4 hours due to the surviving precipitates ($M_{23}C_6$+Laves phase) and the MX carbonitrides to be consumed in the Z-phase formation.

In the experimental creep curves shown in Figure 3.1 some steels show an accelerated degradation of the creep strength at long exposure times. To relate the accelerated strength loss to the Z-phase formation, the total precipitation strengthening factor is decomposed into its constituent terms using the results of the calculated microstructural changes shown in Figure 3.4. The black columns in Figure 3.5 present the "stable strength" which is contributed by the equilibrium (i.e. surviving) Laves phase and $M_{23}C_6$ carbides, while the grey columns marks the

contribution of the MX carbonitrides to the precipitation hardening before they are transformed into non-strength-contributing Z-phase particles. For the MARN and SAVE12 steels, only very small amounts of stable MX strengthening carbides are present. In the calculations the (negative) contributions of both newly formed Z phase and M_2N nitrides to the precipitation hardening factor are neglected, thus the sum of two represents the "ideal" precipitation hardening contribution. The results show that the precipitation related strength component of commercial grades P91 and P122 is almost halved after Z-phase formation, while NF12, SAVE12, MARN and 15Cr6W3Co steels only 1/3 of their precipitation strength is lost due to the disappearance of MX particles. The significant strength loss in precipitation strengthening factor as a result of the Z-phase formation encouraged us to conduct a more detailed analysis of the driving force for Z-phase formation.

3.2.5 The driving force for the Z-phase formation

Chromium has the most significant effect among all the alloying elements on the kinetics of Z-phase formation. [8] Experimental observations[12] show that in a 12%Cr steel the Z-phase precipitated 20 to 50 times faster than in 9%Cr steel, which is supported by a theoretical model indicating that an increase in Cr level strongly accelerates the Z-phase formation.[23] Figure 3.6 shows the calculated driving force for Z-phase formation in exiting heat resistant steels, as well as the calculated upper and lower limit of Z-phase driving force with specification permitted C concentration differences as a function of Cr concentration in matrix as at 650°C. From the middle black dash line in Figure 3.6, a clear linear relationship can be found between the calculated driving force of Z-phase in the selected steels and the Cr concentration in the matrix, which demonstrates that alloys with a high solid Cr concentration in solid solution are more prone to have a rapid Z-phase precipitation, while the transformation in low Cr steels should be
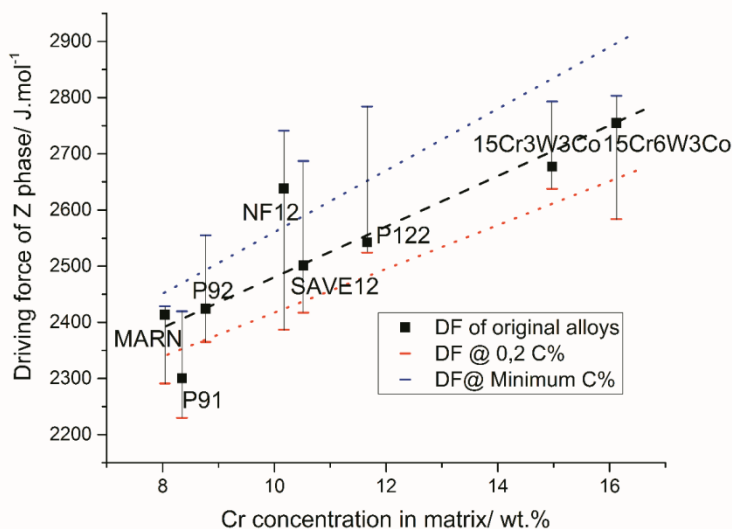
Figure 3.6 The calculated driving force for Z-phase formation in exiting heat resistant steels (in black dash line), as well as the calculated upper and lower limit of Z-phase driving force with specification permitted C concentration differences (in blue and red dot lines), as a function of Cr concentration in matrix as at 650^0C

more sluggish. Danielsen's simulation results[23] show that only Cr and C have a significant influence on the kinetics of Z phase formation, while the effect of other Z phase forming elements such as Nb, Mo and V was found to be minor. The changes in Z phase driving force as a function of the specification permitted C- content variations are shown in Figure 3.6 for the selected heat resistant steels. The blue spots mark the upper limit of Z phase driving force for the minimum concentration of C concentration allowed in the steel specifications, while the red spots mark the Z phase driving force for highest permitted C concentration. The blue and red dotted lines mark the variation range of the driving force in Z phase transformation for the existing steels. The results indicate the possibility to reduce the driving force of Z phase through

tuning their element concentration. However, the adjustment in chemical concentration may cause complex synergies in thermodynamic as well as microstructural properties. The feasibility of element adjustment to lower the driving force for Z phase formation will be discussed in the following paragraph.

3.2.6 Exploring the option to reduce the Z-phase formation at high Cr levels

While on the one hand a high Chromium level is desirable because it leads to a better corrosion and oxidation resistance as well as a higher initial strength, a high Cr level also leads to a high driving force for Z-phase formation and hence a more significant strength loss at long creep times. In Figure 3.7 the calculated driving force for Z-phase formation at 650^0C as a function of the two dominant alloying elements for Z-phase formation Cr and C[23] has been plotted, for two high Crsteels P122 and 15Cr6W3Co (see table 3.1 for the concentration values for the other alloying elements) which showed the steepest drop in creep strength due to Z-phase formation. Using a graphical presentation mode first presented in reference[33] in each Figure, not only the driving force is presented via the background colour contour but for each composition the thermodynamically predicted occurrence of other undesirable microstructural phenomena which would have a very negative effect on the creep performance, is indicated by different forms of shading. The black horizontal, black vertical and white vertical slash patterns mark the domains where a) the volume fraction of austenite at the homogenisation temperature is less than 99% (i.e. δ ferrite or big primary carbides are present); b) the Cr concentration in the matrix below 12% after formation of all equilibrium precipitates (i.e. the corrosion resistance would be poor); and c) the volume fraction of undesirable intermetallic phase (excluding matrix, Laves phase and $M_{23}C_6$ particles) at 650^oC is higher than 1%. The white regions close to the Cr-axis contain
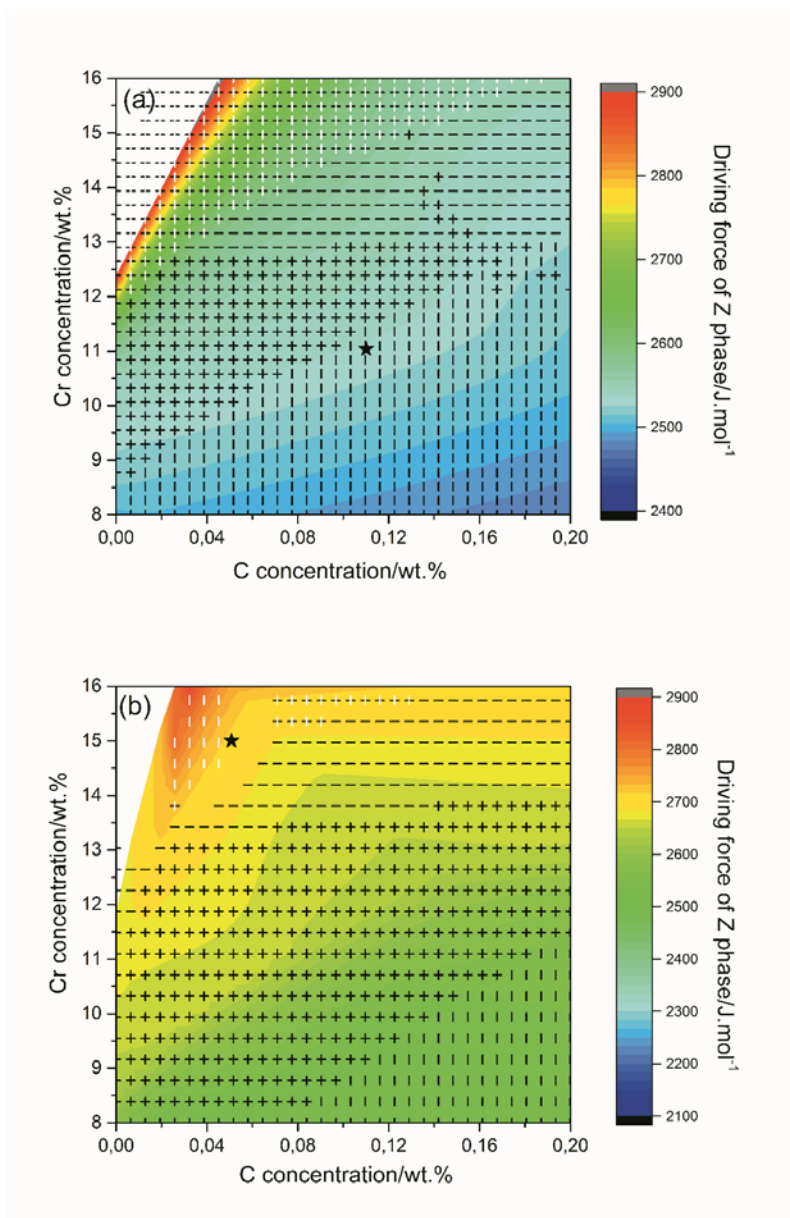
Figure 3.7 The binary isopleths of C-Cr for the calculated driving force of Z-phase in commercial grades (a) P122 and (b) 15Cr6W3Co steels. the black star symbols show the nominal concentration values for the P122 and 15Cr6W3Co alloys respectively.

compositions where Thermo-Calc equilibrium calculation cannot be successfully performed. An unmarked area would mark a composition region which would lead to the absence of undesirable microstructural phases and hence to optimal creep strength properties.

In Figure 3.7a, the background colour contours show that Z phase driving force rises with the increase of Cr concentration, while decreases as the C content increases, in agreement with the work by Danielsen. The Figure shows that (given the temperature of 650^0C and the other alloying element concentrations being at the level of those of the base alloy P122) there are no compositional domains which satisfy all constraints. The nominal P122 composition is located in the place where Cr concentration in solid solution in the matrix after formation of all precipitates is below the set level of 12%. In the middle area, the development of δ-ferrite consumes too much Cr in the matrix which reduces the volume fraction of austenite at the homogenisation temperature to unacceptably low levels, thereby preventing the formation of a uniform martensitic microstructure. In the upper part of the Figure, high amounts of Z phase and σ phase are responsible for unattractive properties. The Figure clearly shows the P122 composition has some intrinsic deficiencies and a high tendency to form Z-phase but these characteristics cannot be resolved by adjustments in Cr or C level (nor by modest adjustments in any of the other alloying elements; results not shown but calculations performed).

In Figure 3.7b, a very narrow unmarked area can be found at the top left corner of the whole area, close to the nominal composition of 15Cr6W3Co steel, and this indicates that the composition of this steel grade is very well selected, but also that the steel has a high tendency to form Z-phases. This prediction is in excellent agreement with the experimental creep data as plotted in Figure 3.1, which shows the steel to have the initial strength but a tendency to show accelerated creep strength loss at long testing times.

3.3 Conclusions

1. Heat resistant steels with different Cr levels have been employed. Their precipitation hardening effects and solid solution strengthening effects are calculated at 650 ^{0}C. The calculated creep properties have been compared with the experimental creep strength values and the results confirms that precipitation strengthening factor can reproduce the creep strength rather well.

2. The microstructural changes due to the long-term exposure at 650 ^{0}C as a result of the Z-phase formation are analysed using thermodynamics. The analysis indicates that accelerated creep strength loss is related to the consumption of the strengthening MX carbonitrides. At a service temperature of 650°C, a high Cr level will unavoidably promote the formation of Z-phase.

3. By exploring the binary effect of two dominant alloying elements Cr and C on Z-phase formation, It was found not possible to propose compositional adjustments which lead to a combination of a high Cr level (12-15 %Cr) and a reduced tendency to form Z-phase precipitates, while meeting all other requirements for a desirable starting microstructure.

Reference

[1]   Masuyama F. Isij Int 2001;41:612.
[2]   Abe F, Kern T-U, Viswanathan R. Creep-resistant steels. Cambridge England: Woodhead Publishing, CRC Press, 2008.
[3]   Abe F. Mater Sci Eng A 2001;319:770.
[4]   Mandal A, Bandyopadhyay TK. Steel Res Int 2017;88.
[5]   Yan W, Wang W, Shan Y, Yang K. Front Mater Sci 2013;7:1.
[6]   Sklenička V, Kuchařová K, Svoboda M, Kloc L, Buršík J, Kroupa A. Mater Charact 2003;51:35.
[7]   Maruyama K, Sawada K, Koike J-i. Isij Int 2001;41:641.
[8]   Danielsen HK, Hald J. Energy Mater 2006;1:49.
[9]   Danielsen HK, Hald J. Mater Sci Eng A 2009;505:169.
[10]   Hald J. T Indian I. Metals 2016;69:183.
[11]   Strang A, Vodarek V. Mater Sci Technol-lond 1996;12:552.
[12]   Danielsen HK, Di Nunzio PE, Hald J. Metall Mater Trans A 2013;44:2445.
[13]   Lopez Barrilao J, Kuhn B, Wessel E, Talík M. Mater Sci Technol-lond 2017;33:1056.
[14]   KIMURA K, KUSHIMA H, BABA E, SHIMIZU T, ASAI Y, ABE F, YAGI K. Tetsu-to-Hagané 2000;86:542.
[15]   Kimura K, Seki K, Toda Y, Abe F. Isij Int 2001;41:S121.
[16]   Quadakkers W, Zurek J. Shreir's Corrosion 2010;1:407.
[17]   Kern T-U, Merckling G, Yagi K. Introduction. Creep Properties of Heat Resistant Steels and Superalloys. Springer, 2000. p.1.
[18]   Abe F, Tabuchi M, Tsukamoto S, Kutsumi H. Alloy Design of Creep-and Oxidation-Resistant 9Cr-Boron Steel Beyond Grades 91, 92 and 122. ASME 2014 Symposium on Elevated Temperature Application of Materials for Fossil, Nuclear, and Petrochemical Industries. Seattle, Washington, USA: American Society of Mechanical Engineers, 2014. p.44.
[19]   Igarashi M, Sawaragi Y. Development of 0.1 C-11Cr-3W-3Co-V-Nb-Ta-Nd-N ferritic steel for USC boilers. International Conference on Power Engineering-97 (ICOPE-97), Tokyo, Japan, 1997. p.107.
[20]   ASM Handbook: ASM International, 1988.

[21]   Abe F. Int J of Mater Res 2008;99:387.
[22]   Hättestrand M, Andrén H-O. Mater Sci Eng A 1999;270:33.
[23]   Danielsen HK, Hald J. Calphad 2007;31:505.
[24]   Abe F. Long-term stabilization of creep-resistant ferritic steels for highly efficient ultra-supercritical power plants. Advances in Science and Technology, vol. 72. Switzerland: Trans Tech Publ, 2010. p.12.
[25]   Lu Q, Xu W, van der Zwaag S. Philos Mag 2013;93:3391.
[26]   Lu Q, Xu W, van der Zwaag S. Acta Mater 2014;77:310.
[27]   Lu Q, Xu W, Zwaag Svd. Comp Mater Sci 2014;84:198.
[28]   Pickering FB. Physical metallurgy and the design of steels: Applied Science Publishers, 1978.
[29]   Leslie WC. Metall Mater Trans B 1972;3:5.
[30]   Lu Q, Xu W, van der Zwaag S. Comp Mater Sci 2014;84:198.
[31]   Lee K-H, Suh J-Y, Hong S-M, Huh J-Y, Jung W-S. Mater Charact 2015;106:266.
[32]   Cipolla L, Danielsen HK, Venditti D, Di Nunzio PE, Hald J, Somers MAJ. Acta Mater 2010;58:669.
[33]   Xu W, Del Castillo PRD, van der Zwaag S. Int J Mod Phys B 2009;23:1060.

Design of ferritic heat resistant steels with self-healing properties at 550$^{\text{o}}$C and above

Heat resistant steels are widely used in power plant applications, and with plant efficiency targets rising such steels have to withstand higher loads and higher temperatures for longer times. Unlike the conventional "damage prevention" alloy-design strategies, the novel Self-Healing concept opens a new window for alloy development. In this work, a generic alloy-by-design model is applied to develop novel creep resistant steels with self-healing properties. Decent mechanical properties of newly-designed alloys are to be obtained by combining precipitation strengthening ($M_{23}C_6$ carbides) and solid solution strengthening. Coupled thermodynamic and kinetic principles are employed to simulate and optimize their high temperature long-term strength values. Based on recent research of successful healing process in Fe-W model alloys, the W-containing Laves phase is selected as the self-healing agent to automatically fill the grain boundary cavities at the intended service temperature of 550$^{\text{o}}$C, so as to prolong the creep lifetime. For efficient healing to take place, it is crucial that the Laves phase forms more or less at the same time as the grain boundary cavities. An empirical relationship is derived which captures the experimental incubation time for Laves phase formation in existing commercial alloys of the basis of the calculated chemical driving force for that alloy composition. Based on desirable compositions identified by the model, a series of alloys have been made for experimental validation with comparable high temperature mechanical properties but widely different Laves phase nucleation times. The temperature dependence of the compatibility between self-healing properties and creep resistance has also been explored.

4.1 Introduction

Heat resistant steels combining superior creep strength and great corrosion resistance at high temperature are widely used in automotive, aerospace, fossil and nuclear power plants applications[1, 2]. Ferritic heat resistant steels have the advantages over austenitic steels and Ni superalloys due to their good thermal conductivity and low thermal expansion[3, 4]. However, the relatively low strength of ferritic grades and the microstructure instability due to the high Cr alloying (Z Phase formation for example) at elevated service temperature largely limits their application[4-6]. As shown in figure 4.1, Ferritic steel grades appear to reach their limit at live steam temperatures around 620°C. Attempts have been made to develop novel advanced ferritic steels with improved high-temperature properties.
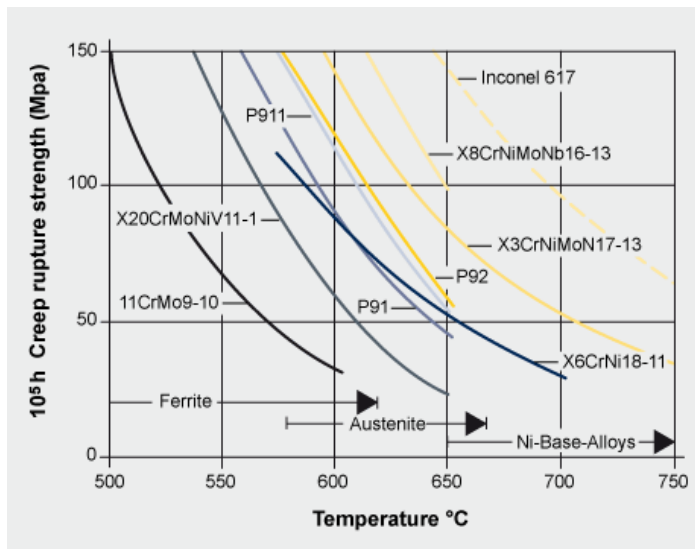
Figure 4.1 Materials for main steam pipes in power plants[7].

Conventional alloy-design strategies are following the so-called "damage prevention" paradigm[8], i.e. their composition and microstructures are tuned in such way that the formation of mechanical

damage is postponed as long as possible. In the case of ferritic heat resistant steels, commercial alloys are generally developed by employing high effective strengthening mechanisms, including precipitation strengthening by finely-distributed particles and solid solution strengthening by solvent atoms. For example, Nabiran[9] and Sim[10] studied the strengthening effect of MX carbonitrides in ferritic steels and concludes that MX carbonitrides (M=Nb,V) are highly effective in providing high temperature strength, while relatively high annealing temperatures($>1250^{o}$C) are necessary to dissolve the strengthening phases. Song[11] developed a novel ferritic alloy strengthened by coherent hierarchical NiAl/Ni$_2$TiAl particles which exhibits superior creep resistance. The coherency of hierarchical strengthening particles and the matrix provides the increment in creep strength which is strongly dependent on the Ti alloying level. However, for precipitation strengthened alloys, a drop in the strengthening contribution of precipitates is inevitable over very long service time due to the coarsening of precipitates during service. Compared to precipitation strengthening, solid solution strengthening is more stable once the equilibrium state is achieved. Alloys based on a high solid solution strengthening contribution will probably have a combination of a (lower initial) high creep strength but a highly superior stability over very long use times. Nabiran's research proves the great effect of solid solution elements W, Mo and Al on the high temperature strength after long time annealing[12].

Unlike the traditional design strategies, currently the novel concept of Self-Healing mechanism has been applied as a new promising approach to enhance the lifetime for a wide range of materials[13-15]. Namely for Self-healing materials, the occurrence of mechanical damages can be intrinsically or extrinsically repaired by the local directional mobility of the healing agents in the matrix. In the case of heat resistant steels, more focus has been paid to open the new window of designing novel alloys with enhanced creep lifetime by employing self-healing mechanism. The selection of alloying elements which can provide potential self-healing

properties has been discussed in detail by van Dijk and van der Zwaag[16]. The key parameters for autonomous healing process in iron system have been summarized as follows: a supersaturated system is necessary to provide driving force for healing precipitation; a larger atomic radius for solute atoms than that of Fe is needed to achieve a net volumetric filling process; the preference of precipitation should be at damage site rather than in the matrix; the diffusion of healing atoms should be faster than the self-diffusion of Fe; and the solute atom should not interact with other atoms to become immobile before precipitation at the desirable sites. In this case that all abovementioned requirements are fulfilled, the occurrence of local mechanical damage can cause atoms to move towards the defect site and fill it, such that it is no longer present or cannot grow further under prevailing conditions.

Following the abovementioned requirements, four iron-based binary systems with potential self-healing properties have been selected and investigated, i.e., Fe-Cu, Fe-W, Fe-Mo and Fe-Au system. Systematic researches have been made to investigate their autonomous healing process qualitatively and quantitatively. Results show that in Cu-alloyed steels, the nucleation of Cu-rich particles shows a stronger preference to present at the dislocation network within the matrix also at grain boundaries[17]. The depletion of healing source by forming at the "undesirable sites" instead of creep defects will lead to a poor healing efficiency of Fe-Cu system. Comparably in Fe-Au alloys, experimental results indicate that Au atoms highly prefer to form Au-rich BCC particles and segregate at cavity surface, with seldom appearance in the matrix. Also, first-principle calculation confirms that Au atoms diffuse two orders of magnitude faster than bcc iron self-diffusion[18]. Therefore, the effectively site-selective Au atoms with high mobility brings into a high efficiency for cavity-filling process in Fe-Au system[19-22]. However, the practical application of gold as alloying element was limited due to its scarcity. For the alloys with Mo and W addition, the precipitation of Laves phases acting as healing agent were also observed relatively good tendency to segregate at free surface of

creep damage rather than in the matrix[23]. Nevertheless, the efficiency of cavity filling as well as the precipitation kinetics of Laves phase are highly sensitive to the W and Mo addition, so the concentration of Laves phase forming elements should be cautiously considered.

In the formal research, our group has developed a genetic based computational alloy design approach coupling thermodynamics and kinetics principles, which has been successfully applied to design a serial of novel creep resistant steels with the combination of excellent mechanical properties and good corrosion resistance[24-28]. Inspired by the work on understanding the self-healing behaviour in iron-based binary alloys, the design of novel ferritic creep resistant steels with self-healing properties becomes achievable. In this paper, W containing Laves phases are selected as self-healing agents. A hybrid approach has been developed by combining the Genetic algorithm selection and conventional design approach, based on which a serious of alloys have been computationally designed with their properties characterized by experiments. Focuses are paid on quantifying the precipitation behaviour of Laves phase in newly designed alloys to realize self-healing creep resistant steels as an industrial reality.

4.2 Model description: alloy by design

The design methodology follows the "goal-means" design philosophy and has been well established in the formal work from our research group. First, a set of required properties for creep resistant steels are determined according to the application, then the required property combination was translated into microstructure feathers. The tailored microstructural feathers are converted to quantifiable criteria afterwards, and finally is linked to a specific composition and associated heat treatment conditions.

In terms of optimization strategy, Genetic Algorithms are recognised as a powerful tool for multi-parameter and multi-objective optimization, which are inspired by evolutionary process in nature system by following the survival of the fittest principle. However, the underlying physical mechanistic conclusions are hidden when calculated solutions approach the optimal results. In contrast, the conventional alloy-design method is generally started by educated guess, while the adjustments in composition are traceable to exploring the effect of alloying elements on properties. the obvious drawback is that the numerous variables can lead to low efficiency for searching while no clue to the optimum can be found during this process. In this paper, the combination of these two approaches was made to build a so-called hybrid model, in which the high efficiency in searching the composition range was integrated with the manual-selected compositional variation for unravelling the physical mechanism of alloying elements.

4.2.1 The criteria for mechanical properties

In this case, the novel creep resistant steels are expected to maintain high performance during long term use at the temperature $550^{o}C$. In principle, the steels with ferritic matrix while strengthened by both precipitation strengthening and solid solution strengthening mechanism are the microstructural requirements. A typical heat treatment of ferritic steels includes an annealing treatment for achieving composition homogeneity, followed by a rapid cooling process to keep the ferritic matrix. To obtain the desirable microstructure, it's necessary for candidate solutions at the annealing condition to fulfil the following two criteria:

1) The equilibrium volume fraction of ferrite at annealing temperature should be larger than 99%
2) The maximum level of primary carbides should be limited to 0.5% in vol.%

After homogenisation, the alloy is quenched to room temperature, then a nearly fully ferritic matrix can be maintained without phase transformation. However, during service the thermodynamic equilibrium may vary and some undesirable phases may form. Therefore, additional go/no-go criteria are enforced during service at the intended temperature $550^{o}C$:

3) The maximum allowed volume fraction of all undesirable phases (all phases exclude ferrite, $M_{23}C_6$ carbide and Laves phase) should be no more than 1%

4) A minimum chromium concentration of 8 wt.% in solid solution in matrix to yield adequate corrosion and oxidation resistance

4.2.2 The criteria for self-healing properties

When discussing the possible criteria for the self-healing properties in creep resistant steels, the precipitation behaviour of healing agents needs to analysed quantitatively. In principle, the amount of healing phase should be firstly set a decent minimum level to provide the efficiency of cavity-filling, namely, the volume of healing agents should be no less than that of the defects. In Fang's work, the volume fraction of creep cavities in Fe based alloys has been measured systemically by 3D synchrotron X-ray tomography. The results show that at the service temperature $550^{o}C$ while the stress range within 60-117MPa, the amount of creep cavities varies between 0.11-0.76 vol.%[21]. Based on this experimental observation, in our design the amount of Laves phase was defined as follows:

5) The minimum volume fraction of Laves phase as healing agents should be no less than 1%

4.2.3 Design flow chart

The flow chart of design strategy as a conclusion of abovementioned criteria is shown in figure 2. The chemical composition and annealing temperature are randomly selected by the algorism, and the thermodynamic equilibriums are calculated at annealing process and in-use stage consequently. At the stage of annealing heat treatment, a nearly fully ferritic matrix is required with limited amount of primary carbides. At the service temperature, the corrosion and oxidation resistances are guaranteed by the adequate Cr concentration in matrix; the thermodynamic equilibrium phase configuration in target should be the ferritic matrix with only strengthening particle $M_{23}C_6$ carbides and healing agents Laves phase with their total volume fraction higher than 99 vol.%; the self-healing properties are quantified by the amount of Laves phase as self-healing agents. The solutions which can fulfil all the criteria will be restored as candidates, then their mechanical properties contributed by precipitation hardening and solid solution strengthening are calculated by two properly defined equations. The detailed information of these two equations will be discussed in the next section. Any solution that violates any listed criteria will stop the flow and go back to search a new solution.
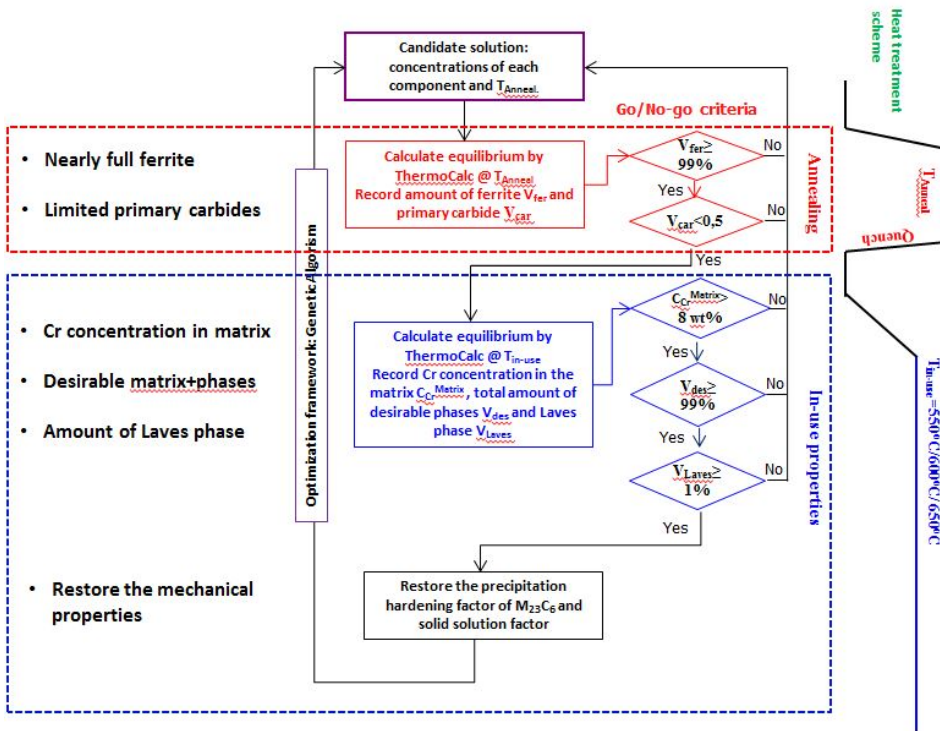
Figure 4.2 Alloy design strategy and criteria evaluation

4.2.4 The quantifiable parameters for mechanical properties

As grain boundary strengthening cannot be modelled by macroscopic approaches, the precipitation hardening and solid solution strengthening are the targeted methods to raise the creep strength. In our previous work, the precipitation strengthening contribution in creep resistant steels has been shown to be inversely proportional to the inter-particle spacing, which in general is a function of the particle volume fraction, the initial particle size and coarsening kinetics of the precipitates.[24, 27, 29] The following expression is used to calculate the time-dependent precipitate strengthening factor while taking into account precipitate coarsening and its temperature dependence:

$$\sigma_p \propto 1\big/_L = \sqrt{f_p}\big/_r = \sqrt{f_p}\Big/_{\sqrt[3]{r_0^3 + Kt}} \qquad (1)$$

$$r_{0 =} 2\gamma\big/_{\Delta G_V} \qquad (2)$$

$$K = 8\gamma V_m^p \Big/_{\sum_{i=1}^{n} \frac{9(x_i^p - x_i^{mp})^2}{x_i^{mp} D_i}\big/_{RT}} \qquad (3)$$

where L is the average inter-particle spacing, f_p is the equilibrium volume fraction of the strengthening precipitates at the service temperature, r_0 is the critical precipitate nucleus size, γ is matrix-precipitate interfacial energy, ΔG_v is volume thermodynamic driving force for the precipitation. V_m^p is the molar volume of precipitate. K is the factor of coarsening rate and t is the exposure time at the high temperature. x is equilibrium interface mole fraction of the precipitation former elements on both matrix (m) and precipitate (p) sides. T is the service temperature and D_i is the corresponding diffusion coefficient. In the calculations the interfacial energy is arbitrarily set at a fixed value of 1 J/m^2 irrespective of the precipitate size or type. This is a slight simplification but helps in illustrating the effect of precipitate coarsening. All thermodynamic parameter values including f_p, ΔG_v, x_i^p, x_i^{mp}, D_i and V_m^p required during the calculations were calculated via Thermo-Calc using the TCFE9 and MOBFE1 databases. The equation shows that the highest strengthening factors are obtained for high volume fractions and small and constant precipitate sizes, i.e. precipitates showing a very low coarsening rate. The computational details of the model and its application to MX precipitation strengthened creep resistant steel design can be found elsewhere[24, 27, 29]. In the

present calculations the temperature and the creep time are fixed at 550°C and 10^5 seconds respectively.

With respect to solid solution strengthening, the solid solution strengthening(SSS) factor was taken to be the weighted contribution of atomic concentration of solutes, which can be formulated as

$$\Delta\sigma_{ss} = \alpha_T \sum_i S_i x_i^{mp} \tag{4}$$

Where α_T is a temperature dependent scalar, and S_i is the (room temperature) solid solution strengthening coefficient which combines size misfit and modulus misfit effect. For the solid solution elements in this work, the strengthening coefficients at room temperature were determined from literature data on binary Fe-M systems and actual values are shown in table 1[30, 31]. In reference[26], the temperature dependence of parameter αT was determined by the quantitative analysis between the experimental minimum yield strength and the calculated solid solution strengthening contribution from existing ferritic steel grades. Following the same calibration study and based on the experimental results from data sheets[32], a value of α_{550}=0.98 was used in the following discussion.

Table 4.1 Strengthening coefficient for alloying elements at room temperature (MPa per at.%) [30, 31].

Element	C	Si	Mn	Mo	W	Cr
Si	1103.45	25.80	16.90	15.90	31.8	2.60

4.2.5 Selection of alloying elements and search domain

It is an unprecedented research to design of novel heat resistant steels with self-healing properties for industrial application, so a relatively simple alloying system was selected in this work, with C, Cr, Mn, Si and W as alloying elements. The composition ranges and heat treatment parameters applied in the design exercise are listed in table 2. W is the key forming elements for healing agent Laves phase, while C and Cr forms the main strengthening particle $M_{23}C_6$. Cr also provides the necessary corrosion and oxidation resistance during high temperature application. Mn and Si are the most commonly used alloying elements in steels and here are employed to provide decent solid solution strengthening contribution. The determine of composition range takes into account practical constrains based on existing heat resistant steel grades.

Table 4.2 Search range (in wt.%) for alloying elements and the annealing temperature.

	C	*Cr*	*Mn*	*Si*	*W*	*Fe*	$T_{anneal}/^oC$
Min.	0	12	0	0	0		800
						Bal.	
Max.	0.1	20	5	5	3		1200

4.3 The design results
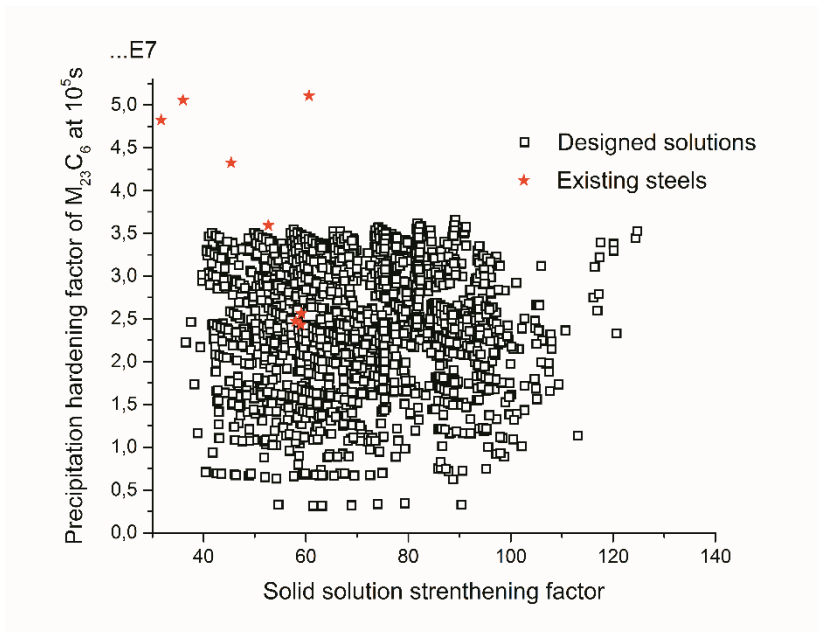
Figure 4.3 PH factor of $M_{23}C_6$ carbides at 10^5s versus SSS factor of solutions meeting all go/no-go criteria. The values of existing alloys, as indicated by star symbols, are also put on the plot to compare to the designed solution.

Based on the design flow chart in figure 4.2, the GA based search covered about 10^6 unacceptable or less well performing variants and finally restored around 10^4 desirable solutions. All candidate solutions which fulfil all the go/no-go constrains are recorded for further analysis, with the Precipitation Hardening factors of $M_{23}C_6$ carbides at the time of 10^5 s versus Solid Solution Strengthening factors shown in figure 4.3. The solutions with the combination of high PH and SSS values are expected to possess the best mechanical properties, locating in the right top corner of the figure. To benchmark the designed solutions, existing

alloys have been selected with their chemical composition shown in table 3. Their PH factors as well as the SSS factors are indicated by stars. Compared to the exiting alloys marked by red dots, the designed solutions are relatively weak in precipitation strengthening contribution; the best performed solutions can reach 2/3 value of PH factor of commercial grade 12CrMoWV. However, given the fact that the alloying system of our work is only a five-element system compared to commercial alloys which have up to 11 alloying elements, the difference in precipitation strengthening is fairly acceptable. Besides, it's worth noting that in terms of SSS factor, wide range of the solutions can reach the values that are beyond the performance of existing alloys. The simulation in mechanical properties shows that at the service temperature 550°C, the designed solutions can reach the comparable level in strength compared with the existing steels.

Table 4.3 Chemical composition and heat treatment parameter of existing $M_{23}C_6$ and Laves phase containing steel grades (in wt.%)[33-36].

	C	*Si*	*Mn*	*Cr*	*Ni*	*Mo*	*W*	*V*	*N*	*B*	*Al*	*others*
F-82H	0,1	0,1	0,48	7,65	0,01	-	2	0,18	0,002	0,0034	0,01	0,038Ta
F-82	0,1	0,17	0,48	7,52	0,05	-	2,2	0,2	0,002	0,0035	0,01	-
HT9	0,19	0,22	0,48	12	0,6	1	0,5	0,29	0,002	-	0,02	-
T-91	0,11	0,45	0,43	8,57	0,1	1	-	0,22	0,03	-	0,03	0,08Nb
9Cr4W	0,1	0,3	0,5	9	-	-	4	-	0,002	-	-	-
12CrMoVW	0,22	0,29	0,76	11,38	0,55	0,96	1	0,25	-	-	-	-
CR	0,05	0,067	0,58	9,85	0,94	2,31	-	0,12	-	-	-	0,06Nb
CA4	0,038	0,066	1,17	9,36	0,84	2,04	-	0,096	-	-	-	0,01Nb
CA3	0,049	0,29	1,24	9,21	0,84	2,29	-	0,1	-	-	-	0,01Nb

4.3.1 The simulation of precipitation behaviour of Laves phase
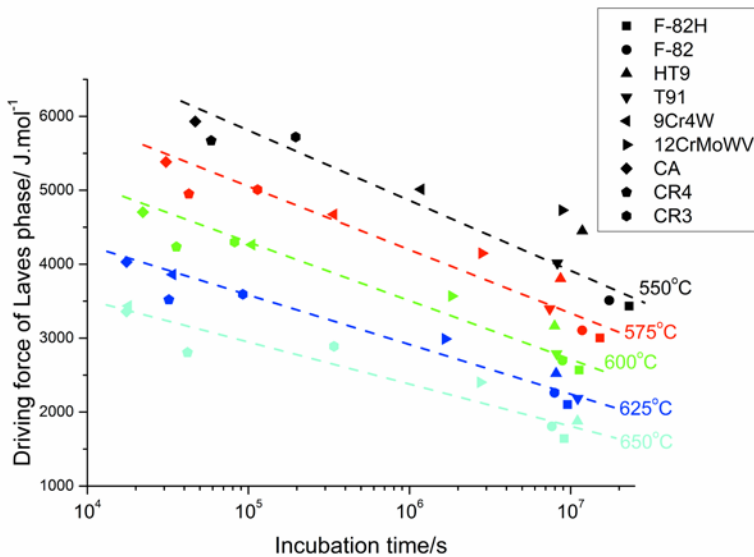
Figure 4.4 The incubation time of Laves phase extracted from experimental observation as a function of calculated driving force for Laves phase in existing commercial steels[33-36].

By now the microstructural parameters which are directly related to the mechanical properties have been defined and discussed. However, one key parameter is still necessary in the design strategy, which should be able to quantify the self-healing efficiency of healing agents as an optimization parameter during computational simulation. For a healing process with high efficiency, Laves phases are expected to only be able to precipitate at creep cavities without any formation in the matrix. From the perspective of forming energy, the nucleation of self-healing agents at the cavity free surface will lower the energy barrier compared to that in the bulk. Ideally, the formation driving force of Laves phase should be located precisely between the nucleation energy range with and without the effect of free surface. In comparison with the homogeneous

nucleation in the bulk, the decrease in energy barrier of heterogeneous nucleation at the free surface is mainly due to the reduction in interfacial energy, misfit energy and volume energy of the newly formed phase. To quantify the energy reduction, complex parameters like the interface relationship among matrix/self-healing agents/cavity, the lattice and modulus misfit between matrix and self-healing agents, the growth kinetics of healing agents, need to be taken into consideration.

To simplify the problem by circumventing the complex energy factors, the value of Lave phase driving force was employed as a decision parameter, which can be easily obtained from computational calculation based on the chemical composition of the alloys. However, this simplification requires a direct connection between the calculated Laves driving force and the experimental formation behaviour of Laves phase for quantitative analysis. For the selection of experimental parameter which can present the behaviour of Laves phase, the incubation time of Laves phase is employed in this research. According to the classical nucleation theory, the homogeneous nucleation with a spherical nucleus can lead to an equation between nucleation incubation time and chemical driving force, where $t_{incubation}$ is proportional to the negative square of chemical driving force [37-39]. However, In reality much more complex factors need to be considered compared to the homogeneous nucleation assumption, so explorations have been made to build the empirical relationships between calculated driving force and experimental incubation time in the following discussion.

The experimental incubation time of Laves phase are extracted based on the temperature-time-precipitation curves in existing steels in table 4.2, while the driving force of Laves phase in these steels are calculated according to their chemical compositions. Then incubation time of Laves phase from experiments versus the calculated Lave phase driving force was drawn and shown in figure 4.4. It can be clearly found that for all existing steels, a perfect linear relationship can be found between the incubation time and formation driving force of Laves phase at all temperature ranges, as shown by the dash lines with different colours.

As the temperature increases, the slopes of the fitting lines decrease slightly, which reflects the temperature dependence of diffusion on the Laves phase formation. The remarkable linear connection between these two parameters enables us to predict the precipitation kinetics of Laves phase through calculated information based on the formation driving force of Laves phase.

4.3.2 The modified design results

After defining the driving force of Laves phase as the quantifying parameter for self-healing behaviour, the properties of acceptable solutions in figure 4.3 are redrawn and shown in figure 4.5. In figure 4.5a, precipitation hardening factor was set the key optimization parameter as the mechanical property contribution. The dots with different colours indicate the different range of SSS values. It can be found that black dots and blue dots can distribute evenly in the whole PH/DF range while the green dots with highest level of SSS values tend to crowd in the high driving force value domain. The ideal solution with the combination with high value of PH factor and SSS factor as well as the low driving force of Laves phase should be the dots with green colour and located at the bottom right corner of the figure. Similar method was applied to obtain figure 4.5b, with SSS value being the main optimization parameter versus Laves driving force. In this figure, the density of the dots are obviously higher in the high driving force range, while the dots located in the relatively low driving force domain are more sparse.

The validation of PH factor and SSS factor as criteria for mechanical properties have been confirmed by our formal work, see reference[26-29]. For the newly defined parameter, driving force of Laves phase, the experimental tests are necessary to validate the applicability as a criterion to quantify the self-healing efficiency. In the following section, representative solutions are selected for further experiments with comparable calculated properties
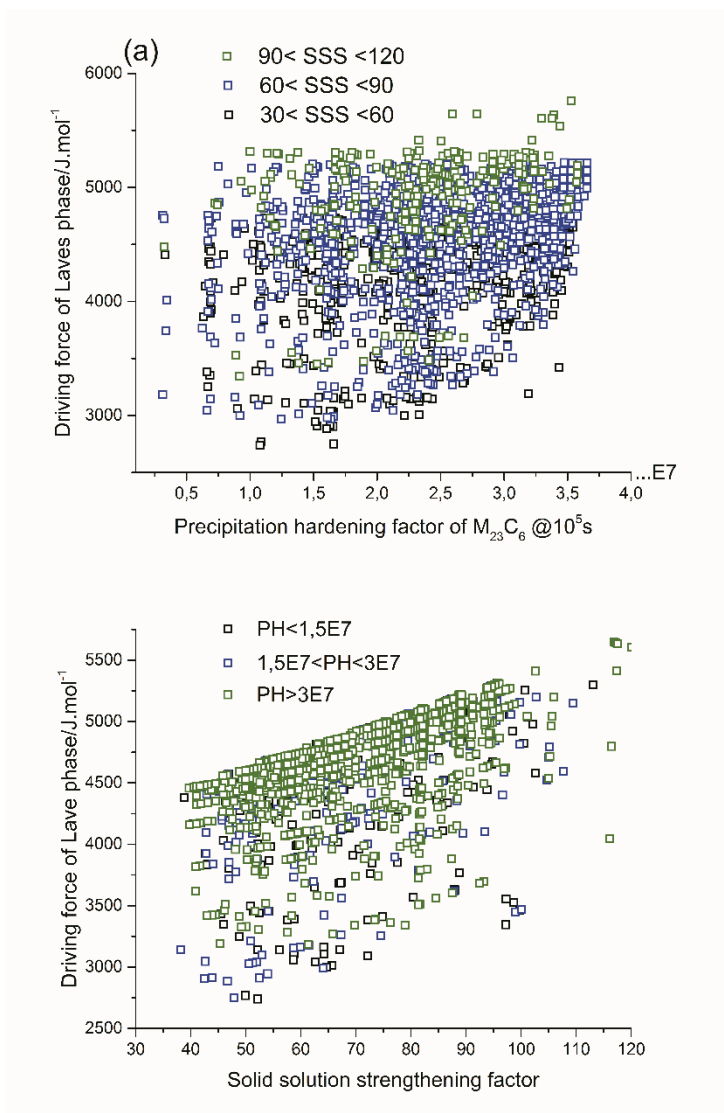
Figure 4.5 PH factors of $M_{23}C_6$ precipitates as strengthening particles at 10^5s (a) and the SSS factors (b) versus driving force of Laves phase as self-healing agents meeting all go/no-go criteria at the temperature of 550^oC.

4.3.3 The selected sample alloys
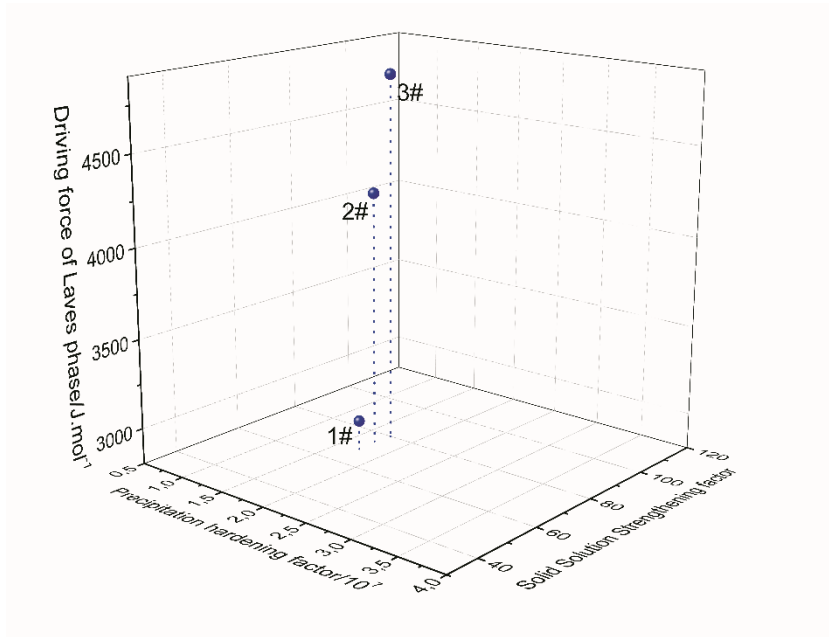
Figure 4.6 The selected alloys with comparable mechanical and self-healing properties from simulation.

Based on GA model, the solution pools have been built shown in figure 4 and 5, with all properties of the solutions being restored. Then classification of the solutions is made manually through conventional composition optimization method, while the effects of variation in chemical concentration on the targeted properties are explored. Afterwards, a series of solutions with comparable properties are selected as test samples, as shown by the dots in figure 4.6. The selected sample alloy No.1, 2, 3 has the similar level of PH factor values and SSS factor values, but with the Laves phase driving force value 2964 J/mol, 4218 J/mol and 4848 J/mol respectively. These three alloys are expected to have similar creep strength but difference in creep life time due to the variation in formation behaviour of Laves phase as healing agents. The

chemical compositions, annealing temperature and calculated properties of these alloys are shown in table 3.

The variation in chemical concentrations of all sample alloys are indicated in table 3. With the increase in Laves phase driving force from alloy 1 to 3, the concentration of Mn keeps decreasing while Si and W alloying levels increase continuously, while C and Cr concentration are almost unchanged. The experimental investigation from Hosoi[34] indicates that the addition of Si and decrease in Mn alloying will improve the formation kinetics of Laves phase, which agrees well with our prediction results. The increase in alloying level of W as the Laves forming element leads to the increase in laves driving force, which is also predictable due to the higher supersaturated level.

Table 4.3 Composition of 3 selected alloys (in wt.%), with annealing temperatures, their phase configuration, PH factor, SSS factor and Driving force of Laves phase of at 550°C.

	C	Cr	Mn	Si	W	T_{anneal}/ K	Phase configuration/%	PH@10^{5}s $M_{23}C_6$	SSS	DF of Laves/J.mol^{-1}
1	0,026	12	0,81	0,32	1,45	1473	BCC+1,03Laves+0,52M$_{23}$C$_6$	1,73E+07	69	2964,2
2	0,023	12	0,32	0,65	2,23	1473	BCC+1,87Laves+0,46M$_{23}$C$_6$	1,71E+07	75	4218,4
3	0,023	13,03	0,01	0,97	3,0	1473	BCC+2,6Laves+0,72M$_{23}$C$_6$	1,74E+07	80	4848,8

Table 4.4 Composition of 2 alloys (in wt.%) with further alloying, the annealing temperatures, phase configuration, PH factor, SSS factor and Driving force of Laves phase of at 550°C

	C	Cr	Mn	Si	W	others	T_{anneal}/K	Phase configuration/%	PH@10^{5}s $M_{23}C_6$	PH@10^{5}s NbX	SSS	DF of Laves/ J.mol^{-1}
4	0,023	12	0,32	0,65	**2,23**	**0.1Nb**	1473	BCC+1,90Laves +0,23 M$_{23}$C$_6$ +**0,1 NbC**	1,22E+07	7.04E+07	75	4253
5	0,023	12	0,32	0,65	**2,23**	**0.004B**	1473	BCC+1,86Laves +**0,45**M$_{23}$C$_6$ +**0,06 M$_2$B**	2.76E+07	-	72	4198
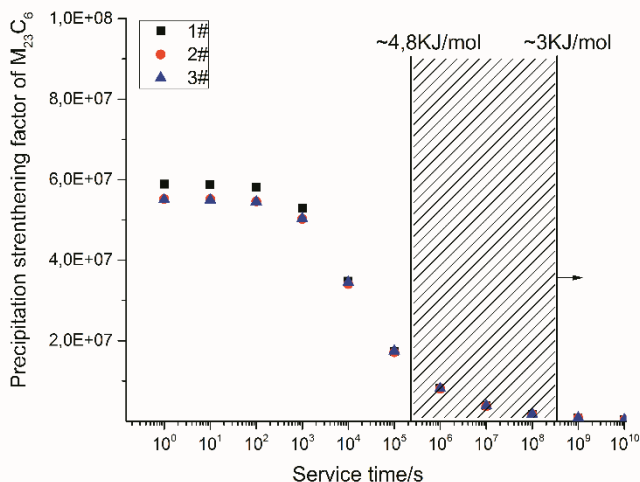
Figure 4.7 The degradation behaviour of PH factor for $M_{23}C_6$ precipitates with service time for 3 selected alloys.

It's interesting to explore the performance of the strengthening particle, $M_{23}C_6$ carbides, at the time domain when the Laves phase starts to form as self-healing agents. In figure 4.7, the PH factor evolution with time for the sample alloys No. 1-3 are shown. The results demonstrate that minor difference in the value of PH factor of $M_{23}C_6$ for all alloys can be found. Besides, the PH contributes from $M_{23}C_6$ can keep stable within the starting few hundreds of seconds. Pronounced degradation occurs during the time range 10^3-10^5 seconds and at 10^5s the PH value decrease to one fifth of the initial strength. The vertical lines in figure 4.7 marked the area with slash patterns, which was the expected formation time domain for Laves phase based on the calculated driving force of Laves phase, according to the relationship from figure 4.4. At this time domain when Laves phase starts to form, the strength contributed by $M_{23}C_6$

precipitates is reduced to a relatively low level which is around one tenth of the original strength.

4.3.4 The modified sample alloys

Given the fact that the performance of $M_{23}C_6$ carbides in sample alloys will experience significant degradation before the formation of Laves phases, attempts are made to explore the possibility to stabilize $M_{23}C_6$ precipitates after long time service, as well as employing a more effective precipitate which can be more coarsening resistant. Sample alloy No.2 has been selected as the baseline composition for further adjustment.

Among the strengthening precipitations family in heat resistant steels, MX carbonitrides have been proved high effective in providing superior creep strength due to their nano-sized initial dimension and excellent resistance to coarsening[1, 40]. The application of MX particles in strengthening ferritic steels was largely limited due to the low solubility of ferrite for MX forming elements like Nb, V and Ti. The corresponding problems brought by employing MX in ferritic matrix are the relatively high annealing temperature to dissolve the carbonitrides, otherwise MX would form as large-size primary precipitates and become detrimental. Here 0.1% Nb was added in alloy No.2 to form NbC carbides as new strengthening particles. The new alloy with Nb addition is numbered 4 with its detailed properties shown in table 4.

Also, Boron addition in heat resistant steels has been widely applied as strategy for novel alloy development, and the alloying of small amounts Boron can effectively improve the long-term creep properties for commercial steel grades[41, 42]. Experimental results have shown that Boron alloying mostly ends up in $M_{23}C_6$ carbides instead of dissolving in the matrix[43, 44], while more detailed investigation has shown that Boron partition in $M_{23}C_6$ precipitates can efficiently supress the particle coarsening also helps to maintain of a homogeneous distribution of

$M_{23}C_6$ carbides near prior austenite grain boundaries. Therefore, 0.004% B was added in alloy No.2 with all the properties listed in table 4.
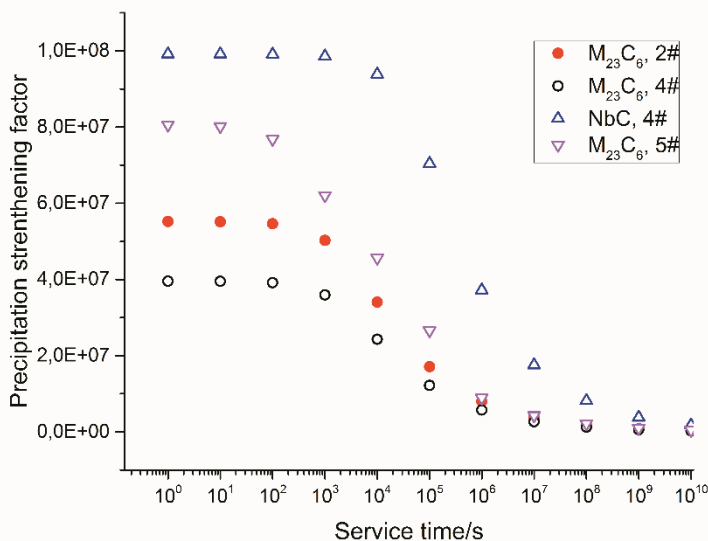
Figure 4.8 The degradation behaviour of PH factor for $M_{23}C_6$ and NbC precipitates with service time for alloys No. 4 and 5.

After the Nb and B addition, the coarsening behaviours of strengthening particles in new alloys with the comparison of No.2 alloy are shown in figure 4.8. Alloy No.2 was set as reference alloy with the PH factor marked as red solid dots, while the hollow dots marked the properties of new alloys. For alloy No.4 with Nb addition, the contributes made by NbC carbides possess a doubled value of initial PH factor compared to that of alloy 2, with more sluggish coarsening rates as shown by the blue dots. Also, the amount of $M_{23}C_6$ carbides in alloy 4 is reduced due to the depletion of carbon, as shown by the black dots. After Boron alloying in alloy 5, the PH factor of $M_{23}C_6$ has a remarkable increase, but no great improvement can be found in the change of coarsening behaviour of

particles, since the increment in strength is largely due to the increase in the volume of $M_{23}C_6$.

4.3.5 The alloy design for higher temperature application

By now the discussion is based on the application with the in-use temperature fixed at 550°C, while the precipitation strengthening was emphasized as the key parameter for providing the mechanical properties in the alloy design strategy. In the current industrial application, during the last fifty years the service temperature in fossil-fired power plants have been continuously raised to improve thermal efficiency. Efforts for raising steam conditions are in response to the social demand for environmental protection as well as energy conservation concerns. Therefore, in the following content, we attempt to broaden the application window to higher temperature domain in our design strategy, by setting the in-use temperature at 600°C and 650°C. The temperature dependence of the mechanical properties and self-healing properties are explored then discussed computationally.

Following the same alloy-by-design concept discussed in last section, similar results have been obtained presenting the combination of mechanical properties and self-healing properties at 600°C and 650°C, as shown in figure 4.9a and 4.9b respectively. At the in-use temperature pre-setting at 600°C in figure 9(a), the minimum value of driving force of Laves phase was 2170 J/mol, located in the bottom left corner of the image. To develop the series of alloys with comparable properties at different temperature level, figure 4.9a was compared with figure 4.3. It can be obviously shown that the range of x axis, i.e., the value of precipitation hardening factor at 600°C was halved compared to that at 550°C. Besides, for alloys No.1, 2, 3 and 5 with the PH factor higher than 1.7E7 designed at temperature 550°C, the values of whose PH factor are beyond the highest range of that in figure 4.9a. The degradation of particle strengthening contribution as temperature

increases is predictably due to the faster coarsening rates of precipitates brought by the higher atomic mobility at higher temperature.

When it comes to solid solution contribution, the temperature dependence parameter α_{600} was obtained by the same abovementioned method[26] with the value 0.64 at 600°C. Comparing with the SSS value in figure 4.5, the solid solution contribution in figure 4.9a can reach a higher-level range to 150. According to the colour distribution of the dots, solutions with higher SSS values tend to disperse in the higher driving force range.

In figure 4.9b, the lowest value of driving force of Laves phase was 1500 J/mol. Compared with figure 3, the value range of x axis at 650°C is one magnitude less than that at 550°C. For the same alloying system, the shrinkage in PH factor at elevated temperature is fairly too high to provide decent strength. However, the solid solution contributes at 650°C can reach as high as 180, as shown by the pink dots. From the comparison between figure 4.5 and figure 4.9a, b, the general trend of strength as increased temperature is that, great decrease in PH factor can be obtained due to the increased coarsening rate of particles, but the SSS factor can reach a higher value from the improved solubility at higher temperature. Thus, it would be of high interest to explore the compatibility of low Laves driving force and high solid solution strengthening as the effect of temperature variation. In the following discussion, the solid solution strengthening factor was set as the key optimization parameter at 600°C and 650°C to reconstruct the "Pareto front" between the SSS contributions and self-healing properties for high temperature application.
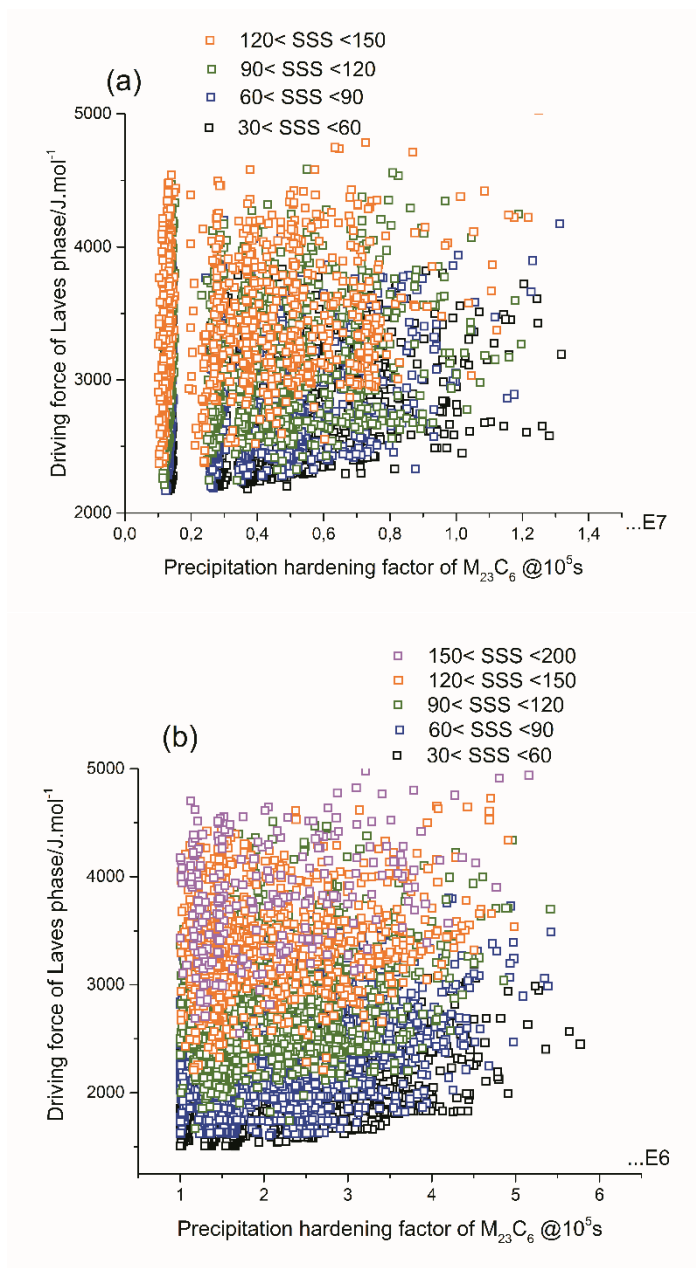
Figure 4.9 PH factors of $M_{23}C_6$ precipitates as strengthening particles at 10^5s versus driving force of Laves phase as self-healing agents meeting all go/no-go criteria at the temperature of 600°C(a) and 650°C(b).

4.3.6 The design results: SSS factor as key optimization parameter at higher temperature
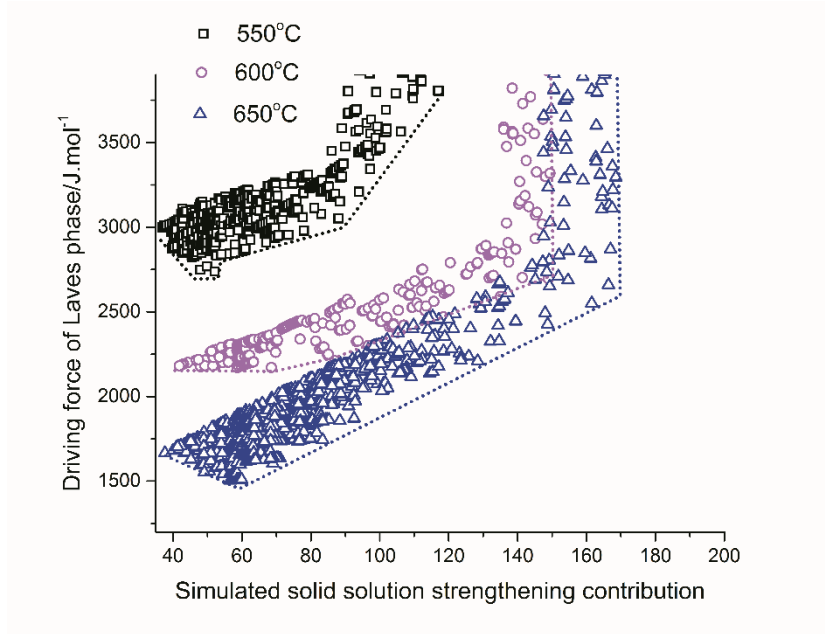
Figure 4.10 Properties values for SSS factor and Laves phase driving force on the Pareto front at different temperature domain.

As shown in figure 4.10, a large number of solutions of different combinations of SSS and Laves driving force at different temperatures are marked by different colour dots. As the temperature increases, it was more direct-viewing that solutions extend to the domain with elevated SSS factor and reduced Driving force value. The optimal solution with low Lave driving force and high SSS contribution located on the right bottom corner of the figures, therefore the fitting lines of the dots' distribution at the bottom and right edges need to be investigated. It's noteworthy that with the increase of temperature, the slopes of the bottom fitting curve become steeper, which means at higher temperature, more sacrifice is needed in Laves driving force if higher SSS value

wants to be obtained. Namely, the compatibility of low Lave driving force and high solid solution strengthening effects become more difficult to be combined with increased temperature.

To summary, the strengthening mechanism at 600^oC and 650^oC are both proved difficult to have a decent performance in the current alloying system. The precipitation hardening suffers from the rapid coarsening behaviour of $M_{23}C_6$ carbides, while the high solid solution strength only can be achieved at the expense of sacrifice the self-healing properties.

4.4 Conclusion

1. A generic alloy-by-design model is applied to develop novel creep resistant steels with self-healing properties. Decent mechanical properties of newly designed alloys are to be obtained by combining precipitation strengthening and solid solution strengthening, which are comparable to existing heat resistant commercial grades.
2. To quantify the self-healing properties, an empirical relationship is derived which captures the experimental incubation time for Laves phase formation in existing commercial alloys of the basis of the calculated chemical driving force for that alloy composition. The compatibility of self-healing properties and mechanical properties were evaluated then for industrial feasibility.
3. A serious of novel alloys with gradients in self-healing properties but similar mechanical properties have been developed for experimental validation. Free surface precipitation tests and tensile creep tests are to be executed to measure the filling efficiency of creep cavities for the alloys.

4. At the temperature range higher than 550°C, the compatibility of self-healing properties and creep resistance degrades both the precipitation hardening and solid solution strengthening.

Reference

[1]   Abe F, Kern T-U, Viswanathan R. Creep-resistant steels. Cambridge England: Woodhead Publishing, CRC Press, 2008.
[2]   Allen N. Nature 1951;167:836.
[3]   Ennis P, Czyrska-Filemonowicz A. Sadhana 2003;28:709.
[4]   Masuyama F. Isij Int 2001;41:612.
[5]   Danielsen HK, Hald J. Energy Mater 2006;1:49.
[6]   Danielsen HK. Mater Sci Technol-lond 2016;32:126.
[7]   International Molybdenum association. https://www.imoa.info/molybdenum-uses/molybdenum-grade-alloy-steels-irons/high-temperature-steel.php.
[8]   van der Zwaag S. Self healing materials: an alternative approach to 20 centuries of materials science: Springer Science+ Business Media BV Dordrecht, The Netherlands, 2008.
[9]   Nabiran N, Weber S, Theisen W. High Temp Mater Pr-isr 2013;32.
[10]   Sim GM, Ahn JC, Hong SC, Lee KJ, Lee KS. Mater Sci Eng A 2005;396:159.
[11]   Song G, Sun Z, Li L, Xu X, Rawlings M, Liebscher CH, Clausen B, Poplawsky J, Leonard DN, Huang S, Teng Z, Liu CT, Asta MD, Gao Y, Dunand DC, Ghosh G, Chen M, Fine ME, Liaw PK. Sci. Rep. 2015;5:16327.
[12]   Nabiran N, Weber S, Theisen W. Procedia Engineering 2011;10:1651.
[13]   De Belie N, Gruyaert E, Al-Tabbaa A, Antonaci P, Baera C, Bajare D, Darquennes A, Davies R, Ferrara L, Jefferson T. Adv Mater Interfaces 2018:1800074.
[14]   Yang Y, Urban MW. Adv Mater Interfaces 2018:1800384.
[15]   Zhong N, Post W. Compos Part A Appl Sci Manuf 2015;69:226.

[16]   van Dijk N, van der Zwaag S. Adv Mater Interfaces 2018:1800226.

[17]   Zhang S, Schut H, Kohlbrecher J, Langelaan G, Brück E, Van der Zwaag S, van Dijk N. Philos Mag 2013;93:4182.

[18]   Versteylen C, van Dijk N, Sluiter M. Phys Rev B 2017;96:094105.

[19]   Zhang S, Kohlbrecher J, Tichelaar FD, Langelaan G, Brück E, van der Zwaag S, van Dijk NH. Acta Mater 2013;61:7009.

[20]   Zhang S, Langelaan G, Brouwer JC, Sloof WG, Brück E, van der Zwaag S, van Dijk NH. J Alloy Compd 2014;584:425.

[21]   Fang H, Versteylen CD, Zhang S, Yang Y, Cloetens P, Ngan-Tillard D, Brück E, van der Zwaag S, van Dijk NH. Acta Mater 2016;121:352.

[22]   Zhang S, Kwakernaak C, Sloof W, Brück E, van der Zwaag S, van Dijk N. Adv Eng Mater 2015;17:598.

[23]   Zhang S, Fang H, Gramsma ME, Kwakernaak C, Sloof WG, Tichelaar FD, Kuzmina M, Herbig M, Raabe D, Brück E, van der Zwaag S, van Dijk NH. Metall Mater Trans A 2016;47:4831.

[24]   Lu Q, Xu W, van der Zwaag S. Philos Mag 2013;93:3391.

[25]   Lu Q, Xu W, van der Zwaag S. Metall Mater Trans A 2014;45:6067.

[26]   Lu Q, Xu W, van der Zwaag S. Comp Mater Sci 2014;84:198.

[27]   Lu Q, Xu W, van der Zwaag S. Acta Mater 2014;77:310.

[28]   Lu Q, Xu W, van der Zwaag S. Acta Mater 2014;64:133.

[29]   Lu Q, Xu W, Zwaag Svd. Comp Mater Sci 2014;84:198.

[30]   Pickering FB. Physical metallurgy and the design of steels: Applied Science Publishers, 1978.

[31]   Leslie WC. Metall Mater Trans B 1972;3:5.

[32]   Alloy Digest: Data on World Wide Metals and Alloys: ASM International, 2011.

[33]   中橋昌子, 小松周一, 中村新一, 山田政之. 日本金属学会誌 1983;47:426.

[34]   Hosoi Y, Wade N, Kunimitsu S, Urita T. J Nucl Mater 1986;141:461.

[35]   Tamura M, Hayakawa H, Tanimura M, Hishinuma A, Kondo T. J Nucl Mater 1986;141-143:1067.

[36]   Abe F, Araki H, Noda T. Metall Trans A 1991;22:2225.

[37]   Russell KC. Adv Colloid Interface 1980;13:205.

[38]   LeGoues F, Aaronson H. Acta Metall. 1984;32:1855.

[39]   Kampmann R, Wagner R. Materials science and technology. VCH, vol. 5. Germany, 1991.

[40]   Kong H, Liu C. Technologies 2018;6:36.

[41]   Strang A, Gooch D. Microstructural development and stability in high chromium ferritic power plant steels. Conference on microstructural development and stability in high chromium ferritic power plant steels. Cambridge, UK, 1997. p.11.

[42]   Hald J, Straub S. Mater Adv Power Eng 1998:155.

[43]   Hättestrand M, Andrén H-O. Mater Sci Eng A 1999;270:33.

[44]   Lundin L. High Resolution Microanalysis of Creep Resistant 9-12% Chromium Steels. Doctoral dissertation. Denmark: Chalmers University of Technology, 1995.

Microstructure and dislocation structure evolution during creep life of Ni-based single crystal superalloys

The high performance of Ni single crystal superalloys during high temperature low stress creep service, is intrinsically determined by the combined effects of microstructural evolution and the dislocation behaviour. In the field of the evolution of dislocation network, two main recovery mechanism based on dislocation migration dominate the process. One is superdislocations shearing into γ' rafts through a two-superpartials-assisted approach. Another is the compact dislocations migrating along γ/γ' interface. These two mechanisms are similarly climb-rate-controlled process. In this work, a model for the minimum creep rate based on thermodynamic and kinetic calculations and using an existing detailed dislocation dynamics model has been built by taking the dislocation migration behaviours as well as the rafted microstructure into consideration, which can well reproduce the ([100] tensile) creep properties of existing Ni superalloy grades, without the need to make the dislocation parameter values composition dependent.

5.1 Introduction

Ni-based single crystal superalloys have been widely used for the blades and other loaded structures of aero-engines and gas turbines due to their superior mechanical properties, in particular their excellent creep resistance at high temperatures[1]. Their outstanding creep resistance, not only origins from the absence of grain boundaries but is largely determined by the unique microstructure characterised by the presence of a high-volume fraction of the long-range ordered $L1_2$ γ' phase, which appears as cubes coherently embedded in a face-centered cubic solid solution γ matrix. In general, the size, volume fraction and morphology of γ' precipitates mainly determine the mechanical properties of Ni-superalloys[2, 3]. In the as-produced condition the cuboidal γ'-precipitates have a size of around 0.4um size and they are separated by γ-channels with around 0.1um size. The typical precipitate volume fraction at room temperature is 50% or higher[1].

When exposed to their typical use conditions, a relatively high temperature (>950C) and a modest stress (<250MPa), there is directional coarsening of γ' precipitates during the early creep stage, which is so-called "rafting" stage[4-7]. During this time, the initially adjacent cuboidal γ' particles coalesce and form platelets that turn into plate-like or rod-like structures. This lamellar γ/γ' rafted microstructure will remain more or less unchanged during the long stable creep stage, until the γ' gradually interconnects and becomes the matrix phase surrounding isolated γ phase islands[8, 9]. This process is known as the 'topological phase inversion', which has been considered as the microstructural indicator marking the transition from quasi-stationary creep to accelerated creep. This inverted microstructure is maintained during the accelerated creep stage but rapidly loses it regularity, the morphology evolution of the phases during the entire creep life is presented in figure 1[10].
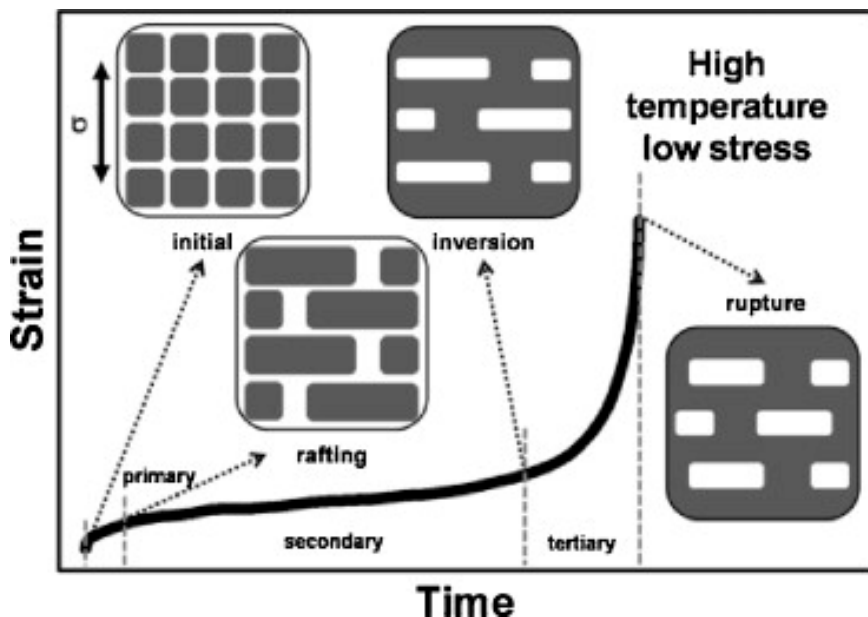
Figure 1. Schematic illustration of the microstructure evolution of Ni superalloy single crystals during high temperature low stress creep loading. The black phase is the γ′ phase, while the white phase marks the γ phase. The stress is applied in the direction parallel to the Y-axis. Adopted from reference[10].

On the other hand, the creep response not only depends on the microstructure evolution but also on the changes in the dynamics and topology of the dislocations and dislocation networks [11]. At the beginning of creep loading, the deformation is governed by the dislocation glide and dislocation multiplication in the γ channels. Soon thereafter the mobile dislocations start to accumulate and become rearranged at the γ/γ' interface, while the formation of lamellar rafts takes place, leading to the widely observed formation of dislocation networks on the γ/γ' interface[11-15]. Analogous to the lamellar microstructure, the dislocation network will remain stable until the end of the stable creep stage (stage II creep) when the network begins to degrade by huge amounts of dislocations cutting into the rafted γ′

through the interface. Ultimately this chaotic dislocation multiplication process leads to rupture.

Summing up, the creep properties of Ni single crystal superalloys are strongly dependent on the combined effect of the microstructure evolution and the dislocation behaviour. Therefore, a good understanding and some quantification of microstructure and dislocation evolution during creep is crucial to better comprehend the mechanical properties of Ni superalloys. In this paper, the current work on the dependence of mechanical properties in Ni single crystals on the microstructural and dislocation behaviour during isothermal creep tests is reviewed. The experimental observations and the corresponding models and simulations are combined to show their mutual interaction. A simple model has been built in which the governing dislocation dynamics equation is thermodynamically coupled to the chemical composition of some commercial superalloys to predict their minimum creep rate at the loading conditions.

5.2 Microstructure evolution

5.2.1 Initial microstructure

The γ' precipitates in Ni superalloys undergo a succession of morphology changes from spheres to cubes during the heat treatments preceding the actual use phase. At the very beginning, the γ' precipitates nucleate as spheres to minimize the surface area[16]. As the particles grow, the misfit strain energy induced by the lattice and modulus mismatch between the γ and the γ' phase increases, and the precipitates become cuboids as the reduction in strain energy more than compensates for the increase in surface energy. It has been proven that cube morphology best minimizes the total energy of the precipitate as it provides the best balance between the anisotropic strain energy and the isotropic interfacial energy[17].

Nathal[18] has quantitatively investigated the optimal size of initial (i.e. as produced) particle and his work shows that alloys with an initial γ′ particle size between 0.35 and 0.5µm can pronouncedly outperform their counterparts with the same level of particle volume fraction but a different initial particle size. Hence the optimal initial microstructures consists of aligned cuboidal γ′ particles with a size around 0.4µm. This value of size has been widely adopted as the typical dimension of initial γ′ particles for most of the commercial Ni superalloys. To explore the possible "optimal" volume fraction of γ′ phase, Murakumo and co-workers started their study based on TMS-75 single crystal superalloy[2]. Results show that the dependence of the creep rupture life on the amount of γ′ was more evident in single crystals than in polycrystals, while the "optimal" amount of γ′ phase which leads to the longest creep lifetime is not a constant and varies with different service temperature. In some design models of Ni superalloys[19, 20], the optimal volume fraction of γ′ phase at different temperatures was generally set around 50%, which was mainly due to the dependence of topological inversion on the γ/γ′ volume.

5.2.2 Rafting stage

Rafting is one of the most pronounced characteristics of high temperature creep deformation in nickel-based superalloy single crystals[5, 7, 21, 22]. During creep tests at a high temperature and a low unidirectional applied stress, the microstructure in Ni superalloys gradually degrades by a directional coarsening process of γ′ precipitates. The initially adjacent cuboidal γ′ particles coalesce and form platelets that turn into plate-like or rod-like structures. The orientation of directional coarsening is closely related to the driving force of rafting, which is proportional to the product of applied stress and the lattice misfit[7, 23]. For negative misfitting alloys(where the lattice parameter of γ′ precipitates is smaller than that of γ matrix), N-type coalescence is observed (i.e. rafts form normal to the direction of the applied stress)

during tensile creep test, whereas P-type coalescence is obtained in compressive loading (i.e. rafts form parallel to the direction of the applied load). Conversely, for alloys with positive lattice misfit, the tensile loading leads to P-type coalescence and vice versa. Describing the morphological change in microstructure dimensions during rafting is a direct way to understand the evolution of mechanical properties.

To quantify the kinetics of rafting process, the key microstructural parameters presenting the morphology change need to be extracted and characterised. The γ channel widening is an important process during the creep seen in microstructures evolution, since γ channels are the conserved domains where dislocations propagate and glide during primary creep. Kamaraj investigated the kinetics of the widening of γ channels in the γ/γ′ microstructure, whose result suggests that multi-atom diffusion through the γ channels controls the widening process[24]. Later work by Serin further explored the effect of the level and state of applied stress on the kinetics of γ channel widening[25]. Results shown that <1 0 0> tension and 0 1 1<0 1 $\bar{1}$> shear creep deformation can equivalently lead to the same microstructure evolution, while γ channel widening rates increase with increasing stress level.

The structural periodicity λ in Ni superalloys is another important microstructural parameter and this is defined as the sum of the width of the N-channels and the extent of the γ′ phase in the direction parallel to applied stress[26]. This parameter characterizes the global coarsening of γ/γ′ microstructure since γ/γ′ composite morphology is almost periodical both for the initial microstructure and for the fully rafted microstructure[27]. Fedelich's work indicates that the microstructure period λ does not change remarkably during rafting, which means that rafting in essence is an anisotropic coarsening process. The growth of γ′ cuboids, characterized by the first increase in λ, precedes the coalescence of γ′ cuboids into rafts taking place without a great change in λ.

Rafting is generally considered as a creep hardening process, since the morphological change in γ/γ' in fact retards the evolution of creep strain[28-30]. Reed et al attributed this hardening effect to the closure of vertical γ channels during the morphology change[31]; the movement of dislocations contributing to the deformation creep is hindered by the lamellar structure with the orientation normal to the applied stress, leading to dislocation accumulation and rearrangement on the γ/γ' interface[12, 13].

5.2.3 Stable post-rafting stage and topological inversion

Generally, the rafting process is terminated at or before the stable creep stage. The fully rafted lamellar γ/γ' microstructure can hereafter maintain their morphology for a relatively long time, with only minor coarsening behaviour of γ' plates taking place[27, 32]. This stable post-rafting controls the microstructural dynamic recovery process, leading to a very slow accumulation of creep deformation.

At the end of creep stable stage with a sufficient time for the rearrangement of the lamellar morphology, the γ' phase gradually interconnects and is no longer confined by the γ channels. This evolution leads to an effect called "topological inversion": the γ' phase now surrounds the γ phase and topologically becomes the matrix[8, 33-36]. The moment of topological inversion has been proven to be strongly dependent on the initial volume fraction of γ' phases[37]. The reason for the formation of inversed microstructure has been studied in detail by many researchers[8, 9, 37]. It is generally accepted that after the rafting stage, the misfit stresses on γ/γ' interface are released by the dislocation network, and then the γ' precipitate size and morphology will evolve such as to minimize the total interfacial energy. This evolution is obtained by a reduction in γ/γ' interface area driven by diffusion-controlled coarsening of the γ' particles. For the modern Ni single crystal superalloys with a typical γ' fraction greater than 50% at service

temperature, the topological inversion of the γ/γ' microstructure is due to the minimization of the total γ/γ' interface area with the minor phase embedded in the major one. The occurrence of topological inversion is generally seen as the indicator of onset of accelerated creep[8, 36].

5.2.4 Break-up stage

After the inversion of the γ/γ′ microstructure, the creep resistance degrades, rapidly which finally leads to the failure of superalloys. Mughrabi ascribes this deterioration to a rapid increase in deformation induced by internal stresses, which cannot be released any longer by the interface dislocations once the γ phase is being split into discrete islands[38]. Other studies[33, 39, 40] have indicated that in the inversed microstructure the shape of γ/γ' interfaces changes from smooth into zigzag, leading to the formation of new dislocation glide planes in γ′, which correspondingly promote the formation of dislocation pile-ups and consequently cutting of the γ' phase.

5.2.5 Modelling of microstructure evolution

To interpret and further predict the directional coarsening behaviour of Ni superalloys, a large number of models have been proposed[32, 41-56]. Emphasis has been put on explaining the orientation of rafting based on driving force of morphology variation. Andre explains the behaviour in an elastic framework, where the elastic energy is calculated as a function of the particle shape, the applied stress and the ratio between the Young's modulus of the precipitates and that of the matrix[41]. The influence of plastic strains were added by considering the effect of unevenly distributed interfacial dislocations. Meanwhile the anisotropy in releasing the coherency stresses have been also simulated[42-44]. The original local stresses induced by the lattice and modules mismatch

distributed evenly in γ matrix. When the external stresses were applied on the materials, the local state of stress in γ/γ′ microstructure has been modified, which lead to anisotropic coarsening behaviours. The orientation dependence of elastic energy for different morphologies was then quantified for the combinations of transformation strain and matrix plastic strain[45]. These abovementioned models have pointed out that driving forces on rafting are in essence the lattice misfit, the external loading, and the difference in elastic constants between the two phases.

Besides, Other studies focused on quantitatively describing the kinetics of the morphology changes during rafting. Svodoba's model takes into account the interactions between dislocations and channels of γ matrix[46]. Through modelling the coarsening behaviour of γ' particles, the intricate creep behaviour can be well captured. Fedelich and co-workers made systematic studies to quantify the microstructural parameters of commercial alloy CMSX-4 during rafting process[32, 47, 48]. The direction widening behaviour of γ channel width is perfectly fitted as a function of time, stress and temperature, and the morphology description was further applied to build the constitutive model by connecting with creep properties[49].

Recently, the phase field method has emerged as a powerful way to capture the morphology change in Ni superalloys. Early phase field models were based on a elasticity framework only[50, 51], while the contributions from plastic strains were introduced in later models[52-54]. The principal criteria in all abovementioned models remain the lattice misfit, the elastic inhomogeneity and the applied load as the driving force for the directional coarsening., The effects of diffusion on the kinetics of rafting have been studied by coupling the phase field calculations with a CALPHAD approach[55, 56]. Results elucidate that Re addition retards the kinetics of rafting by slowing down the mobility of γ/γ′ interface.

5.3 Evolution of dislocation structures

5.3.1 Dislocations in initial microstructure

For the commercial Ni single crystal superalloys with the typical microstructure of aligned cubic γ′ embedded in γ matrix, the well-organized γ/γ′ coherent initial microstructure is obtained by a multi-step solution and aging treatment followed by a slow air-cooling process. The density of dislocations in the initial microstructure will be at a sufficiently low level after the high-temperature heat treatment and the as-processed γ/γ′ microstructure can be approximately considered as a dislocation-depleted state.

When the stress is applied during the early stages of creep, the dislocations are primarily emitted from the low-angle boundaries and percolate into the narrow γ channels. As creep deformation proceeds, the mobile individual dislocations become sequentially active and start to generate short avalanches of creep dislocations in boundary-free regions. Upon their activation, the density of creep dislocations in boundary-free regions rises by two orders of magnitude. Experimental observation at this stage shows that the γ/γ′ interfaces parallel to the applied stress are nearly devoid of dislocation, while dislocations are frequently observed on the γ channels normal to the stress axis[13]. The anisotropic distribution of dislocations in different γ channels is ascribed to the effect of unidirectional applied stress, which releases the misfit strain in parallel channels while introducing higher strains in the transverse channels[14, 57]. The deformation mechanism during primary creep has been generally interpreted as the rapid growth in dislocation density and the filling of γ channels with dislocations[33, 58, 59].

5.3.2 Formation of interfacial dislocation network

As the microstructure turns into rafts, the dislocations will accumulate at the γ/γ′ interfaces and form planar dislocation networks. It is commonly reported that networks form by the reaction of two dislocations with same Burgers vector to rearrange and generate new dislocations[14, 60-62], while Eggerler and co-workers also observed the formation of new dislocations on γ/γ' interface contributed by the interaction of two dislocations with different Burgers vector[63]. The formation of interfacial dislocations is usually believed to be driven by the release of lattice mismatch strain between the γ′ precipitate and γ matrix[12, 13]. The magnitude of lattice misfit is therefore of vital importance in the sense of determining the formation of the dislocation network. Zhang's experimental results[64] provide direct evidence for the dislocation networks evolution due to lattice misfit. In alloys with a large negative lattice misfit, the dislocations rearrange in the γ channels and form more complete and condensed dislocation networks and at a higher speed than in alloys with a small misfit Harada and co-workers[65] have isolated a quantitative correlation between the dislocation density of the equilibrium network and their creep performance in single crystal, with the dislocation spacing being found to be proportional to the logarithm of the minimum creep rate. The positive correlation between creep strength and interfacial dislocation density was also proven by Zhang's work[66]. Basically, the formation of interfacial dislocation network helps to release the γ/γ′ misfit strain, meanwhile contributes to the strengthening mechanism of γ/γ′ lamellar structure by hindering the cutting the mobile dislocations in the matrix.

5.3.3 Sustenance of the stable dislocation network

Experimental observations have shown that the networks can maintain their morphology and density during the secondary creep stage[62, 67,

68]. As mentioned above, the interfacial dislocation network can act as dislocation sinks to absorb/accommodate the matrix dislocations, thereby effectively preventing matrix dislocations from piling up at the interface[69]. Moreover, the dislocation networks also provide dislocation pins to prevent the matrix dislocations from cutting into the γ′ precipitate[11]. The stability of dislocation network helps to correspondingly stabilize the lamellar γ/γ′ structure during the stable creep stage.   So clearly there is mutual stabilisation.
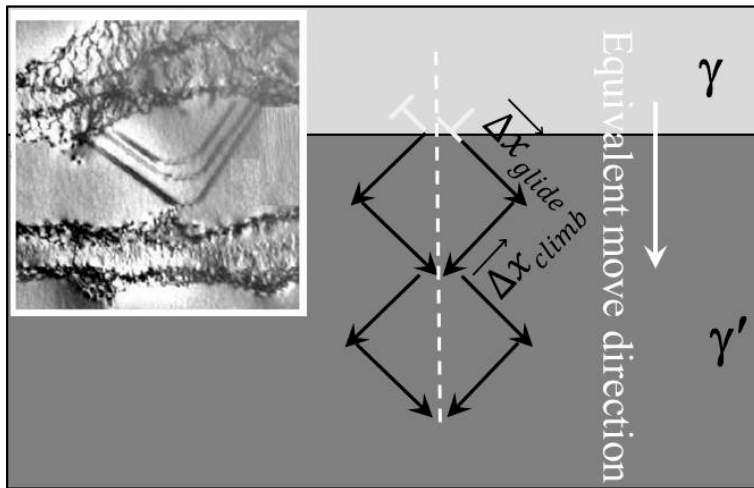
Figure 2. The 2D sketch for the superdislocations cutting into γ′rafts. reproduced from reference[70].

The stable stage for γ/γ′ interfacial dislocation network corresponds to the creep stable stage, which presents the microstructural dynamic recovery process with a very slow accumulation of creep deformation. Srinivasan investigated the recovery behaviour of mobile dislocations, focusing on the mechanism of γ' rafts cutting [70]. Experimental observations show that two dislocations with different Burgers' vectors in γ channel jointly shear the γ′ phase by forming a non-compacted superdislocation during [001] tensile creep. The two superpartials move into the γ′ phase by a combined process of glide and climb, which is equivalent to the migration of single superdislocation. The 2D schematic illustration is shown in figure 2. Similar results were proved by

experiments from many other researchers[71-74], while the superdislocation-cutting-γ′ mechanism has been widely accepted as the dominate recovery mechanism during creep stable stage. According to this climb-plus-glide cutting process, the rate-controlling step in creep is essentially the climb rate of dislocations in γ'.
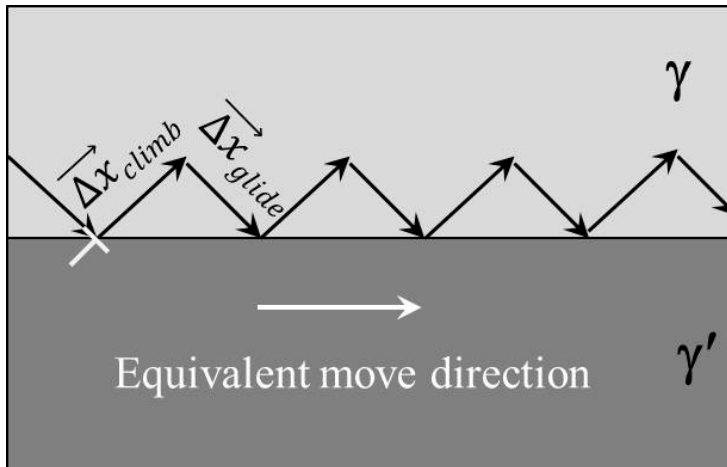
Figure 3. 2D sketch for the motion of a dislocation on γ/γ′ interface, reproduced from reference[75]

In addition, Epishin proposed another mechanism for dislocation movement during stable creep[33]. Here dislocations in the γ channels segregate on γ/γ′ interface during primary creep, then move transversely to the applied stress by a combination of glide and climb. while the gliding dislocations first get pinned by γ′ rafts. But with the help of osmotic forces produced by temperature and stress, trapped dislocations can climbs away from its original slip plane. Then the climbing dislocation can glide in a new slip plane again once its climb distance is large enough to afford a new glide step before it is blocked again by γ′ rafts. the 2D sketch of dislocation movement is shown in figure 3. As a result, the dislocations in the matrix channels can move along the γ/γ′ interface in a zig–zag manner as shown in the figure. Unlike the collective shearing of γ′ rafts, dislocations in this mechanism are

compact, and migrating only in γ matrix. A similar description of the dislocation migration on γ/γ′ interfaces can also be found in [75, 76].

5.3.4 Break-up of interfacial dislocation structure

The γ/γ′ microstructure becomes inversed when creep enters the tertiary stage. A large part of the dislocation network is still present on the γ/γ′ interfaces, but some are locally damaged in a later period of creep. The damaged networks lose the co-ordinating role of maintaining the dynamic equilibrium, so that a large number of dislocations are piled up at some regions where the networks have been damaged, giving rise to the local stress concentration[14]. Experimental results have shown that the {111}-type distorted interface forms as a consequence of the inversed microstructure[73, 74, 77]. The zigzag interface forms through dislocations which cut into the γ′ raft via {111} planes of interface[40]. The accelerated creep rate can then be attributed as the increased dislocation activity with the break-down of dislocation networks and the formation of new gliding planes.

5.3.5 Modelling the dislocation evolution

Based on a constitutive model for precipitate-strengthened alloys from Dyson[78], Zhu has developed a model by simulating the interaction between the dislocation and the γ′ particles with a cuboid morphology[76]. The rate-controlling step is assumed to be climb of dislocations at the matrix/particle interfaces, hereby the creep rate can be modelled as a function of microstructural parameter as well as intrinsic dislocation diffusivity.

At the mesoscopic scale, the main computational tool to study the dynamic collective evolution of dislocations under the external loading

is discrete dislocation dynamics (DDD) simulation. The application of DDD in Ni superalloys was primarily concerned with superdislocations in the γ' phase, focusing on the role of cube size and shape, phase volume fraction, temperature and anti-phase boundary energy[79-81]. Attention has been paid to the rafting domain to tackle dislocation plasticity in γ channels of γ/γ′ microstructures, which makes dislocation climb and vacancy diffusion become unavoidable key issues. In Hafez Haghighat's work, the movement of dislocations along the γ/γ′ interface close to the γ′ cube was interpreted as a combination of dislocation glide and climb, while the net dislocation motion is climb controlled[82]. Work done by Gao explicitly takes into account the vacancy-diffusion-coupled dislocation climb, which shows that dislocation climb can rearrange the dislocation configuration to relax the hardening due to dislocation filling γ channels[83]. Yang's work also puts emphasis on simulating the diffusion-induced dislocation climb to study the primary creep and early plastic behaviour[75]. The influences of microscale vacancy supersaturation and mesoscale phase morphology were described in detail. Using a DDD model, the effect of interfacial diffusion on the creep behaviour has been investigated by Shishvan[84]. Results show that interfacial diffusion helps to rearrange the dislocation distribution, as well as to relax the back-stresses induced by dislocations pile-up. The DDD model has also been combined with finite element method by Song to investigate the influence of interfacial dislocation networks and lattice mismatch on the dynamics of dislocation evolution in the matrix channels [85].

5.4 Discussion

5.4.1 The dependence of minimum creep rate on interfacial dislocation density
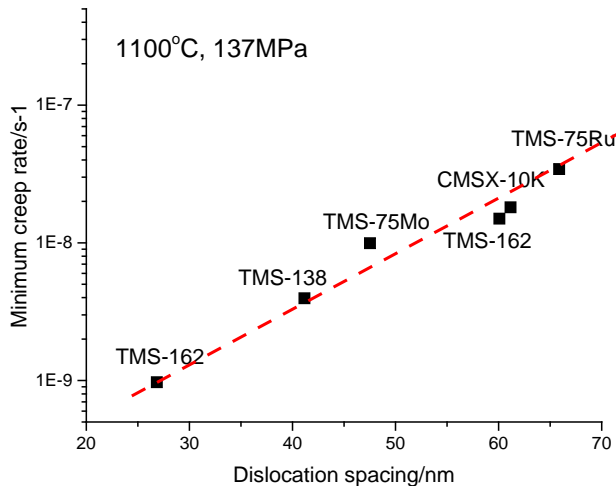
Figure 4. The minimum creep rate of commercial Ni single crystal superalloys as a function of interfacial dislocation spacing during 1100°C, 137MPa creep[11, 57, 65].

As shown in figure 4, the minimum creep rate of commercial Ni single crystal grades increases linearly with the spacing of the interfacial dislocations[11, 57, 65]. This phenomenological relationship can give an intuitive first-order connection between the creep properties and the dislocation properties. However, the parameter dislocation spacing is highly dependent on the accuracy of experimental observation. Moreover, the application of this relationship to quantify the creep behaviour of existing superalloys or further predict the properties of novel superalloys, is largely infeasible. To build a constitutive relationship with physical meanings instead of fitting equations, more detailed description in the dependence of dislocation behaviour needs to

be made, while the dislocation-behaviour-based deformation mechanism needs to be taken into consideration.

5.4.2 Simulation of dislocation behaviour

Formal statements have shown that the layered fully-rafted structure coupled with γ/γ' interfacial dislocation network can remain stable and keep almost unchanged for a relatively long time until rupture. Therefore, the investigation of creep properties as the dependence of dislocation behaviour should be focused on the post-rafting stage as the most long-lasting stage. As stated before, Srinivasan's research has shown that the γ' rafts can be cut by the superdislocation through a combined process of glide and climb, where the climbing velocity of superpartials are the controlling factors of creep rate[70]. The following discussion about creep is by default referred to the [001] tensile creep. Based on this results, the classic dislocation climb model from Anderson[86] was employed as a first order approximation to estimate the dislocation mobility, where the climbing rate of dislocations in γ' phase $v_{c'}$ has been presented as follows:

$$v_c' = \frac{2\pi D_s (e^{\frac{\sigma_{xx} V_{a'}}{kT}} - 1)}{b \, ln(R'/b)} \qquad (1)$$

where $D_{s'}$ is the diffusivity of γ', σ_{xx} is the applied stress, $V_{a'}$ is the atomic volume of γ', b is the Burger's vector, R' is the average dislocation spacing in γ' and $R' \approx \sqrt{1/\rho_{\gamma'}}$, and $\rho_{\gamma'}$ is the dislocation density in γ' phase.

For the dislocation zig-zag movement along the γ/γ' interface proposed by Epishin[33], the creep rate controlling factor of this mechanism is similarly the dislocation climb rate. Here the compact dislocations move

along γ/γ′ interface without superpartials, and the γ matrix is the domain of dislocation migration. Anderson's theory was again employed [86], and the climbing rate of dislocation on γ/γ′ interface was shown as follows:

$$v_c = \frac{2\pi D_s (e^{\frac{\sigma_{xx} V_a}{kT}} - 1)}{b \, ln(R/b)} \qquad (2)$$

where D_s is the diffusivity of g, Va is the atomic volume of g, R stands for the average distance of dislocations on the γ/γ′ interface. The interfacial dislocation density of Ni superalloys has been reported by many researchers as a function of lattice misfit[68], where the spacing of dislocation network $R = \frac{|b|}{|\delta|}$. here δ is the lattice misfit presenting by $\delta = \frac{a_{\gamma'} - a_\gamma}{a_\gamma}$. $a_{\gamma'}$ and a_γ are the lattice parameter of γ' and γ phase respectively. So the equation was represented in the following way:

$$v_c = \frac{2\pi D_s (e^{\frac{\sigma_{xx} V_a}{kT}} - 1)}{-b \, ln|\delta|} \qquad (3)$$

In this paper, the lattice misfit is obtained, from the lattice parameters of γ/γ′ phases calculated through their molar volumes $a = \sqrt[3]{\frac{4V_m}{NA}}$. For the calculation of diffusion coefficient in the multi-element alloy system, a harmonic mean of calculation is selected based on Zhu's work[76], i.e., $D_s = \frac{1}{\sum_m x_m / D_0^m}$.

By now the creep rate-controlling behaviours of dislocations in γ and γ′ phase have been presented respectively. After figuring out the underlying deformation mechanism originating from dislocation

behaviour, the creep behaviour of superalloys can be then interpreted as the combination of these two mechanism.

5.4.3 Simulation of minimum creep rate

For the fully rafted γ/γ' lamellar microstructure, the creep behaviour can be approximately equal to the composites reinforced by the continuous lamellae, which are oriented perpendicular to the applied stress. Assuming an iso-stress condition[87], the strain rate of alloy can be presented by the following equation:

$$\dot{\varepsilon} = \dot{\varepsilon_\gamma} V_\gamma + \dot{\varepsilon_{\gamma'}} V_{\gamma'} \qquad (4)$$

Where V_γ and $V_{\gamma'}$ are the volume fraction of $\gamma/$ and γ' phase respectively. According to the Orowan law, the strain rate in g and g' phase can be written as

$$\dot{\varepsilon_\gamma} = \bar{M} \rho_\gamma b v_c \qquad (5)$$

Where ρ_γ stands for the dislocation density in γ; and $\bar{M}$ is the Schmid factor.

However, the abovementioned equation describes the creep properties of alloys with a lamellar microstructure without taking into consideration the distribution of lamellae spacing, and the effect of inter-spacing of lamellae need to be further interpreted. Whitely proposed a model based on the Bailey-Norton creep equation to describe Al-CuAl$_2$ eutectic alloy with lamellar structure[88], where dislocation-motion related microstructural parameter, inter-lamellar spacing L, was added, as shown by the following equation

$$\dot{\varepsilon} \propto L^n \qquad (6)$$

where n is the lamellar spacing exponent. Theoretically n should be equal to 1 for a perfectly aligned and continuous fiber (or plate) reinforced composite, but it will be as high as 3 if fiber (or plate) rupture occurs. The application of equation can also be found [89, 90] with similar well-aligned lamellar structure. In this work the lamellar inter-spacing can be defined as the channel width of γ' phase to present the periodical microstructure. According to the geometrical relationship, L can be expressed in the following way:

$$L = \frac{V_{\gamma'}}{1 - V_{\gamma'}^{1/3}} \; \omega_0 \tag{7}$$

Where ω_0 is the initial size of γ' particles.

Combining all, the creep rate can be expressed by the following equation:

$$\dot{\varepsilon} = L^n \left(\frac{2\pi \bar{M} V_{\gamma'} \rho_\gamma D_{s'} \left(e^{\frac{\sigma_{xx} V_{a'}}{kT}} - 1 \right)}{\ln\left(\frac{R'}{b}\right)} - \frac{2\pi \bar{M} \rho_\gamma V_\gamma D_s (e^{\frac{\sigma_{xx} V_a}{kT}} - 1)}{ln|\delta|} \right) \tag{8}$$

The creep properties of Ni superalloys can be presented by dislocation behaviour through building the climb-assisted equation with the consideration of lamellar microstructure. In equation, the parameters such as phase volume fraction V_γ and $V_{\gamma'}$, diffusivity D_s and $D_{s'}$, and lattice misfit δ are thermodynamic factors that are strongly related to chemical composition. The mechanical properties of superalloys can be then connected with the composition when these thermodynamic parameters can be properly obtained as a consequence of composition. While the model as given by equation (8) is probably conceptually correct, the large number of physical parameters which values cannot be obtained independently , implies that the model cannot easily be used for the compositional optimisation of existing alloys, nor the design of new superalloys.

In the field of superalloys, the implementation of CALPHAD-based thermodynamic models is now an emerging approach, where

equilibrium microstructural features of complex multi-component alloys, such as phase fraction, element partition and diffusivity, can be well captured by using Gibbs free energy databases. Values for the parameters such as Vf, V_m, x_m, Ds were calculated via Thermo-calc using TCNI9 and MOB2 database. Since the minimum creep rate is also a function of the (a-priori unknown) dislocation density in γ and γ' phase in the following simulations it was pre-set as a constant. This is a slight simplification but helps us to illustrate the effect of composition-related factors. The microstructural parameters and physical constants used in equation are listed in table 1[70, 76].

Table 1. The microstructural parameters and physical constants used in equation[70, 76].

Lamellar spacing exponent n	1.5
Schmid factor $\bar{M}$	$1/\sqrt{6}$
Burger's factor b	2.5×10^{-10} m
Dislocation density in γ' phase $\rho_{\gamma'}$	10^9 m^{-2}
Dislocation density in γ phase ρ_{γ}	10^{11} m^{-2}
Initial size of γ' particles ω_0	4×10^{-7} m

5.4.5 Validation of minimum creep rate in existing Ni commercials
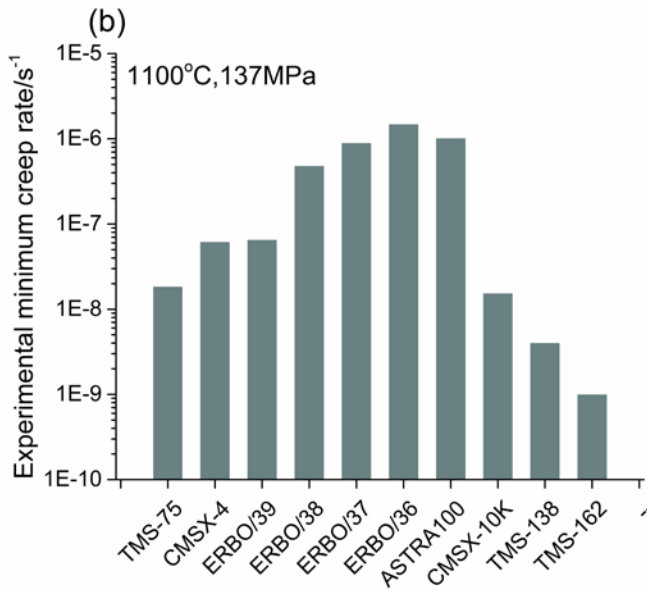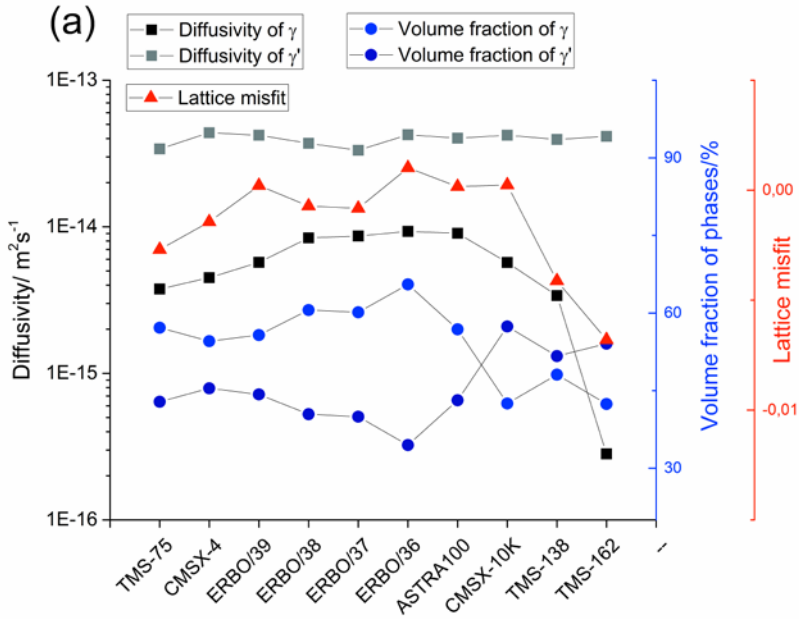
Figure 5. The calculated diffusivity and volume fraction of γ and γ′ phase, as well as the lattice misfit of existing Ni single crystal grades at 1100°C (a), and the experimental minimum creep rates of alloys at 1100°C, 137MPa[65, 91, 92] (b). The lines connecting the individual data points have no physical meaning and are only added to guide the eye. The order of the superalloys along the x-axis is based on the generation of Ni commercial single crystal superalloys.

To illustrate the model's capability in reproducing the creep properties of superalloys, existing commercial grades of Ni single crystals have been employed with their chemical compositions shown in table 2. Based on the composition, the volume fraction as well as the diffusivity of γ and γ′ phase in existing alloys at 1100°C are calculated and shown in figure 5.

In figure 5a, the square dots with black and grey colour indicate the calculated diffusion coefficient in γ and γ′ phases respectively. For all alloys, almost no difference can be found in the diffusivity of γ′ phase, due to the relatively small solubility of alloying elements in the Ni_3Al intermetallic. In comparison, the diffusivity in TMS-138 and TMS-162 alloys is significantly smaller than that in the other alloys, which is understandable due to the more heavily alloying by refractory elements (such as Re and Mo) in TMS series. Also, the calculated results demonstrate that difference of diffusivity in γ′ is small but that in γ is big, which implies the diffusion behaviour in γ phase is the dominate mechanism in deformation which leads to the difference in creep behaviour for Ni commercial grades. The round dots present the phase volume fractions of listing alloys, where ASTRA100, ERBO/36, ERBO/37 and ERBO/38 alloys have a relatively low values of γ′ volume fraction around 35%. The red triangle dots show the calculated lattice misfits of all alloys. The TMS alloys generally possess large negative misfits, while the lattice mismatch of other alloys fluctuates around zero with small difference. Figure 5b shows the experimental minimum creep rates of these alloys at 1100°C and 137MPa. TMS-162 alloy

pronouncedly outperforms other alloys while ERBO/36 has the worst performance in creep. The influence factors corresponding to the composition-related parameters have been analysed.
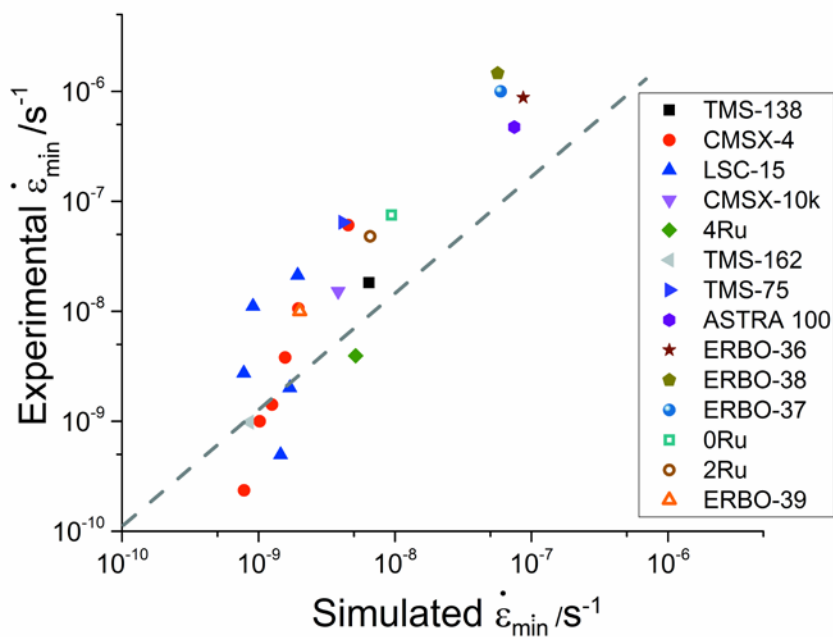
Figure 6. The simulated minimum creep rate of existing Ni commercial grades compared with the experimental results obtained from the literature [65, 77, 91-94]

Table 2. The chemical composition of commercial Ni single crystal superalloys (in wt.%) [65, 77, 91-94]

	Al	*Co*	*Cr*	*Hf*	*Mo*	*Re*	*Ru*	*Ta*	*Ti*	*W*	*Ni*
TMS-75	6	12	3	0,1	2	5	-	6	-	6	
CMSX-4	5,6	9	6,5	0,1	0,6	3	-	6,5	1	6	
ERBO/39	4,4	8,92	5,11	-	0,97	-	-	6,7	3	9	
ERBO/38	5,54	8,71	5,12	-	0,95	-	-	6,54	0,79	9,05	
ERBO/37	6	8,74	5,14	-	0,95	-	-	6,56	-	9,09	
ERBO/36	5,65	8,89	5,23	-	0,96	-	-	6,67	-	6,19	
ASTRA100	6,13	8,92	5,25	-	0,97	-	-	6,7	-	6,19	*bal*
CMSX-10K	5,7	3	2	0,03	0,4	6	-	8	0,2	5	
TMS-138	5,9	5,9	2,9	0,1	2,9	4,9	2	5,6	-	5,9	
TMS-162	5,8	5,8	2,9	0,1	3,9	4,9	6	5,6	-	5,8	
LSC-15	4	6	7	0,1	1,5	-	-	5,5	-	10	
SX-0Ru	6	-	4	-	1	4	0	5	0,5	5	
SX-2Ru	6	-	4	-	1	4	2	5	0,5	5	
SX-4Ru	6	-	4	-	1	4	4	5	0,5	5	

Figure 6 shows the comparison between the experimental minimum creep rates of existing Ni grades, and the calculated minimum creep rates obtained from thermodynamic simulations. The selected experimental data are obtained from different temperature and stress ranges [65, 77, 91-94]. Results show that compared to the experimental results, the creep rates are generally overestimated by the simulations, as indicated by the red dash line. But it is worth pointing out this model based on the simulation of dislocation movement can well reproduce the creep properties of existing Ni superalloys at different temperature and stress ranges,. Hence, through thermodynamic and kinetic calculations, the chemical compositions of Ni superalloys can be successfully coupled to their creep performance by this model without making the dislocation specifications themselves composition dependent.

Conclusions

1. The high performance of Ni single crystal superalloys during high temperature low stress creep service, is primarily controlled by the combined effects of microstructural evolution, namely the formation of rafting lamellae, and the dislocation behaviour, i.e., the well-arranged dislocation network located on the γ/γ' interface.

2. During the secondary creep stage which takes longest time of creep life, two main recovery mechanism based on dislocation migration dominate the process. One is superdislocations shearing into γ' rafts through a two-superpartials-assisted approach. Another is the compact dislocations migrating along γ/γ' interface. These two mechanisms are similarly climb-rate-controlled process.

3. A model for the minimum creep rate based on thermodynamic and kinetic calculations and using an existing detailed dislocation dynamics model has been built by taking the dislocation migration behaviours as well as the rafted microstructure into

consideration, which can well reproduce the creep properties of existing Ni superalloy grades.

Reference

[1]   Reed RC. The superalloys: fundamentals and applications: Cambridge university press, 2008.
[2]   Murakumo T, Kobayashi T, Koizumi Y, Harada H. Acta Mater 2004;52:3737.
[3]   Shui L, Jin T, Tian S, Hu Z. Mater Sci Eng A 2007;454–455:461.
[4]   Ricks RA, Porter AJ, Ecob RC. Acta Metall 1983;31:43.
[5]   Johnson W, Berkenpas M, Laughlin D. Acta Metall 1988;36:3149.
[6]   Socrate S, Parks DM. Acta Metall Mater 1993;41:2185.
[7]   Nabarro FR. Metall Mater Trans A 1996;27:513.
[8]   Epishin A, Link T, Brückner U, Portella P. Acta Mater 2001;49:4017.
[9]   Goerler JV, Lopez-Galilea I, Mujica Roncery L, Shchyglo O, Theisen W, Steinbach I. Acta Mater 2017;124:151.
[10]   Tan XP, Liu JL, Jin T, Hu ZQ, Hong HU, Choi BG, Kim IS, Jo CY. Mater Sci Eng A 2011;528:8381.
[11]   Zhang J, Murakumo T, Koizumi Y, Kobayashi T, Harada H, Masaki Jr S. Metall Mater Trans A 2002;33:3741.
[12]   Lasalmonie A, Strudel J. Philos Mag 1975;32:937.
[13]   Gabb T, Draper S, Hull D, MacKay R, Nathal M. Mater Sci Eng A 1989;118:59.
[14]   Sugui T, Huihua Z, Jinghua Z, Hongcai Y, Yongbo X, Zhuangqi H. Mater Sci Eng A 2000;279:160.
[15]   Zhang J, Harada H, Koizumi Y, Kobayashi T. J Mater Sci 2010;45:523.
[16]   Ricks R, Porter A, Ecob R. Acta Metallurgica 1983;31:43.
[17]   Baldan A. J Mater Sci 2002;37:2379.
[18]   Nathal M. Metall Trans A 1987;18:1961.

[19]   Zhu Z, Höglund L, Larsson H, Reed RC. Acta Mater 2015;90:330.

[20]   Rettig R, Ritter NC, Helmer HE, Neumeier S, Singer RF. Model Simul Mater Sc 2015;23:035004.

[21]   Kamaraj M. Sadhana 2003;28:115.

[22]   Johnson WC. Metall Trans A 1987;18:233.

[23]   Ignat M, Buffiere J-Y, Chaix J. Acta Metall Mater 1993;41:855.

[24]   Kamaraj M, Serin K, Kolbe M, Eggeler G. Mater Sci Eng A 2001;319:796.

[25]   Serin K, Göbenli G, Eggeler G. Mater Sci Eng A 2004;387:133.

[26]   Epishin A, Link T, Portella P, Brückner U. Acta Mater 2000;48:4169.

[27]   Epishin A, Link T, Klingelhöffer H, Fedelich B, Brückner U, Portella PD. Mater Sci Eng A 2009;510:262.

[28]   Mughrabi H, Tetzlaff U. Adv Eng Mater 2000;2:319.

[29]   Reed RC, Cox DC, Rae CMF. Mater Sci Technol-lond 2007;23:893.

[30]   Rae C, Reed R. Acta Mater 2007;55:1067.

[31]   Reed R, Matan N, Cox D, Rist M, Rae C. Acta Mater 1999;47:3367.

[32]   Fedelich B, Künecke G, Epishin A, Link T, Portella P. Mater Sci Eng A 2009;510-511:273.

[33]   Epishin A, Link T. Philos Mag 2004;84:1979.

[34]   Caron P, Benyoucef M, Coujou A, Crestou J, Clement N. ONERA, TP no. 2000-230 2000.

[35]   Fredholm A, Strudel J-L. High temperature creep mechanisms in single crystals of some high performance nickel base superalloys. High Temperature Alloys. Springer, 1987. p.9.

[36]   Walston W, O'hara K, Ross E, Pollock T, Murphy W. RENE N6: THIRD GENERATION SINGLE CRYSTAL SUPERALLOY. Superalloy 1996. Warrendale, PA, 1996. p.27.

[37]   Caron P, Ramusat C, Diologent F. Superalloys 2008 2008:159.

[38]   Mughrabi H. γ/γ'rafting and its effect on the creep and fatigue behaviour of monocrystalline superalloys. The Johannes Weertman Symposium, 1996. p.267.

[39]   Pollock TM, Argon AS. Acta Metall Mater 1992;40:1.

[40]   Ru Y, Li S, Zhou J, Pei Y, Wang H, Gong S, Xu H. Sci. Rep. 2016;6:1.

[41]   Pineau A. Acta Metall 1976;24:559.

[42]   Arrell D, Vallés J. Scr Metall Mater 1994;30.

[43]   Buffiere JY, Ignat M. Acta Metall Mater 1995;43:1791.

[44]   Matan N, Cox D, Rae C, Reed R. Acta Mater 1999;47:2031.

[45]   Ratel N, Bruno G, Bastie P, Mori T. Acta Mater 2006;54:5087.

[46]   Svoboda J, Lukáš P. Acta Mater 1998;46:3421.

[47]   Fedelich B, Epishin A, Link T, Klingelhöffer H, Künecke G, Portella PD. Comp Mater Sci 2012;64:2.

[48]   Fedelich B, Epishin A, Link T, Klingelhöffer H, Künecke G, Portella PD. Rafting during high temperature deformation in a single crystal superalloy: experiments and modeling. Superalloys 2012. TMS, 2012. p.491.

[49]   Tinga T, Brekelmans W, Geers M. Comp Mater Sci 2009;47:471.

[50]   Gururajan M, Abinandanan T. Acta Mater 2007;55:5015.

[51]   Li D, Chen L. Acta Mater 1998;47:247.

[52]   Boussinot G, Le Bouar Y, Finel A. Acta Mater 2010;58:4170.

[53]   Zhou N, Shen C, Mills M, Wang Y. Acta Mater 2007;55:5369.

[54]   Zhou N, Lv D, Zhang H, McAllister D, Zhang F, Mills M, Wang Y. Acta Mater 2014;65:270.

[55]   Mushongera LT, Fleck M, Kundin J, Wang Y, Emmerich H. Acta Mater 2015;93:60.

[56]   Wen YH, Lill JV, Chen SL, Simmons JP. Acta Mater 2010;58:875.

[57]   Zhang J, Murakumo T, Harada H, Koizumi Y. Scr Mater 2003;48:287.

[58]   Link T, Epishin A, Brückner U, Portella P. Acta Mater 2000;48:1981.

[59]   Schneider W, Mughrabi H. Creep and Fracture of Engineering Materials and Structures 1993:209.

[60]   Keller RR, Maier HJ, Mughrabi H. Scr Metall Mater 1993;28:23.

[61]   Gabrisch H, Mukherji D, Wahi R. Philosophical Magazine A 1996;74:229.

[62]   Gabrisch H, Mukherji D. Acta Mater 2000;48:3157.

[63]   Eggeler G, Dlouhy A. Acta Mater 1997;45:4251.

[64]   Zhang JX, Wang JC, Harada H, Koizumi Y. Acta Mater 2005;53:4623.

[65]   Koizumi Y, Kobayashi T, Yokokawa T, Zhang J, Osawa M, Harada H, Aoki Y, Arai M. Superalloys 2004 2004:35.

[66]   Zhang JX, Murakumo T, Harada H, Koizumi Y. Scripta Materialia 2003;48:287.

[67]   Zhu T, Wang C-y. Phys Rev B 2005;72.

[68]   Carroll L, Feng Q, Pollock T. Metall Mater Trans A 2008;39:1290.

[69]   Luo ZP, Wu ZT, Miller DJ. Mater Sci Eng A 2003;354:358.
[70]   Srinivasan R, Eggeler GF, Mills MJ. Acta Mater 2000;48:4867.
[71]   Kostka A, Mälzer G, Eggeler G, Dlouhy A, Reese S, Mack T. J Mater Sci 2007;42:3951.
[72]   le Graverend JB, Cormier J, Gallerneau F, Villechaise P, Kruch S, Mendez J. Int J Plasticity 2014;59:55.
[73]   Agudo Jácome L, Nörtershäuser P, Heyer JK, Lahni A, Frenzel J, Dlouhy A, Somsen C, Eggeler G. Acta Mater 2013;61:2926.
[74]   Agudo Jácome L, Nörtershäuser P, Somsen C, Dlouhý A, Eggeler G. Acta Mater 2014;69:246.
[75]   Yang H, Huang M, Li Z. Comp Mater Sci 2015;99:348.
[76]   Zhu Z, Basoalto H, Warnken N, Reed R. Acta Mater 2012;60:4888.
[77]   Tan XP, Liu JL, Jin T, Hu ZQ, Hong HU, Choi BG, Kim IS, Jo CY, Mangelinck D. Mater Sci Eng A 2013;580:21.
[78]   Dyson B. Mater Sci Technol-lond 2009;25:213.
[79]   Yashiro K, Kurose F, Nakashima Y, Kubo K, Tomita Y, Zbib HM. Int J Plasticity 2006;22:713.
[80]   Rao SI, Parthasarathy TA, Dimiduk DM, Hazzledine PM. Philos Mag 2004;84:3195.
[81]   Vattré A, Devincre B, Roos A. Intermetallics 2009;17:988.
[82]   Hafez Haghighat SM, Eggeler G, Raabe D. Acta Mater 2013;61:3709.
[83]   Gao S, Fivel M, Ma A, Hartmaier A. J Mech Phys Solids 2017;102:209.
[84]   Shishvan SS, McMeeking RM, Pollock TM, Deshpande VS. Acta Mater 2017;135:188.
[85]   Huang S, Huang M, Li Z. Int J Plasticity 2018;110:1.
[86]   Anderson PM, Hirth JP, Lothe J. Theory of dislocations: Cambridge University Press, 2017.
[87]   Bartholomeusz MF, Wert JA. Metall Mater Trans A 1994;25:2161.
[88]   Schmidt-Whitley RD. Z Metallkd 1973;64:552.
[89]   Mason D, Van Aken D. Acta Metall Mater 1995;43:1201.
[90]   Hagihara K, Araki H, Ikenishi T, Nakano T. Acta Mater 2016;107:196.
[91]   Kondo Y, Miura N, Matsuo T. Stress Exponent of Minimum Creep Rate of Single Crystal Nickel-Based Superalloy, CMSX-4, AT 1273K. Mater Sci Forum, vol. 539: Trans Tech Publ, 2007. p.3100.

[92]   Pröbstle M, Neumeier S, Feldner P, Rettig R, Helmer H, Singer
        R, Göken M. Mater Sci Eng A 2016;676:411.
[93]   Wollgramm P, Buck H, Neuking K, Parsa AB, Schuwalow S,
        Rogal J, Drautz R, Eggeler G. Mater Sci Eng A 2015;628:382.
[94]   Guédou JY, Tsuno N, Takahashi S, Choné J. MATEC Web of
        Conferences 2014;14:20002.

The compositional dependence of the microstructure and properties of CMSX-4 superalloys

The degradation of creep resistance in Nickel-based single crystal superalloys is essentially ascribed to their microstructure evolution. Yet there is a lack of work that manages to predict (even qualitatively) the effect of alloying element concentrations on the rate of microstructure degradation. In this research, a computational model is presented to connect the rafting kinetics of Ni superalloys to their chemical composition by combining thermodynamics calculation and a modified microstructure model. To simulate the evolution of key microstructural parameters during creep, the isotropic coarsening rate and γ/γ' misfit stress has been defined as composition related parameters, and the effect of service temperature, time and applied stress are taken into consideration. Two commercial superalloys for which the kinetics of the rafting process are selected as the reference alloys, and the corresponding microstructural parameters are simulated and compared with experimental observations reported in the literature. The results confirm that our physical model not requiring any fitting parameters manages to predict (semi-quantitatively) the microstructure parameters for different service condition, as well as the effects of alloying element concentrations. The model can contribute to the computational design of new Ni-based superalloys.

6.1 Introduction

The outstanding high-temperature mechanical performance of Nickel based single crystal superalloys, in particular their superior creep resistance makes them favourite materials for turbine blades in aero engines[1]. Their interesting properties are largely dictated by the high-volume fraction (up to 70%) of ordered, $L1_2$ structured γ' precipitates, which are coherently embedded in a solid solution strengthened γ matrix (FCC structure). During the high temperature creep process above 900^0C, the creep behaviour strongly depends on the microstructural evolution. Specifically, in the early creep stage of so-called negative misfitting alloys, initially adjacent cuboidal γ' particles coalesce and turn into plate-like structures which are normal to the stress direction. This microstructure of alternating platelets of γ and γ' phases is called the rafted structure. The lamellar structure is rather stable and essentially blocks the dislocation bypassing mechanism, resulting in a low creep rate during the secondary creep stage. In the later stage of creep, the destabilisation of the rafted microstructure occurs through a topological inversion of γ/γ' microstructure, resulting in a steep increase in the creep rate.   Hence, the creep kinetics can be linked to the process of microstructure evolution, and it is of great importance to identify the main microstructural evolution mechanisms and to incorporate their effects as a function of service conditions.

The characterization of microstructure evolution during creep process is of utmost importance in detecting the desirable mechanical properties of Ni single crystalline superalloys. Hence since the 1990s a large number of models has been derived to describe and investigate the progress of γ' morphology evolution. Most of them focus on the dynamics of dislocation behaviour, exploring the balance between dislocation multiplication and interaction with precipitates, as well as dislocation annihilation and recovery[2-6]. Other models focus on probing the driving force of the anisotropic coarsening of precipitates[7-10]. Essentially, the microstructure characteristics for Ni superalloys are

determined by three factors: γ' precipitate volume fraction, isotropic coarsening and directional coarsening, also called rafting. There are two main parameters in describing the rafted microstructure, i.e. the microstructural periodicity λ and the γ channel width ω. This λ parameter characterizes the global coarsening of the γ/γ' microstructure, since the rafted γ/γ' composite morphology is found to be almost independent of the initial microstructure. The widening of the γ channel width which is perpendicular to the uniaxial applied stress is also an important process in presenting creep kinetics during microstructure evolution, since the channel width determines the dislocation motion due to the Orowan mechanism and their accumulation. The γ channel widening is driven by the superimposition of internal misfit stress and the uniaxial applied stress, which can significantly affect the kinetics of the anisotropic coarsening mechanism.

As mentioned above, the creep kinetics are linked to the process of microstructural evolution, which is not only a function of the imposed loading conditions but also of the chemical composition of the superalloy. However, there are only few studies that attempt to show the effect of alloying element concentrations on microstructure evolution[11-13], because of the large number of potential interactions between the alloying elements, and the complex dependences on service temperature, time and applied stress that need to be evaluated. Theoretical analyses and computer modelling tools might conceivably provide a qualitative or semi-quantitative method to solve this problems[14, 15]. In the present paper, the Ni single crystal commercial grades CMSX-4 and René N4 are selected as the reference alloys, since their microstructure parameters and creep behaviour during different creep tests have been reported in quite some detail[1, 16-19]. A novel computational design model predicting the microstructure development during creep process, is presented in which thermodynamic data are combined with an energy based microstructure evolution model. The microstructural features are computationally linked to the chemical composition, and the simulated results are validated against

experimental observations. Specifically, the conditions considered in this work correspond to the coalescence of cubic γ′ precipitates at elevated service temperatures (above 1173K, 900 ^{0}C), leading to the lamellar structure under uniaxial <001> tensile loading. Other loading conditions (uniaxial compression, multiaxial stress, cyclic loading et al.) are outside the scope of this work.

6.2 Model description

In this section, a model which combines thermodynamic calculations with two representative methods that describe the microstructural evolution of CMSX-4 and René N4 superalloys is presented. The effects of chemical compositions are introduced and the corresponding microstructural parameters can be predicted as a function of stress and temperature. For the relatively limited composition domain explored in this work, the composition dependence of dislocation behaviour is ignored. The nominal chemical compositions of commercial superalloy CMSX-4 and René N4 are shown in table 6.1.

Table 6.1 Nominal chemical compositions of commercial superalloys
CMSX-4 and René N4 (in wt.%)

	Al	*Co*	*Cr*	*W*	*Mo*	*Ta*	*Ti*	*Re*
CMSX-4	5.6	9.0	6.5	6.0	0.6	6.5	1.0	3.0
René N4	3.7	8.0	9.0	6.0	2.0	4.0	4.2	–

6.2.1 Fedelich's phenomenological model

Recently Fedelich[20] and co-workers measured the increase in the microstructural periodicity λ and the γ channel width ω of CMSX-4 commercial superalloys as a function of service time, temperature and applied stress. An analytical expression has been proposed which seems to capture the findings from detailed observations on the transition of γ' morphology from cuboid to rafted shape. In their work, the processes of isotropic coarsening and unidirectional coarsening, i.e., rafting, are considered separately and are assumed to be governed by different driving mechanism. Based on geometrical considerations, the channel width in the two different procedures is given by:

$$\omega_{cube}(t) = (1 - \sqrt[3]{f_\gamma})\lambda(t) \qquad\qquad (1)$$

$$\omega_{raft}(t) = (1 - f_\gamma)\lambda(t) \qquad\qquad (2)$$

Where $f_{\gamma'}$ is the volume fraction of precipitates and $\lambda(t)$ is the microstructure periodicity. The isotropic coarsening of $\lambda(t)$ has been captured by the fitted equation used for specimens crept at 1223K (950^{0}C):

$$\lambda(t) = \lambda_0\sqrt{1 + \beta t} \qquad\qquad (3)$$

A dimensionless parameter, termed rafting degree ξ, is defined to quantify the microstructural changes. It presents the normalised channel width, which increases from 0 to 1 when microstructure changes from cubes to plates:

$$\xi = \frac{\omega(t) - \omega_{cube}(t)}{\omega_{raft}(t) - \omega_{cube}(t)} \qquad (4)$$

The analytical expression to describe   the degree of rafting as a function of time and external stress based on experimental results has been given by:

$$\xi = 1 - \exp(-b\sigma^n t) \qquad (5)$$

Basically, the above-mentioned model is an experiment-based analytical expression which can only be applied for CMSX-4 alloy at the temperature 1223K (950^{0}C), where β, b, n are all fitting parameters not having any physical meaning. To extend the application scope of this model over a wider temperature range, Fedelich[21] further collected the microstructure evolution data of CMSX-4 over a wide temperature range, and built the following equation to describe the kinetics of evolving periodicity and channel width:

$$\lambda_{[001]} = \lambda_{[001]}^0 \left[1 + D_0 \exp(-\frac{Q_\lambda}{RT})t \right]^a \qquad (6)$$

$$\omega_{[001]} = \omega_{cube} + \left(\omega_{raft} - \omega_{cube} \right)$$
$$\left\{ 1 - exp \left[-A_0 \exp(-\frac{Q_\xi}{RT}) \left(1 + \frac{\sigma}{\sigma_0} \right)^p t \right] \right\} \qquad (7)$$

In these two equations, D_o, Q_λ, a, A_0, Q_ξ, σ_0 and p are also fitting parameters. This modified equation excellently describes the microstructure degradation of CMSX-4 at different stress and temperature levels with the correlation factors $r^2 > 0.97$. However, all the parameter values in the equation remain fitted values, which means for other superalloy systems with slightly different chemical compositions, the applicability of the model should be re-assessed and the parameter values need to be re-determined.

6.2.2 Fan's model

Fan and his co-workers [22] follow the approach of Fedelich's work[20] in describing the channel width and rafting degree but attempt to bring in a more physical approach. They describe the isotropic coarsening of the microstructural periodicity, as follows:

$$\lambda(t)^3 - \lambda_0^3 = \frac{BQ}{RT} t \qquad (8)$$

In this equation, B is material constant and Q is the activation energy. One could argue that the Oswald ripening mechanism is describes the coarsening of spherical particles, while the actual microstructure in the superalloys considered is a lamellar structure. But it would be reasonable to simplify the coarsening kinetics of lamellar structures in the same way since essentially it is the overall interfacial energy that drives the coarsening mechanism. Recent studies[23, 24] also show that the isotropic coarsening rate as in the LSW coarsening mechanism can be applied as an indicator of creep properties in Ni superalloys. In this model the isotropic coarsening rate is proportional to temperature and determined by two constants, while no formal connection to the chemical composition is assumed.

According to Fan's study, in the directional coarsening process, γ' precipitates only change their shape from cubes to rafts while the precipitate volume remaining constant, since the change of γ' volume has been included in the isotropic coarsening. The driving force for rafting is the strain energy ψ, which equals the distortion strain energy since the volumetric strain energy is zero. The strain energy during rafting is formulated as:

$$\psi = v_d = (1 - c\xi) \frac{1 + v}{3E} \sigma_s^2 \qquad (9)$$

where υ_d is the distortion strain energy, E is the elastic modulus, υ is the Poisson ratio and σ_s is the largest Mises stress in three type of channels. From a thermodynamics perspective, the driving force for rafting is the partial derivative of the strain energy to the degree of rafting:

$$F = -\frac{\partial \psi}{\partial \xi} = c\frac{1+\upsilon}{3E}\sigma_s^2 \qquad (10)$$

In case of a uniaxial applied tensile stress in one of the three principals <001> directions

$$\sigma_s = |\sigma_0 + (1+\alpha)\sigma_i| \qquad (11)$$

This direction was selected since it leads to the highest von Mises stress values, which was taken to be the superimposition of extrinsic applied stress σ_0 and intrinsic lattice misfit stress σ_i, and σ_i was set as a constant value 300MPa for CMSX-4 superalloy. Similarly, the evolution of the rafting degree ξ is related to the actual morphology, the driving force and the temperature. Hence the channel width during rafting can be predicted with the following equation

$$\omega(t) = \omega_{cube}(t) + [\omega_{raft}(t) - \omega_{cube}(t)]$$
$$\left\{1 - \exp[-A'\sigma_s^{n'}\exp(-\frac{Q}{RT})t]\right\} \qquad (12)$$

In this model, the microstructure parameter γ channel width now is presented as a function of time, temperature and stress. In contrast to Fedelich's work, every parameter in this equation has a clear physical meaning.

6.2.3 The composition dependent microstructural model

In this work we also assume that the growth of microstructure periodicity follows the LSW theory but redefine the isotropic coarsening rate to present the proper effect of temperature. The isotropic coarsening rate of microstructure periodicity is shown in this equation

$$\lambda(t)^3 - \lambda_0^3 = Kt \qquad (13)$$

where t is the creep time. This equation resembles equation (8) but in contrast to the formulation of equation (8) our definition of K allows making a connecting to the equilibrium chemical composition of both the matrix and the precipitate as well as the diffusivities of the alloying elements.   Based on earlier work [25-28], the rate constant for the isotropic coarsening rate of precipitates is given by the following equation:

$$K = 8\gamma V_m^p / \sum_{i=1}^{n} \frac{9\left(x_i^p - x_i^{mp}\right)^2}{x_i^{mp} D_i / RT} \qquad (14)$$

In which $V_m{}^p$ is the molar volume of precipitate. x is equilibrium interface mole fraction of the γ′ forming elements on both matrix (m) and precipitate (p) sides. T is service temperature and D is corresponding diffusion coefficient. In the calculations, the interfacial energy is arbitrarily set at a fixed value of 0.3 J/m^2 irrespective of the precipitate size and the actual composition of precipitate and matrix[29]. This is a slight simplification but helps in illustrating the effect of alloy and particle composition on precipitate coarsening. All thermodynamic parameter values including x_i^p, x_i^{mp}, D_i and $V_m{}^p$ required during the calculations were calculated via Thermo-Calc using the latest TCNI8 and MobNI4 databases.

In addition to the coarsening rate, the misfit stress induced by the mismatch of lattice parameter and elasticity coefficient is also treated as a composition dependent parameter. In this work, the lattice misfit stress

is defined as σ_i, which is taken as the product of the Young's modulus and the lattice misfit strain, as shown in equation (15)

$$\sigma_\delta = |E\delta| \qquad (15)$$

$$\delta = \frac{2(a_{\gamma'} - a_\gamma)}{a_{\gamma'} + a_\gamma} \qquad (16)$$

The lattice misfit stress is determined by the element concentration in γ/γ' phases as well as the thermal expansion coefficients of both phases. In fact, apart from the internal stress induced by lattice misfit, the elastic misfit between γ/γ' phase contributes to internal stress as well. Dye's research [30] revealed that at temperatures above 1173K (900°C), the differences in the elastic moduli between γ/γ' phases in a CMSX-4 superalloy are within 5%. Therefore, in our work the internal stress is simplified as the lattice misfit stress only.

The evolution of channel width in CMSX-4 superalloy during rafting are presented in the following equation

$$\omega(t) = \omega_{cube}(t) \\ + [\omega_{raft}(t) - \omega_{cube}(t)]\Big\{1 \\ - \exp[-A'\sigma_s^{n'}\exp(-\frac{Q}{RT})t]\Big\} \qquad (17)$$

As mentioned before, the lattice misfit between γ/γ' phase is, on the one hand, governed by the chemical composition of the phases at the relevant temperature via Vegard's law and, on the other hand, by the thermal expansion coefficients of both phases. In this paper, the calculation of lattice misfit follows the method from Rettig[14]. The misfit is determined by the equation (18)-(21), which concern element concentrations of the respective phases at the required temperature.

$$a_\gamma^{RT} = 3.524 + 0.0196x_{Co}^\gamma + 0.110x_{Cr}^\gamma + 0.478x_{Mo}^\gamma + 0.444x_W^\gamma$$
$$+ 0.441x_{Re}^\gamma + 0.3125x_{Ru}^\gamma + 0.179x_{Al}^\gamma \qquad (\mathbf{18})$$
$$+ 0.422x_{Ti}^\gamma + 0.7x_{Ta}^\gamma$$

$$a_{\gamma\prime}^{RT} = 3.57 - 0.004x_{Cr}^{\gamma\prime} + 0.208x_{Mo}^{\gamma\prime} + 0.194x_W^{\gamma\prime}$$
$$+ 0.262x_{Re}^{\gamma\prime} + 0.1335x_{Ru}^{\gamma\prime} + 0.258x_{Ti}^{\gamma\prime} \qquad (\mathbf{19})$$
$$+ 0.5x_{Ta}^{\gamma\prime}$$

And

$$a_\gamma = a_\gamma^{RT} + 5.741 \times 10^{-5}\, T - 1.01 \times 10^{-9}\, T^2 \qquad (\mathbf{20})$$

$$a_{\gamma\prime} = a_{\gamma\prime}^{RT} + 6.162 \times 10^{-5}\, T - 1.132 \times 10^{-8}\, T^2 \qquad (\mathbf{21})$$

The element concentrations of γ/γ′ phases can be directly obtained from CALPHAD calculation and the simulated lattice misfit. In the absence of better data and reliable ab-initio calculations, the empirical equations (18)-(21) are used to calculate the lattice misfits.

Since the predictions of this model rely on the accuracy of the underlying database (as all thermodynamic calculations), we checked the validity of the database used in predicting the characteristics of Ni superalloys. Disagreements between experimental results and simulated volume fractions and chemical compositions of γ/γ′ phases have been reported when use was made of the formal TCNI databases[31, 32], but recent publications have validated the reliability of the current databases TCNI8[33, 34]. Modest deviations between the actual experimental data TCP phases and the recalculated values on the basis of the database have been reported by reference[35]. Hence the results of the thermodynamic calculations for TCP phases should be considered as indicative.

6.3 Results
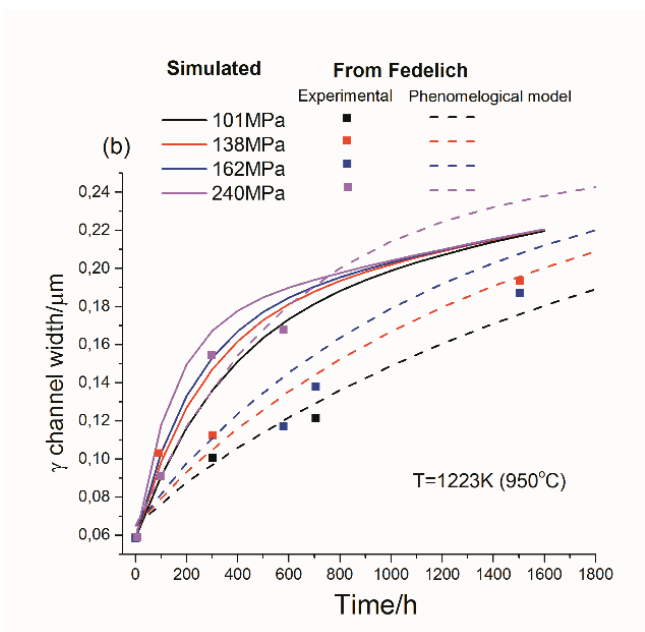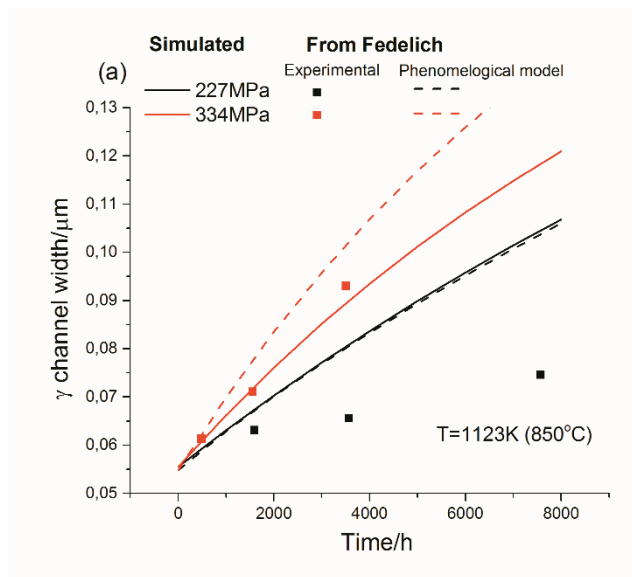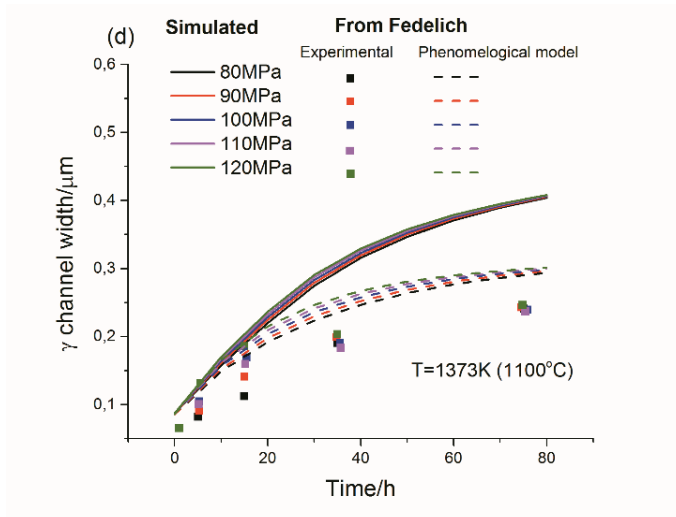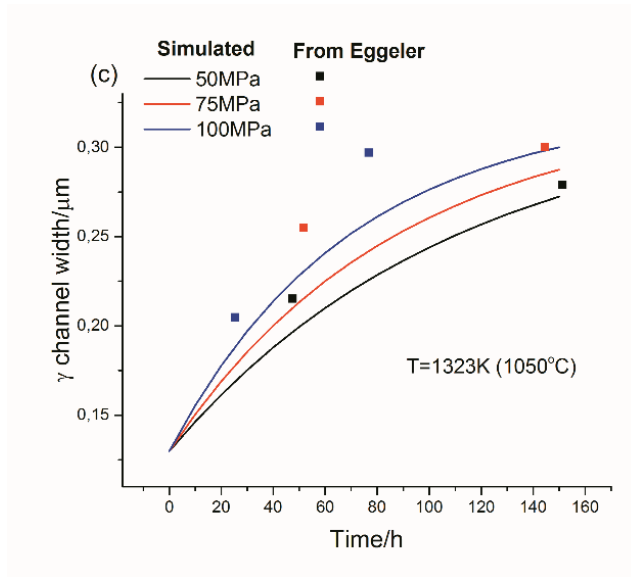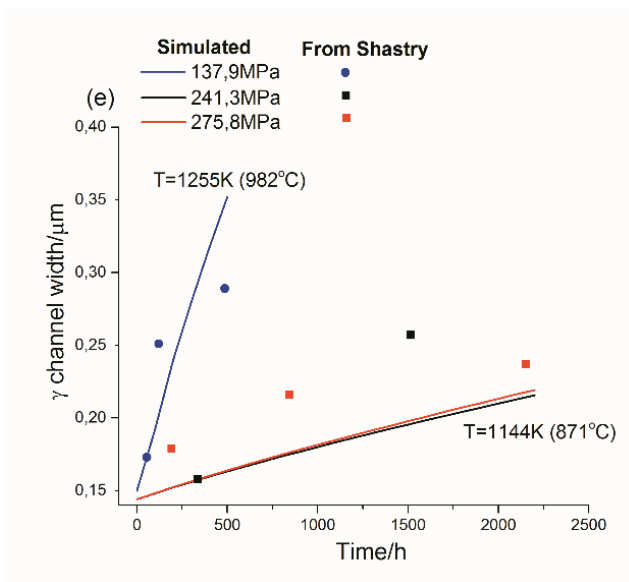
Figure 6.1 The comparison of calculated channel width of CMSX-4 superalloy with the experimental data from Fedelich and Eggeler at the temperature of 1173K (900°C) (a), 1273K (1000°C) (b), 1323K (1050°C) (c) and 1373K (1100°C) (d); and the comparison of René N4 microstructural parameters at 1144K (871°C) and 1255K (982°C) (e).

Figure 6.1 shows the simulated channel width of commercial alloys CMSX-4 and René N4 obtained from our model, and the comparison with the experimental data at different temperatures and applied stress levels. The solid lines are the simulation results obtained from our model while the dashed lines are the results from Fedelich's analytical expression (equation 7)). It turns out in figure 6.1a that at 1123K (850°C), at the lowest stress level a misfit exists between our predictions and the experimental data. But at high stress level, our model perfectly reproduces the experimental results and even outperform Fedelich's analytical expression. Figure 6.1b shows that at a service temperature of 1223K (950°C) a good agreement in the kinetics is obtained for the high stress 240MPa, while at lower stresses the kinetics of the channel

widening process is slightly overestimated. From figure 6.1c it can be deduced that our model predictions fit quite well with Eggeler's experimental data obtained at 1323K (1050°C)[36]. The results in figure 6.1d show that at 1373K (1100°C), the channel characteristics are also slightly overestimated by our simulation, but the tendency of convergence is well predicted. To validate our model for other compositions than that of CMSX-4, the evolution of γ channel width in Ni commercial grades René N4 as reported by Shastry[19] has been employed and the comparison with simulation results is shown in figure 6.1e. At a temperature of 1144K (871°C), the predictions are rather lower than the experimental observation, while at a higher temperature of 1255K (982°C), the prediction suits the experimental results perfectly. It is necessary to point out that for our model which has no fitting parameter in the calculation at all and only uses independently derived physical parameter values, the agreement in the of the predictions at diverse levels of temperature, stress as well as different compositions is remarkable. As such it is one of the first models that manages to couple the microstructure characteristics of rafting process with chemical composition-based thermodynamic calculation in Ni superalloys.

6.4 The effect of alloying element on microstructure and creep properties

For Ni superalloys, the microstructural features and their evolution during creep are intrinsically determined by the type and concentration of the various alloying elements. For example, Al and Ta are the main γ′ forming elements, and higher levels of these elements can effectively increase the γ′ volume fraction[37]. Mo and Co partition preferentially in γ matrix and plays as a strong solid solution strengthening element to elevate the creep properties[38-40], while Co addition helps to reduce the tendency to form Topologically-closed packed (TCP) phases[41, 42].

Cr was found to increase γ' volume fraction[38] but deteriorates the microstructure stability at high level of concentration[43]. The Re addition can substantially lower the γ' coarsening kinetics and helps to bring into large negative misfits, but also increases the tendency to form Re-rich TCP phases[44, 45]. Ru can effectively stabilize the microstructure by suppressing the precipitation of TCP phases[34, 46].

We now try and predict the effect of the concentration of specific alloying elements on the microstructure and rafting kinetics, taking the base composition of CMSX-4 superalloy as the starting point. The change in alloy composition is obtained at the expense of varying Ni concentration. The service temperature, total time and applied stress are set as 1273K (1000 ^{0}C), 200 h and 100 MPa respectively, and the predicted trends are compared with the experimental observations reported in the literature. All alloying concentrations are given in wt.%.

6.4.1 Cr effect

The predicted effects of Cr on the microstructure parameters and γ' coarsening rate are shown in figure 6.2. The calculation results show that as the Cr concentration increase, the value of γ channel width varies but the changes are minor. The γ' coarsening rate decreases slightly when the Cr levels increase from 2% to 10%, then the decrease becomes sharper as Cr increases from 10% to 14%. The γ' volume fraction decreases slowly but continuously with the Cr level. When the Cr level reaches 11%, the TCP phases including μ phase and σ phase are predicted to start to precipitate.

The predicted influence of the Cr level on the volume fraction is in good agreement with the experimental observations by Mackay's[40] and Feng's[13], which showed that Cr helps to develop the γ' volume fraction in Ni superalloy. Feng's data also indicates that a Cr addition

contributes to narrowing the γ channel width, which also agrees well with the predictions. Carroll's[37] and Chen's[47] investigations show that an increasing Cr level helps to improve the creep strength of Ni superalloys. This result can be explained by the effect of Cr on decreasing γ′ coarsening rate as shown in this figure. Besides, it also has been reported [12, 13] that high Cr levels can deteriorate the microstructure stability by increasing the proneness to TCP phases formation, in accordance with the simulation results reflected by the pink dots. In this figure, the backward slash patterns define areas where undesirable phases precipitate. From the simulations as presented in figure 6.2 and assuming the thermodynamic database to be sufficiently validated and correct (see the validity comment at the end of the model introduction section), it can be concluded that the Cr level can be increased in the base CMSX-4 alloy, to further retard the coarsening rate without the occurrence of TCP phases formation.
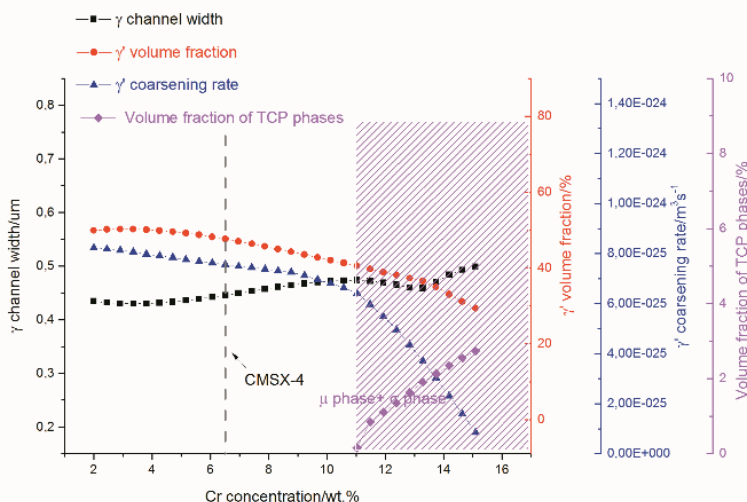
Figure 6.2 The effect of Cr on the γ channel width, γ′ volume fraction and γ′ coarsening rate. The dashed region marks the formation of undesirable phases.

6.4.2 Co effect
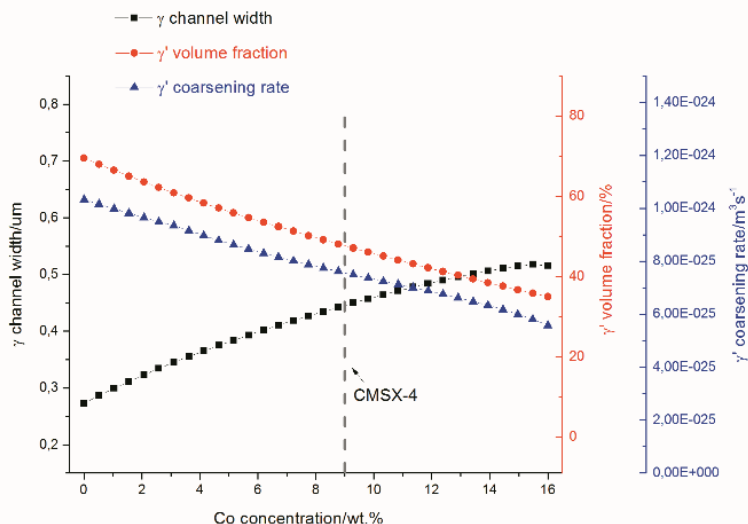
Figure 6.3 The effect of Co on the γ channel width, γ′ volume fraction and γ′ coarsening rate.

As shown in figure 6.3, a rise in Co level from 0 to 16 wt.% brings a continuous increase in γ channel width and a continuous drop in γ′ volume fraction from 71% to 48%, while the γ′ coarsening rate decreases simultaneously. Over the whole Co concentration range, no signs of the existence of TCP phases is found, which agrees well with the experimental investigations[43] showing that Co addition helps to suppress the formation of TCP phases. The predicted effect of Co on decreasing the γ′ volume fraction fits well with Mackay's investigation[40, 48]. In contrast, Feng's[13] experimental results show that an 8 wt.% addition of Co can slightly reduce γ′ volume fraction to 3%. This mismatch reflects the complex effect of Co on γ′ precipitation, which can be ascribed to the effect of Co on altering the γ/γ′ partitioning behaviour of other alloying elements[49].

6.4.3 Ta effect
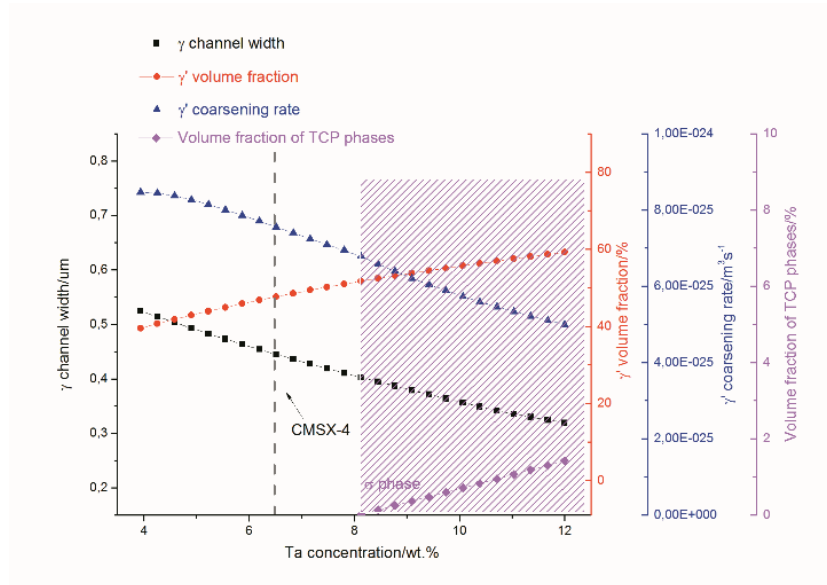
Figure 6.4 The effect of Ta on the γ channel width, γ′ volume fraction and γ′ coarsening rate. The dashed region marks the formation of undesirable phases.

The effect of Ta on the microstructural parameters of γ/γ′ phases is shown in figure 6.4. The calculated results show that if the Ta concentration increases from 4% to 12%, the value of γ channel width is almost halved, while the γ′ volume fraction increases continuously from 39% to 60%, and the γ′ coarsening rate has a sustained decrease. The simulated results agree well with Jena's experimental investigations showing that Ta promotes γ′ formation as a γ′ former[50], and Forde's study showing that Ta addition helps to retard diffusion mediated processes in Nickel based systems [51]. When the Ta content reaches 8.1%, Cr-enriched σ phase begins to precipitate, as shown by pink dot and the area marked by the slash pattern. It has been demonstrated by Karunaratne's experimental results that the Ta addition increases the susceptibility to TCP formation by concentrating the γ–partitioning

TCP-forming elements in γ phase[52]; Specifically, Booth-Morrison's study shows that Ta increases the partitioning ratio for Cr by displacing Cr atoms from γ′ phase[53], in this way promoting the TCP formation. The reported experimental observations are well predicted by the model presented here.

6.4.4 Mo effect
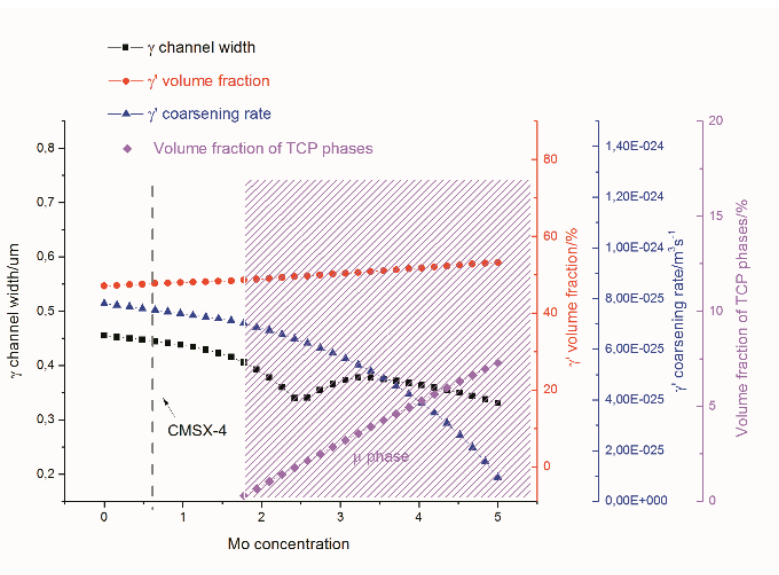
Figure 6.5 The effect of Mo on the γ channel width, γ′ volume fraction and γ′ coarsening rate. The dashed region marks the formation of undesirable phases

Figure 6.5 shows that the γ channel width drops from 0.45μm to 0.32μm as the Mo concentration increases from 0 to 2.5 wt.%. After that the channel width experiences a slow increase then keeps decreasing with further increase in Mo concentration. Besides, the figure shows that Mo additions can slightly increase the volume fraction of γ′ precipitates, and reduces the γ′ coarsening rate by a factor 8 when the Mo concentration

rises from 0 to 5%. However, the undesirable µ phase begins to precipitate and grow rapidly for Mo concentrations in excess of 1.7%. The simulation results for the γ channel width and γ′ volume fraction fit well with Feng's data[13], which showed that 1.5% addition of Mo can slightly increase the precipitation volume fraction and decrease the γ channel width. Moreover, Biss's experimental results[54] show that Mo addition can retard the coarsening rate of γ′ particles also agrees well with the calculated results. The role of Mo as a strong TCP former has been investigated experimentally by many researchers [11, 12], and their results confirm the simulation results that an elevated level of Mo promotes the formation of the detrimental µ phase. The forbidden area with the presence of µ phase is marked by a backward slash pattern. It is also worth mentioning here that the model predictions suggest that there still exist some space to increase the Mo concentration in the base CMSX-4 alloy, as it leads to a higher precipitation volume fraction and a lower coarsening rate while the TCP phases should remain absent.

6.4.5 Re effect

Finally, figure 6.6 shows that according to the simulations based on the existing data in the TCNI8 and MobNI4 thermodynamic databases Re additions can slightly decrease the γ channel width, while the γ′ volume fraction remains more or less unchanged. The blue dots indicate that the coarsening rate of γ′ precipitates experiences a slow decrease when the Re level increases from 1% to 5%. Besides, TCP phases are predicted not to form over the whole concentration range of Re from 1% to 5%. According to the experimental results by Singer and his co-workers[44], a 2% at.% Re addition can significantly reduce the γ′ volume fraction to 15%. Besides, the effect of Re on the coarsening rate of γ′ has also been investigated extensively. The conclusions are quite consistent and indicate that Re addition in Ni superalloys can effectively retard the

γ′ coarsening rates [55, 56], due to the fact that Re is the slowest-diffusing element in Nickel among all alloy elements [57, 58]. The calculated results are in qualitative agreement with the reported effect of Re, but the high efficiency of Re in lowering the coarsening rate as well as decreasing γ′ volume fraction is quantitatively not captured very well. It might be that the data in the thermodynamic databases TCNI8 and MobNI4 regarding the impact of the element Re need some adjustment.
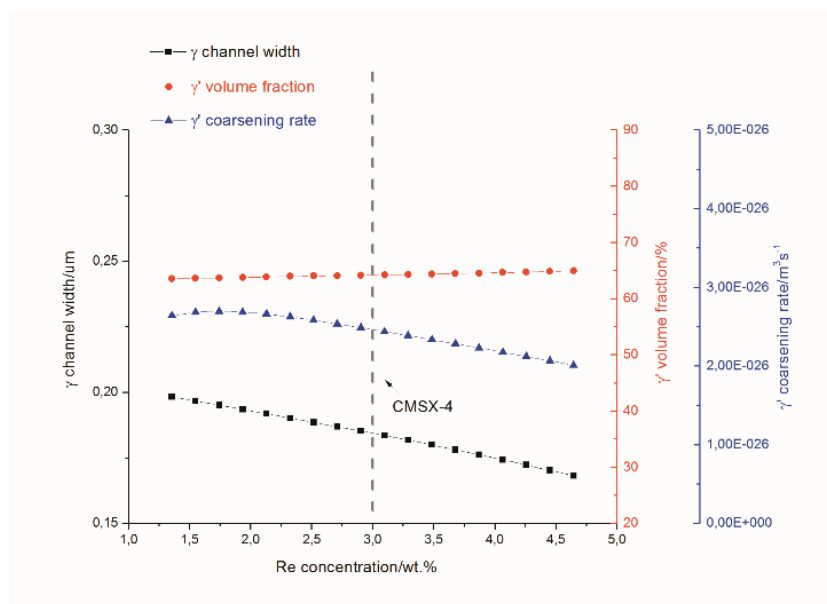
Figure 6.6 The effect of Re on the γ channel width, γ′ volume fraction and γ′ coarsening rate.

To sum up, our model can semi-quantitatively predict the effect of chemical composition of Ni based superalloys on γ channel width at relatively high temperature and low stress range on the basis of hard physical data rather than empirical fitted parameter values, which reflects the power of the model in simulating the microstructure evolutions during rafting process. The effect of alloying elements Cr, Co, Ta, Mo and Re in CMSX-4 superalloy on the microstructure

parameters, γ' coarsening rates and microstructure stability are calculated by this model, and the simulated results have a qualitatively good agreement with the experimental results from literature. Moreover, our calculation shows that the chemical composition of the CMSX-4 superalloy has not reached the optimal values from a thermomechanical stability perspective. There still exist some space to increase the alloying level of Cr, Ta and Mo to further improve the precipitation strengthening while maintaining the microstructural stability of the matrix.

6.5 Conclusions

1. A novel computational model for the microstructural stability of Ni based single crystal superalloys as a function of temperature and applied tensile stress has been built by combining thermodynamics calculations and an energy-based microstructural model. The connection between chemical compositions and the rate of microstructure evolution is based on the isotropic coarsening of γ' phase and γ/γ' lattice misfit during creep.

2. The model has been applied to predict the γ channel widening of Ni commercial grades of CMSX-4. The microstructure characteristics of rafting process, especially at elevated temperature, can be well simulated by the model.

3. The effect of alloying elements Cr, Co, Mo and Re on the microstructural parameters, γ' coarsening rates and microstructure stability in CMSX-4 superalloy have been analysed by this model. The simulated results are well confirmed by the reported experimental data. The calculated results show that from a thermomechanical stability point of view the chemical composition of the CMSX-4 superalloy has not reached its optimal value. There still exist some space to increase the

alloying level of Cr, Ta and Mo, to further improve the precipitation strengthening while maintaining the microstructural stability of the matrix.

Reference

[1]   Reed RC. The superalloys: fundamentals and applications: Cambridge university press, 2008.

[2]   Zhu Z, Basoalto H, Warnken N, Reed R. Acta Mater 2012;60:4888.

[3]   Gao S, Fivel M, Ma A, Hartmaier A. J Mech Phys Solids 2017;102:209.

[4]   Vorontsov V, Voskoboinikov R, Rae CM. Prediction of Mechanical Behaviour in Ni-Base Superalloys Using the Phase Field Model of Dislocations. Advanced Materials Research, vol. 278: Trans Tech Publ, 2011. p.150.

[5]   Cottura M, Appolaire B, Finel A, Le Bouar Y. J Mech Phys Solids 2016;94:473.

[6]   Choi YS, Parthasarathy TA, Woodward C, Dimiduk DM, Uchic MD. Metall Mater Trans A 2012;43:1861.

[7]   Nabarro F, Cress CM, Kotschy P. Acta Mater 1996;44:3189.

[8]   Ohashi T, Hidaka K, Imano S. Acta Mater 1997;45:1801.

[9]   Chang JC, Allen SM. J Mater Res 1991;6:1843.

[10]   Wu W-P, Guo Y-F, Dui G-S, Wang Y-S. Comp Mater Sci 2008;44:259.

[11]   Liu XG, Wang L, Lou LH, Zhang J. J Mater Sci Technol 2015;31:143.

[12]   Wang B, Zhang J, Huang T, Su H, Li Z, Liu L, Fu H. J Mater Res 2016;31:3381.

[13]   Huo JJ, Shi QY, Feng Q. Mater Sci Eng A 2017;693:136.

[14]   Rettig R, Ritter NC, Helmer HE, Neumeier S, Singer RF. Model Simul Mater Sci 2015;23:035004.

[15]   Reed R, Tao T, Warnken N. Acta Mater 2009;57:5898.

[16] Epishin A, Link T, Klingelhöffer H, Fedelich B, Brückner U, Portella PD. Mater Sci Eng A 2009;510:262.

[17] Scholz A, Wang Y, Linn S, Berger C, Znajda R. Mater Sci Eng A 2009;510:278.

[18] Epishin A, Link T, Nazmy M, Staubli M, Klingelhoffer H, Nolze G. Superalloys 2008 2008:725.

[19] Shastry CG, Kelekanjeri VSG, Vishwanath T, Chaudhuri S. Mater Sci Eng A 2013;585:47.

[20] Fedelich B, Künecke G, Epishin A, Link T, Portella P. Mater Sci Eng A 2009;510-511:273.

[21] Fedelich B, Epishin A, Link T, Klingelhöffer H, Künecke G, Portella PD. Rafting during high temperature deformation in a single crystal superalloy: experiments and modeling. Superalloys 2012. TMS, 2012. p.491.

[22] Fan Y-N, Shi H-J, Qiu W-H. Mater Sci Eng A 2015;644:225.

[23] Gong J, Snyder D, Kozmel T, Kern C, Saal JE, Berglund I, Sebastian J, Olson G. JOM 2017:1.

[24] Ai C, Zhao X, Zhou J, Zhang H, Liu L, Pei Y, Li S, Gong S. J Alloy Compd 2015;632:558.

[25] Lu Q, Xu W, van der Zwaag S. Philos Mag 2013;93:3391.

[26] Lu Q, Xu W, van der Zwaag S. Comp Mater Sci 2014;84:198.

[27] Lu Q, Xu W, van der Zwaag S. Acta Mater 2014;77:310.

[28] Lu Q, Xu W, van der Zwaag S. Acta Mater 2014;64:133.

[29] Yang X, Hu W, Zhang X. Appl Surf Sci 2013;264:563.

[30] Dye D, Coakley J, Vorontsov V, Stone H, Rogge R. Scr Mater 2009;61:109.

[31] Amouyal Y, Mao Z, Seidman DN. Acta Mater 2010;58:5898.

[32] Palumbo M, Baldissin D, Battezzati L, Tassa O, Wunderlich R, Fecht HJ, Brooks R, Mills K. Thermodynamic properties of CMSX-4 superalloy: Results from the Thermolab project. Mater Sci Forum, vol. 508: Trans Tech Publ, 2006. p.591.

[33] Llewelyn SCH, Christofidou KA, Araullo-Peters VJ, Jones NG, Hardy MC, Marquis EA, Stone HJ. Acta Mater 2017;131:296.

[34] Matuszewski K, Müller A, Ritter N, Rettig R, Kurzydłowski KJ, Singer RF. Adv Eng Mater 2015;17:1127.

[35] Matuszewski K, Rettig R, Matysiak H, Peng Z, Povstugar I, Choi P, Müller J, Raabe D, Spiecker E, Kurzydłowski KJ, Singer RF. Acta Mater 2015;95:274.

[36] Serin K, Göbenli G, Eggeler G. Mater Sci Eng A 2004;387:133.

[37]   Carroll L, Feng Q, Pollock T. Metall Mater Trans A 2008;39:1290.

[38]   MacKay RA, Gabb TP, Garg A, Rogers RB, Nathal MV. Compositional Effects on Nickel-base Superalloy Single Crystal Microstructures. NASA Glenn Research Center; Cleveland, OH, United States, 2012.

[39]   Zhang J, Murakumo T, Harada H, Koizumi Y. Scr Mater 2003;48:287.

[40]   MacKay R, Gabb T, Garg A, Rogers R, Nathal M. Mater Charact 2012;70:83.

[41]   Erickson G. The development and application of CMSX-10. Superalloys 1996. TMS, 1996. p.35.

[42]   Walston W, O'Hara K, Ross E, Pollock T, Murphy W. Rene N6: Third Generation Single Crystal Superalloy. Superalloys 1996. TMS, 1996. p.27.

[43]   Rae CM, Reed RC. Acta Mater 2001;49:4113.

[44]   Heckl A, Neumeier S, Göken M, Singer RF. Mater Sci Eng A 2011;528:3435.

[45]   Caron P, Khan T. Aerosp Sci Technol 1999;3:513.

[46]   Matuszewski K, Rettig R, Singer RF. The effect of Ru on precipitation of topologically close packed phases in Re–containing Ni base superalloys: Quantitative FIB-SEM investigation and 3D image modeling. MATEC Web of Conferences, vol. 14: EDP Sciences, 2014. p.09001.

[47]   Chen JY, Feng Q, Cao LM, Sun ZQ. Mater Sci Eng A 2011;528:3791.

[48]   Nathal M, Ebert L. Metallurgical Transactions A 1985;16:1849.

[49]   Dreshfield RL, Thomas KJ. Analyses of Elemental Partitioning in Advanced Nickel-Base Superalloy Single Crystals. NASA Glenn Research Center; Cleveland, OH, United States, 2005.

[50]   Jena A, Chaturvedi M. J Mater Sci 1984;19:3121.

[51]   Forde PT. Adv Mater Process 1996;149.

[52]   Karunaratne MS, Rae CM, Reed R. Metall Mater Trans A 2001;32:2409.

[53]   Booth-Morrison C, Mao Z, Noebe RD, Seidman DN. Appl Phys Lett 2008;93:033103.

[54]   Biss V, Sponseller D. Metall Trans 1973;4:1953.

[55]   Giamei A, Anton D. Metall Trans A 1985;16:1997.

[56]   Yoon KE, Noebe RD, Seidman DN. Acta Mater 2007;55:1159.

[57]   Fu CL, Reed R, Janotti A, Krcmar M. On the diffusion of alloying elements in the nickel-base superalloys. Superalloys 2004, vol. 2004. TMS, 2004. p.867.

[58]   Janotti A, Krčmar M, Fu CL, Reed RC. Phys Rev Lett 2004;92:085901.

Summary

The development in computational simulation techniques has brought significant progress in the realization of computational alloy design. The advantages are most significant when developing novel materials of which the research & development cycles are particularly time and energy (and hence cost) consuming, such as high-temperature alloys. In our former research, a computational alloy design approach coupling thermodynamics, kinetics, metal physics and genetic algorithm has been developed. By applying this new approach, novel heat resistant steels have been successfully designed with different microstructural features, which manage to nicely outperform existing commercial alloys. In this thesis, we follow the same approach while more focus has been given on adjusting the alloying level of different elements to solve specific issues, such as the high cost issue caused by a high Cobalt level, and the high microstructural instability caused by a high Chromium concentration. Extended application has been made to design novel heat resistant steels by introducing the concept of self-healing mechanisms. The creep damage (grain boundary cavities) of newly-developed steels during service are expected to be automatically filled by the special-designed Laves phase of which their formation kinetics was adjusted.

Moreover, attempts have been made to apply this computational approach to simulate the properties of Ni base single crystal superalloys. In the important service domain characterised by a high temperature (>950 ^{0}C) and a low stress (<200 MPa), the creep properties of Ni superalloys are intrinsically determined by the evolutions of microstructural variation and dislocation behaviour. In this work a bridge has been made between the simulated kinetics of these processes with the chemical concentration of the superalloys.

In Chapter 2, we focus on the newly designed martensitic creep resistant steels strengthened by Laves phase and $M_{23}C_6$ carbides, The excellent performance of these novel alloys have been analysed and rationalised while attempts have been made to reduce the level of Cobalt (while keeping the properties the same) in order to lower the alloying costs. Computational results have shown that the newly designed alloys with a

high Co level indeed remarkably outperform the existing alloys at a service temperature of 650°C. The outstanding performance can be attributed to the good combination of precipitation characteristics such as the high volume fractions, the low coarsening rates and the high precipitation strengthening factor. The analysis of the effect of Co on the precipitation of Laves phase and $M_{23}C_6$ suggests that as the Co concentration decreases, the precipitation strengthening contributions in these systems will inevitably degrade, even considering the complex synergies of all alloying elements. In the case of Laves phase strengthened martensitic steels the calculations predict that Co can be partially replaced by W to yield the same precipitation strengthening level, while in $M_{23}C_6$ strengthened martensitic steels the long-term strength level cannot be tailored by adjustment of the Cr level but depend on the Co level only.

For the existing commercial heat resistant steels, one general problem in their industrial application is the conflict between the corrosion/ oxidation resistance and the long-term microstructural stability. A high Cr alloying level is necessary to guarantee the high temperature corrosion resistance, while on the other hand a high Cr content can strongly promote the degradation of the MX strengthening precipitates and transform them into detrimental Z phase. In Chapter 3, thermodynamic and kinetic calculations have been made to simulate the formation mechanism of Z phase, and attempts have been made to solve this "Z phase problem". Various commercial heat resistant steels with different Cr levels have been analysed, with their precipitation hardening and solid solution strengthening effects being calculated at 650^{0}C. The calculated creep properties have been compared with the experimental creep strength values and the results confirm that calculated precipitation strengthening factor reflects the experimental creep life time rankings, related to the formation of the Z-phase rather well. By exploring the effects of two dominant alloying elements Cr and C on Z-phase formation, it was found not possible to come up with compositional adjustments leading to a combination of a high Cr level (12-15 %Cr) and

a reduced tendency to form Z-phase precipitates, while meeting all necessary requirements for a desirable microstructure.

The self-healing concept now has opened up a new window for creep steel development. In Chapter 4, novel creep resistant steels have been computationally developed starting from our base alloy-by-design model and introducing the self-healing mechanism. We focus on simulating the formation kinetics of the self-healing agent (in this case the Laves phase) in the iron matrix. To quantify the self-healing potential, an empirical relationship is derived which captures the experimental incubation time for Laves phase formation in existing commercial alloys on the basis of the calculated chemical driving force for that alloy composition. The compatibility of self-healing properties and mechanical properties were evaluated. A series of novel alloys with kinetically different self-healing behaviour but comparable mechanical properties have been proposed. Additional calculations were made to analyse the compositional domain for self-healing at temperatures higher than 550°C. The results show a significant reduction in the potential compositional options.

The simulation work has been extended into the field of Ni superalloys in Chapter 5. The high performance of Ni single crystal superalloys during high-temperature, low-stress creep service, is primarily controlled by the combined effects of microstructural evolution (the formation of rafting lamellae), and the dislocation behaviour (the well-arranged dislocation network located on the γ/γ' interface). The simulation work focussed on the secondary creep stage which takes longest time of creep life, during which two main recovery mechanism based on dislocation migration dominate the process. One is super - dislocations shearing into γ' rafts through a two - super-partials - assisted approach. Another is the migration of compact dislocations along γ/γ' interface. These two mechanisms are similarly climb-rate-controlled process. A model for the minimum creep rate based on thermodynamic and kinetic calculations and using an existing detailed dislocation dynamics model has been built by taking the dislocation migration behaviours as well as the rafted

microstructure into consideration, which can well reproduce the creep properties of existing Ni superalloy grades.

In Chapter 6, a novel computational model for the microstructural stability of Ni based single crystal superalloys as a function of temperature and applied tensile stress has been built by combining thermodynamics calculations and an energy-based microstructural model. The connection between chemical compositions and the rate of microstructure evolution is based on the isotropic coarsening of γ' phase and γ/γ' lattice misfit during creep. The model has been applied to predict the γ channel widening of Ni commercial grades of CMSX-4. The microstructure characteristics of rafting process, especially at elevated temperature, can be well simulated. The effects of the alloying elements Cr, Co, Mo and Re on the microstructural parameters, γ' coarsening rates and microstructure stability in CMSX-4 superalloy have been analysed by this model. The simulated results are well confirmed by the reported experimental data. The calculated results show that from a thermomechanical stability point of view the chemical composition of the CMSX-4 superalloy has not reached its optimal value. There still exist some space to increase the alloying level of Cr, Ta and Mo to further improve the precipitation strengthening while maintaining the microstructural stability of the matrix.

Samenvatting

De ontwikkelingen in het gebied van computer simulaties hebben geleid tot een duidelijke versnelling van model gedreven legeringsontwikkeling. De voordelen zijn het grootst voor die staalsoorten en andere legeringen waarbij de onderzoeks- en ontwikkelingskosten zeer hoog zijn, en dat geldt zeker voor nieuwe staalsoorten voor hoge temperatuurgebruik en superlegeringen. In het voorafgaande onderzoek hebben we een methode ontwikkeld waarbij thermodynamica, -kinetiek, metaalfysica en een genetisch algoritme gekoppeld worden om tot voorspelling van een optimale samenstelling te komen op basis van gekwantificeerde microstructuurparameters. Op basis van dit model hebben we nieuwe staalsamenstellingen geïdentificeerd die duidelijk betere eigenschappen dan de bestaande kruip-staalsoorten moeten hebben. In dit proefschrift is deze onderzoekslijn voortgezet maar is de aandacht verlegd naar het oplossen van specifieke problemen, zoals een hoge kostprijs door het gebruik van het dure element Cobalt en de beperkte thermische stabiliteit van staalsoorten met een hoog Chroom gehalte. Daarnaast is het model uitgebreid met nieuwe concepten om de optimale samenstelling van toekomstige zelf-herstellende staalsoorten te kunnen berekenen. Speciale aandacht is besteed aan het doen verdwijnen van kruipschade (met name korrelgrensporositeit) door lokale uitscheiding van de Laves fase.

Tevens is onderzoek gedaan naar de optimalisatie van de samenstelling van Ni-gebaseerde superlegeringen voor gebruik bij hoge temperatuur ($>950\ ^{0}C$) en lagere belastingen (<200 MPa). Onder die condities wordt de levensduur bepaald door de gekoppelde veranderingen in de microstructuur en de dislocatiestructuur. We zijn er in geslaagd een verbinding te maken tussen de kinetiek van beide processen en de chemische samenstelling.

In Hoofdstuk 2 richten we ons onderzoek op nieuw ontwikkelde Lavesfase en $M_{23}C_6$ carbide-houdende martensitische kruipstalen en de mogelijkheden in kaart gebracht om de kostprijs ervan te verlagen door het gehalte aan het dure element Cobalt te reduceren. De analyse liet zien dat als het Cobalt gehalte verlaagd wordt de sterkte van de legering

onvermijdelijk afneemt, ook al wordt optimaal gebruik gemaakt van synergistische effecten tussen alle andere legeringselementen. In het geval van Laves fase versterkte legeringen zou de Co gedeeltelijk vervangen kunnen worden door W zonder verlies van eigenschappen. In het geval van $M_{23}C_6$ carbide-houdende staalsoorten bleek het onmogelijk het Co gehalte aan te passen zonder verlies van kruipsterkte.

Voor bestaande commerciële hoge temperatuur staalsoorten is het bekend dat er een spanningsveld bestaat tussen de corrosie-/oxidatievastheid en de thermische stabiliteit van de microstructuur. Een hoog chroom gehalte is gunstig voor een goede corrosie-/oxidatieweerstand, maar een hoog chroom gehalte bevordert ook de vorming van ongewenste Z-fase uitscheidingen uit de versterkende MX precipitaten. In Hoofdstuk 3 worden thermodynamische en -kinetische berekeningen gepresenteerd om de vorming van Z-fase uitscheidingen te beschrijven en zo mogelijk het 'Z-fase probleem' op te lossen. Hiertoe is het fasegedrag van diverse commerciële kruipstalen tijdens verblijf op 650 ^{0}C geanalyseerd en werd er een duidelijke correlatie tussen de kruiplevensduur en de vorming van Z-fase vastgesteld. Uit de berekeningen (met name de analyse van het effect van Cr en C gehalte) blijkt dat het onmogelijk is de samenstelling zo te kiezen dat de gewenste combinatie van een hoog chroom gehalte en een geringe tendens om Z-fase te vormen verkregen wordt.

Het 'self healing' concept biedt nieuwe mogelijkheden voor de verdere ontwikkelingen van kruipstaal. In Hoofdstuk 4 wordt het eerdere optimalisatiemodel uitgebreid met een module waarin het zelf-herstellend gedrag in rekening gebracht wordt. Het model richt zich op de gecontroleerde vorming van Laves fase in de poriën die zich tijdens kruip belasting op termijn op de korrelgrenzen vormen. Om in het model het moment van het begin van het optreden van de 'self healing' reactie te kunnen kwantificeren is een empirische relatie tussen de incubatietijd voor Laves fase vorming en de thermodynamische drijvende kracht bepaald. Het model is gebruikt om nieuwe staal-samenstellingen met belangrijke verschillen in kinetiek van schadeherstel maar verder

vergelijkbare mechanische eigenschappen te berekenen welke inzet zijn geworden voor een experimentele validatie. Aanvullende berekeningen zijn uitgevoerd om de mogelijke (zelf-herstellende) staalsamenstelling, in geval van gebruik bij hogere temperaturen dan 550 ^{0}C, in kaart te brengen. De berekeningen laten zien dat de reeks van interessante samenstellingsopties sterk afneemt bij hogere gebruikstemperaturen.

In Hoofdstuk 5 is het onderzoek uitgebreid in de richting van Ni-gebaseerde superlegeringen. Het gedrag van deze superlegeringen wordt bepaald door de simultane veranderingen in de microstructuur ('rafting') en de dislocatiestructuur (een uitgelijnde dislocatienetwerk op het γ/γ' grensvlak). Tijdens de 'stage 2' fase van het kruipproces zijn er twee vergelijkbare vervormingsprocessen: het glijden superdislocaties door de γ' platen en het glijden van compacte dislocaties langs het γ/γ' grensvlak. In dit hoofdstuk wordt een bestaand dislocatie dynamica model gekoppeld aan het model van de microstructuur ontwikkelingen. Het model blijkt het mechanisch gedrag zoals beschreven in de literatuur goed te beschrijven.

In Hoofdstuk 6 wordt een nieuw model gepresenteerd voor de stabiliteit van de microstructuur van Ni-gebaseerde superlegering als een functie van de temperatuur en de aangelegde spanning. Het model combineert thermodynamica en een energie-gebaseerd microstructuur model. De koppeling tussen de chemische samenstelling en de snelheid van structuurverandering is gebaseerd op de isotrope vergroving van de γ' fase en de misfit in roosterconstantes op het γ/γ' grensvlak. Het model is met succes toegepast op data voor de CMSX-4 superlegeringen. Het model is daarna toegepast om de effecten van de legeringselementen Cr, Co, Mo en Re op de stabiliteit van de microstructuur te analyseren. De berekeningen geven aan dat de huidige samenstelling van CMSX-4 superlegeringen nog niet optimaal is en dat een hogere sterktes bij gelijkblijvende thermische stabiliteit mogelijk zijn door kleine aanpassingen in de Cr, Ta en Mo concentraties.

Acknowledgement

The PhD experience is always a unique journey for all experiencers or quitters. Without the support and help from many fantastic people, I might not be lucky enough to become a survivor after this four-year trip. Therefore I would like to express my sincerely gratitude to these names.

Firstly I would like to sincerely thank my promotor, Sybrand van der Zwaag. He himself is a realistic idea generator, an effective problem solver and an experienced educator. Under his supervision, I can have enough freedom to explore the fields interest me meanwhile keep the track with the essential logic core in the right way. I really enjoy the fruitful discussion and delightful advices from you, not only in the academic research, but also on my daily life. You are the academic idol to me, and taught me what a real scientist looks like. I will definitely keep the slogan of our group in my mind and do my best to become famous and rich.

The deep thanks to my copromotor, Wei Xu. You are always optimistic and energetic with great passion on academia. We had skype meeting or wechat meeting not that regularly, but you can always spare time to have a discussion even when you are in the airport or at train station. Without your support and help, my work cannot be completed smoothly as planned.

I would also like to express my gratitude to Prof. dr. Annika Borgenstam at KTH Royal Institute of Technology, Sweden, Prof. dr. Ulrich Krupp at RWTH Aachen University, Germany, Prof. dr. ir. Roumen H. Petrov at Ghent University, Belgium, Dr. ir. Neils H. van Dijk, Dr. ir. Wim G. Sloof, and Prof. dr. Ekkes H. Brück at Technische Universiteit Delft, for being the committee members of my PhD defence.

Curriculum Vitae

Hao Yu

Born on May 28th, 1991

Tai'an, ShanDong Province, China

2015.9 – 2019.12

PhD candidate

Group of Novel Aerospace Materials, Faculty of Aerospace Engineering, Delft University of Technology, the Netherlands.

Promotors: Prof. Sybrand van der Zwaag and Prof. Wei Xu

2012.9 - 2015.6

Master of Material Physics and Chemistry

Materials Design Group, School of Material Science and Engineering, Dalian University of Technology, China.

Supervisor: Prof. Chuang Dong

2008.9 - 2012.6

Bachelor of Material Physics

School of Material Science and Engineering, Dalian University of Technology, China.

List of Publications

Referred Publications

- **H. Yu**, W. Xu, S. van der Zwaag, On the Cobalt - Tungsten / Chromium Balance in Martensitic Creep Resistant Steels, *Steel Res Int* 89(2) (2018)1700320.

- **H. Yu**, W. Xu, S. Van Der Zwaag, The Compositional Dependence of the Microstructure and Properties of CMSX-4 Superalloys, *Metall Mater Trans A* 49(1) (2018) 406.

- **H. Yu**, W. Xu, S. van der Zwaag, On the Relationship between the Chromium Concentration, the Z–Phase Formation and the Creep Strength of Ferritic - Martensitic Steels, *Steel Res Int* 89(2018)1800177.

- **H. Yu**, W. Xu, S. van der Zwaag, Connecting the Microstructure Stability of Ni Based Superalloys to Their Chemical Compositions, *Mater Sci Forum, Trans Tech Publ* (2018) 967.

- **H. Yu**, W. Xu, S. van der Zwaag, Microstructure and dislocation structure evolution during creep life of Ni-based single crystal superalloys. *J Mater Sci Technol*, Accepted

- **H. Yu**, W. Xu, S. van der Zwaag, On the compositional design of self-healing creep resistant steels based on Laves Phase filling of grain boundary cavities. In preparation.

- **H. Yu,** J. Wang, C. Dong, et al, Effect of Brazing Temperature on Properties of W/CuCrZr Alloy Joints Brazed with Cu-based Amorphous Brazing Filler, *Rare Metal Mater Eng* 45(11) (2016) 2981. (In Chinese)

Conference Presentations

- **H. Yu** et al, The Compositional Dependence of the Microstructure and Properties of CMSX-4 Superalloys; Oral presentation, 4th ECCC Conference 2017, Dusseldorf, Germany
- **H. Yu** et al, On the Cobalt− Tungsten/Chromium Balance in Martensitic Creep Resistant Steels, Poster presentation, Euromat 2018, Thessaloniki, Greece
- **H. Yu** et al, Connecting the Microstructure Stability of Ni Based Superalloys to their Chemical Compositions; Poster presentation, Thermec 2018, Paris, France
- **H. Yu** et al, A high temperature creep model for Ni based single crystal superalloys, Oral presentation, MSE 2018, Darmstadt, Germany
- **H. Yu** et al, Computational design of Ni superalloys focusing on the post-rafting stage; Poster presentation, Eurosuperalloy 2018, Oxford, UK
- **H. Yu** et al, On the compositional design of self-healing creep resistant steels based on Laves Phase filling of grain boundary cavities, ICSHM 2019, Oral presentation, Yokohama, Japan